Εθνικό Μετσόβιο Πολυτεχνείο
Σχολή Μηχανολόγων Μηχανικών
National Technical University Of Athens
School Of Mechanical Engineering
Fluids Department
Parallel CFD & Optimization Unit

Aerodynamic Design, Analysis & Adjoint Shape Optimization Of The DrivAer Motorsport Underfloor Using OpenFOAM

Diploma Thesis

Nikolakopoulos Anastasios

Supervisor: Professor Kyriakos C. Giannakoglou

Athens, 2019

Quality means doing it right when no one is looking.
Henry Ford

Acknowledgements

National Technical University Of Athens
School Of Mechanical Engineering
Fluids Department
Parallel CFD & Optimization Unit

Aerodynamic Design, Analysis & Adjoint Shape Optimization Of The DrivAer Motorsport Underfloor Using OpenFOAM

Diploma Thesis

Nikolakopoulos Anastasios
Supervisor: Professor Kyriakos C. Giannakoglou

The aim of this Diploma Thesis is the application of aerodynamic analysis and optimization tools to the design of a racing underfloor for the DrivAer car model. The underfloor modifications were made in accordance to the Le Mans Grand Touring Endurance regulations, that limit, among others, the underfloor geometry. The goal was to increase the downforce. Although the DrivAer model does not suit for direct use in motorsport, it was chosen for this analysis since it is a very refined, available car geometry and very few studies for the increase of downforce have been performed on this model. An additional objective is to investigate whether a simple passenger vehicle is able to satisfy motorsport requirements was desirable.

Initially, the new underfloor geometry was designed using in a CAD software. The underfloor was designed in concordance with the original geometry, following existing curves on the surface of the DrivAer model. A flat front splitter and a finless rear diffuser were added to the model, along with a flat underfloor.

Since the CAD software failed to recognise the merging points of the discrete parts that create the total vehicle geometry, the exported total model was not continuous, having non-manifold edges. A covering of the non manifold edges was attempted using in various ways, however the geometry was far too complex and non-manageable. The adopted solution was the import of the original geometry parts in the mesh generation software, along with a part containing solely the new underfloor, so that the recognition of the merging points was done by the more accurate mesh generator.

After the geometry had been inserted in the mesh generation software, the mesh was generated using primarily the snappyHexMesh tool in the OpenFOAM environment. Two refinement spaces were defined, one solely for the vehicle geometry and one for both the vehicle geometry and the vehicle wake. The space in close proximity to the road was also refined. The resulting unstructured mesh was comprised of approximately 5 million cells for the half of the vehicle, profiting from the symmetry of the case.

After the mesh generation, the air flow around the vehicle was simulated. The algorithm chosen for this simulation is the SIMPLE, in the OpenFOAM environment. The turbulence model selected was the Spalart—Allmaras. The wheels were non rotating, and the Reynolds number was 6.7 million. In order to compare the results with the performance of the original geometry, the original DrivAer model was also aerodynamically simulated for the same conditions. In this Diploma Thesis, the results of the modified DrivAer simulations are presented, along with comparisons with the original DrivAer.

In addition, the continuous adjoint problem was solved, in order to compute the sensitivity derivatives of the objective function, that is the downforce, again in the OpenFOAM environment. The sensitivity derivatives are presented the sensitivity map on the vehicle surface, which indicates possible modifications of the surface to improve the objective function. The adjoint optimization software incorporated in OpenFOAM was developed by the PCOpt Unit of the NTUA.

With the information of the sensitivity map, the geometry of the underfloor was parameterized using volumetric b-splines and was modified accordingly. It is noted that here, the sensitivity derivatives are computed with respect to the displacement of each control point of the volumetric b-splines. The software for the optimization was also developed by the PCOpt Unit of the NTUA.

Results the original and modified geometries are compared. The proposed modifications improved the aerodynamic performance of the vehicle, with a relatively slight further improvement coming from the adjoint-based optimization loop.

Εθνικό Μετσόβιο Πολυτεχνείο
Σχολή Μηχανολόγων Μηχανικών
Τομέας Ρευστών
Μονάδα Παράλληλης ΥΡΔ & Βελτιστοποίησης

Αεροδυναμικός Σχεδιασμός Ανάλυση & Βελτιστοποίηση Μορφής Με Τη Συζυγή Μέθοδο Αγωνιστικού Πατώματος Αυτοκινήτου Σε Περιβάλλον OpenFOAM

Διπλωματική Εργασία

Νικολακόπουλος Αναστάσιος

Επιβλέπων: Καθηγητής Κυριάκος Χ. Γιαννάκογλου

Στόχος της διπλωματικής εργασίας εργασίας είναι η εφαρμογή εργαλείων αεροδυναμικής ανάλυσης, σχεδιασμού και βελτιστοποίησης στον σχεδιασμό ενός αγωνιστικού πατώματος για το μοντέλο αυτοκινήτου DrivAer. Οι αλλαγές στο πάτωμα έγιναν σύμφωνα με τους κανονισμούς Le Mans Grand Touring Endurance, που οριοθετούν, μεταξύ άλλων, και τη γεωμετρία του πατώματος. Στόχος είναι η αύξηση της κάθετης αεροδυναμικής δύναμης που δημιουργείται από το σώμα του οχήματος. Παρά το γεγονός πως το μοντέλο DrivAer δεν ενδείκνυται για απ' ευθείας χρήση στον μηχανοκίνητο αθλητισμό, επιλέχθηκε για την εν λόγω ανάλυση καθώς πρόκειται για μία εξαιρετικά λεπτομερή διαθέσιμη γεωμετρία αυτοκινήτου στην οποία έχουν γίνει ελάχιστες μελέτες για την αύξηση της κάθετης δύναμης. Επίσης, ήταν επιθυμητή η εξέταση του κατά πόσο ένα απλό επιβατηγό όχημα δύναται να πληροί αγωνιστικές προδιαγραφές.

Αρχικά, δημιουργήθηκε η νέα γεωμετρία του πατώματος σε λογισμικό CAD. Το πάτωμα δημιουργήθηκε σε συμφωνία με την αρχική γεωμετρία ακολουθώντας υπάρχουσες καμπύλες στο μοντέλο DrivAer, το οποίο αποτελείται από αρχεία επιφανειακής γεωμετρίας. Στο μοντέλο προστέθηκαν ένας εμπρός επίπεδος splitter, ένας διάχυτης στο πίσω μέρος και ένα τελείως επίπεδο (πλην της περιοχής του διαχύτη) πάτωμα.

Καθώς το λογισμικό CAD δεν αναγνώριζε τα σημεία επαφής μεταξύ των διαφόρων τμημάτων που απαρτίζουν τη συνολική γεωμετρία του αυτοκινήτου, το εξαγόμενο από το λογισμικό CAD συνολικό μοντέλο δεν ήταν συνεχές, αλλά είχε οπές. Έγινε απόπειρα κάλυψης των οπών με τη βοήθεια των λογισμικών MeshLab και Blender, αλλά η γεωμετρία ήταν υπερβολικά περίπλοκη και μη-διαχειρίσιμη. Η λύση που υιοθετήθηκε ήταν να εισαχθούν στον πλεγματοποιητή τα πρωτότυπα τμήματα του μοντέλου, μαζί με ένα νέο αρχείο που περιείχε μόνο τις νέες διαμορφώσεις, έτσι ώστε να αναγνωρίσει ο πλεγματοποιητής τα σημεία επαφής μεταξύ των διαφόρων τμημάτων.

Στη συνέχεια, δημιουργήθηκε το πλέγμα, κυρίως με το εργαλείο snappyHexMesh στο OpenFOAM. Δημιουργήθηκαν επίσης δύο περιοχές αυξημένης ανάλυσης πλέγματος, μία μόνο για τη γεωμετρία του οχήματος και μία για τη γεωμετρία του οχήματος μαζί με τον ομόρρου. Επίσης, δημιουργήθηκε περιοχή αυξημένης ανάλυσης πλησίον του δρόμου. Το τελικό μη-δομημένο πλέγμα αποτελείται από περίπου 5 εκατομμύρια κελιά για το ήμισυ όχημα μιας και, λόγω συμμετρίας, το πλέγμα δημιουργήθηκε γύρω από το δεξί ήμισυ του οχήματος.

Μετά τη δημιουργία του πλέγματος, προσομοιώθηκε η αεροδυναμική ροή γύρω από το όχημα. Ο αλγόριθμος που επιλέχθηκε για την επίλυση είναι ο SIMPLE στο περιβάλλον OpenFOAM. Ως μοντέλο τύρβης επιλέχθηκε το Spalart-Allmaras. Επιλέχθηκε οι τροχοί και ο δρόμος να είναι ακίνητοι, και ο αριθμός Reynolds της ροής είναι 6.7 εκατομμύρια. Για λόγους σύγκρισης, προσομοιώθηκε και η αρχική γεωμετρία του DrivAer. Στην εργασία παρουσιάζονται τα αποτελέσματα της προσομοίωσης αυτής καθώς και η σύγκρισή τους με την προσομοίωση του αρχικού DrivAer.

Επιπρόσθετα, επιλύθηκαν οι συζυγείς εξισώσεις ροής προς υπολογισμό των παραγώγων ευαισθησίας της αντικειμενικής συνάρτησης, δηλαδή της κάθετης δύναμης, ξανά σε περιβάλλον OpenFOAM. Οι παράγωγοι ευαισθησίας δημιουργούν τον χάρτη ευαισθησίας στην επιφάνεια του αυτοκινήτου, ο οποίος υποδεικνύει τις πρέπουσες μετακινήσεις της επιφάνειας για βελτίωση της τιμής της αντικειμενικής συνάρτησης. Το λογισμικό της βελτιστοποίησης με τη συνεχή συζυγή μέθοδο στο περιβάλλον του OpenFOAM αναπτύχθηκε στη ΜΠΥΡ&Β του ΕΜΠ.

Με την πληροφορία του χάρτη ευαισθησίας, τροποποιήθηκε η γεωμετρία του πατώματος, αφού πρώτα περιγράφηκε παραμετρικά με χρήση ογκομετρικών καμπύλων b-splines. Σημειώνεται πως εδώ, ο χάρτης ευαισθησίας υπολογίσθηκε συναρτήσει της μετατόπισης των σημείων ελέγχου των b-splines που την παραμετροποιούν. Το λογισμικό που τροποποιεί την γεωμετρία αναπτύχθηκε και αυτό στη ΜΠΥΡ&Β του ΕΜΠ.

Τα αποτελέσματα συγκρίθηκαν με την αρχική και τροποποιημένη γεωμετρία. Οι μετατροπές στο πάτωμα βελτίωσαν την αεροδυναμική απόδοση του οχήματος, με επιπλέον μικρότερες βελτιώσεις να απορρέουν από τη βελτιστοποίησή τους μέσω της συνεχούς συζυγούς μεθόδου.

Index

References 89

Acronyms

2D	Two Dimensional
3D	Three Dimensional
CAD	Computer Aided Design
CFD	Computational Fluid Dynamics
CPU	Central Processing Unit
FFD	Free Form Deformation
FOAM	Field Operation And Manipulation
NTUA	National Technical University Of Athens
PCOpt	Parallel CFD & Optimization
RANS	Reynolds-Averaged Navier—Stokes
TUM	Technische Universität München
ΕΜΠ	Εθνικό Μετσόβιο Πολυτεχνίο
ΥΡΔ	Υπολογιστική Ρευστοδυναμική
ΜΠΥΡ&Β	Μονάδα Υπολογιστικής Ρευστοδυναμικής & Βελτιστοποίησης

1.   Introduction

1.1. The Front Splitter And The Rear Diffuser In Motorsport

1.1.1. A General Brief Introduction

In motorsports, the winner is in general determined on the shorter race time in the race classification. In order to achieve higher speeds, racing car engineers design the vehicles with maximum grip in mind. Apart from increasing the so-called mechanical grip, which is primarily resultant from the suspension and chassis characteristics, the grip is also increased by increasing the aerodynamic grip. Engineers design the vehicle bodywork aerodynamically, with the main aims of minimising the drag and maximising the downforce. The downforce pushes the vehicle towards the road, improving tyre grip. This lessens the risk of wheel spin at high speeds and raises cornering speeds, resulting in overall shorter lap times. Two aerodynamic components that are often used are the splitter at the front and the diffuser at the rear.

These two components will be incorporated to the original car geometry and will be optimized. In figure 1.1, the original geometry with the aerodynamic additions is depicted.
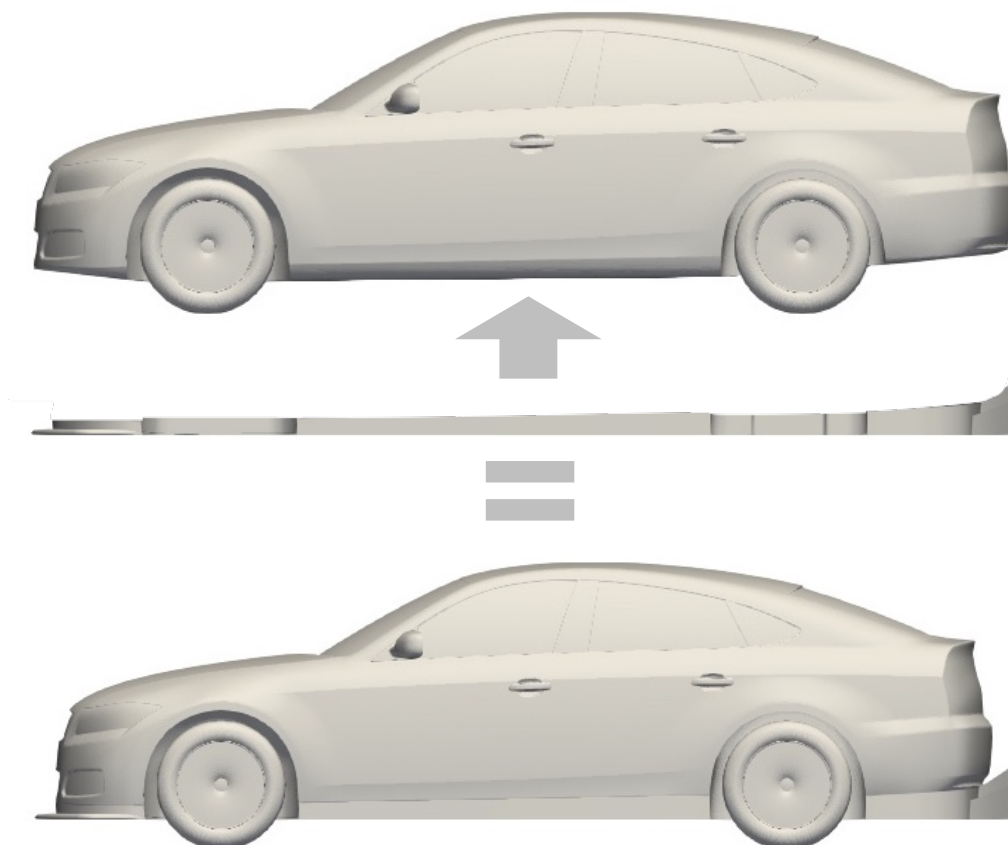
Figure 1.1: The assembly of original geometry and the aerodynamic additions modifications, resulting to the modified geometry.

1.1.2. Front Splitter

Front splitters are aerodynamic components that primarily create front-end downforce and balance the front-to-rear distribution of downforce. The splitter is typically found at the front of a race car, appearing as a flat extension to the very bottom of the front bumper. This splitter extends out, mostly parallel to the ground. While it is attached to the bottom of the front bumper it may also be supported by two or more support rods at some distance forward of the bumper mounting points. These support rods ensure minimal or regulated deformation to the splitter under high aerodynamic loads.[1]

In figure 1.2 an explanation of the splitter function is given.
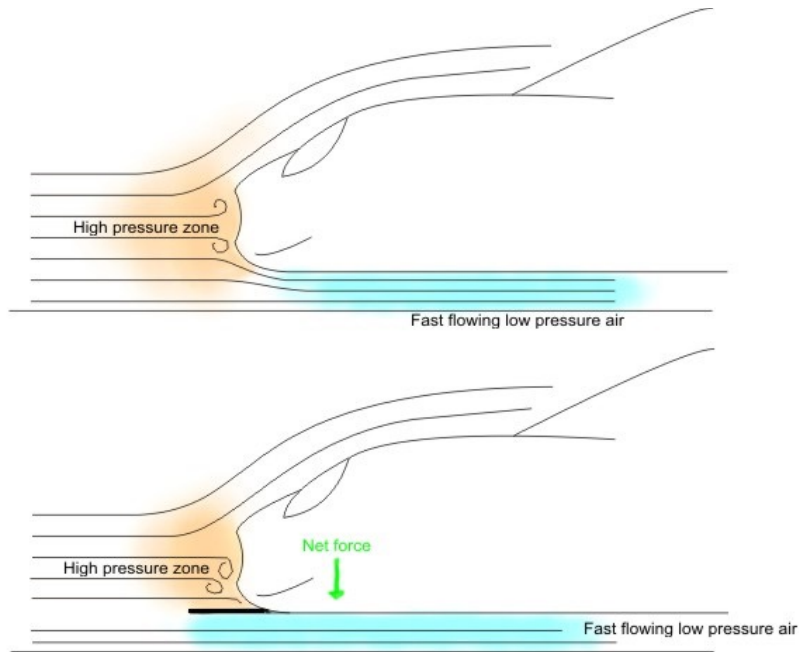
Figure 1.2: Airflow in the front of a car without a splitter (top) and with a splitter (bottom).[2]

The splitter serves the following main purposes:

- Increases downforce, by stagnating airflow on the top and accelerating air flow from below, increasing the difference in static pressure between its top and bottom surfaces, yielding an overall pressure effect of downforce,

- Balances the front-to-rear downforce distribution, since the downforce effect of the splitter is significant compared to the rear wing,[3]

- Regulates the amount of underfloor airflow, according to underfloor brake cooling ducts, power unit cooling ducts and rear diffuser specifications.

1.1.3. Rear Diffuser

The rear diffuser is also used to increase underfloor downforce. The main aim of the diffuser is to allow more air to flow at a greater velocity under the vehicle. The diffuser itself does not function in the same way a racing car wing does, nor in the way a diffuser does in a closed duct.[4]

The diffuser itself decelerates the airflow inside itself. However, if it is designed appropriately, it ensures a smooth mixing with the airflow around the rest of the vehicle. This results in reduced flow losses, allowing a greater overall airflow rate through the underbody. By increasing the underbody flow velocity, the static pressure decreases, increasing overall downforce created by the vehicle. This is the basic function of a diffuser as explained schematically in figure 1.3.

Rapid flow in the throat of the diffuser produces low pressure

Flow returned smoothly to ambient velocity
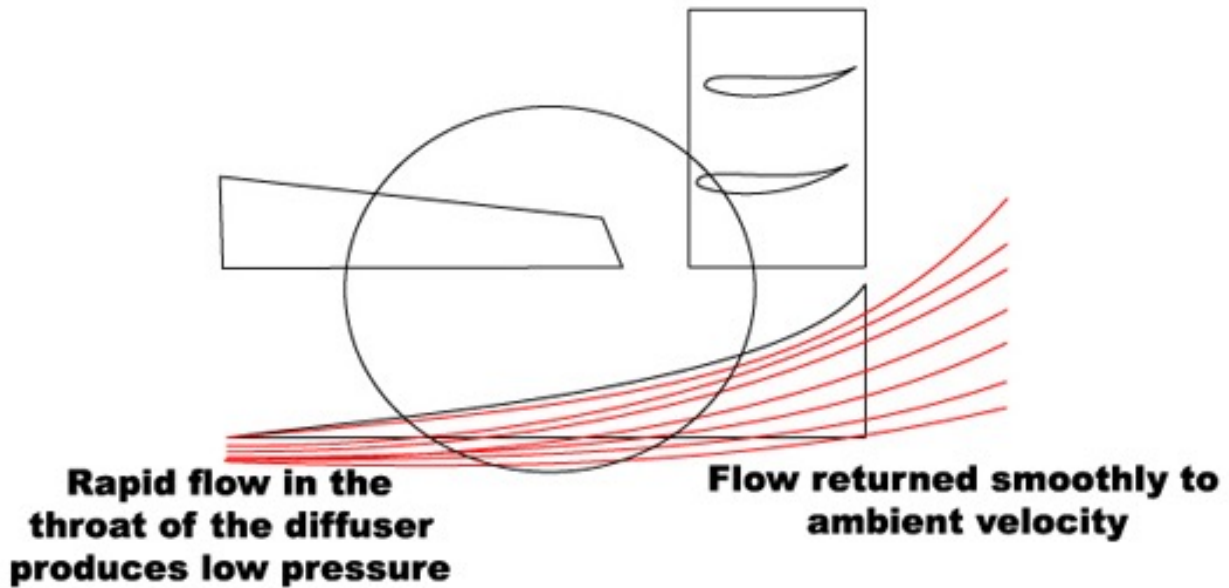
Figure 1.3: Airflow at the rear of a car with a diffuser.[5]

The rear diffuser may also direct airflow upwards at its tip. This means that the equal and opposite force effect of the airflow to the diffuser results in additional downward force. This is often described with the term "underbody upsweep".[6]

In addition, the rear diffuser creates longitudinal vortices in the airflow. These vortices assist in channelling high energy airflow from around the side of the vehicle to the diffuser, allowing for more airflow rate and, thus, greater downforce.

1.2. The Adjoint Method In Optimization

The adjoint method was firstly used in control theory and it is used in optimization in a plethora of phenomena that are governed by partial differential equations.[7] In this case, the air flow, which is governed by the Navier—Stokes equations and a turbulence model. The adjoint method is a mathematical computational tool for computing the sensitivity derivatives of an objective function with respect to the design variables of a model. These derivatives can be utilized in a gradient based optimization method.

The adjoint method is divided into two major subcategories, the discrete and the continuous. In the discrete adjoint method, the objective function and the state equations are firstly linearized and discretized and then, from the discretized equations, the adjoint equations emerge. In the discrete adjoint method the resulting adjoint equations are directly in matrix form and are able to be solved numerically. In the continuous adjoint method, the adjoint equations are firstly expressed mathematically using the continuous state equations. The adjoint equations are in the partial differential equations form. They are then discretized and solved numerically.

The adjoint equations are derived by adding the volume integral of the product of the adjoint variables with the state equations to the objective function. By formulating and using the Green—Gauss theorem, the final expression of the adjoint flow equations and the boundary conditions are determined.

The state equations are often called primal equations. Their solution is often expressed as the "primal problem", while the solution of the adjoint equation is often called the "adjoint problem".

The main advantage of the adjoint method is its low computational cost. Due to the nature of its equations and the procedure of their formulation, the computational cost of the adjoint method is independent to the number of design variables. This enables the optimization of complex geometries described parametrically using parametric analytic geometries such as volumetric b-splines and Bézier surfaces. The time required for the solution of the adjoint equations is about the same to the time required for the solution of the primal equations. The total time required for the computation of the sensitivity derivatives is primarily the time needed to solve the primal and the adjoint problems.

On the other hand, the main disadvantage of the continuous adjoint method is the extra time and effort required to reform the adjoint problem for new objective functions. The new resulting equations have to be discretized and programmed for numerical solution. In a multi-objective optimization case, the total time required for the computation of the sensitivity derivatives is primarily the time needed to solve the primal and, in most cases, each of the adjoint problems.

In comparison with the direct differentiation method, the adjoint method is superior in cases with more design variables than objectives but inferior in cares with more objectives that design variables. The engineer is called to evaluate and decide on the optimization tools according to each case characteristics.

1.3. The OpenFOAM Software

OpenFOAM is an open source CFD software. OpenFOAM was created by Henry Weller in 1989 under the name "FOAM" and was released open source as "OpenFOAM" by Henry Weller, Chris Greenshields and Mattijs Janssens in December 2004.[8] It has a large user base across most areas of engineering and science, from both commercial and academic organizations. It has numerous tools and features for simulating cases in many scientific fields.[9] In this Thesis, the tools used for mesh generation and for simulation of steady incompressible turbulent air flows are used, along with the tools for the continuous adjoint simulation and free form deformation using volumetric b-splines, both developed by the PCOpt Unit of the NTUA.

OpenFOAM is wholly programmed in C++. In combination with the fact that it is an open source software, users are potentially able to develop additional tools for their respective needs and their demands, in order to satisfy certain specifications. Additionally, it is also relatively easy for the independently developed tools to be distributed and utilized by others with similar demands or to be developed further by other researchers.

Such an example of third party developed tools are the continuous adjoint tools and free form deformation tools used in this thesis, both developed by the PCOpt Unit of the NTUA.

The aid in development by independent users has accelerated the overall development of the software and its is generally technologically equivalent to commercial alternatives, while at the same time it is free to use.[10] Another consequence of the open source attribute is the large OpenFOAM user community, which has created many useful threads in forums, enabling quick solution findings to most common problems.

1.4. Aim & Structure Of This Diploma Thesis

The main aim of this Diploma Thesis is the shape optimization of racing underfloor modifications on the DrivAer passenger car model. This is achieved via the solution of the primal problem, the continuous adjoint problem and by implementing a free form deformation method on the vehicle geometry. The optimization aim is downforce maximization. The continuous adjoint method is utilized to compute the sensitivity derivatives, through which a next solution closer to the optimal is indicated. This repeats on each cycle, allowing to eventually reach or approximate the optimum.

The structure of the Diploma Thesis is as follows:

- In chapter 2, the original DrivAer model and the relative parts of the LMGTE regulations and the modified DrivAer vehicle geometry are presented.

- In chapter 3, the mesh generation procedure is explained and presented.

- In chapter 4, the primal problem is described: its flow equations, the turbulence model equations and the boundary conditions. The results from the simulation of the modified vehicle as well as the original DrivAer is presented.

- In chapter 5, the adjoint problem is described: its partial differential equations and the boundary conditions. The results from the simulation of the modified vehicle are presented, along with the sensitivity map on the surface of the vehicle. This is a single step in the whole optimization process.

- In chapter 6, a free form deformation method is presented, using volumetric b-splines in order to parameterize and modify parts of the vehicle geometry. The results of the full optimization procedure are presented.

- In chapter 7, a summation is done, the conclusions of this Diploma Thesis are expressed and suggestions for future work are made.

2. Vehicle Model

2.1. DrivAer Model

The DrivAer vehicle model is a realistic generic car geometry proposed by the TUM, Audi AG and BMW Group. The geometry is based upon two medium-sized passenger cars, the third generation Audi A4 (B7) and the fifth generation BMW 3 Series (E90). The purpose of this model is to popularize a realistic passenger car geometry for computer simulations.[11] In figure 2.1, the side view of the geometry of a BMW E90 3 Series coupé and an Audi B7 A4 saloon is shown individually and combined.
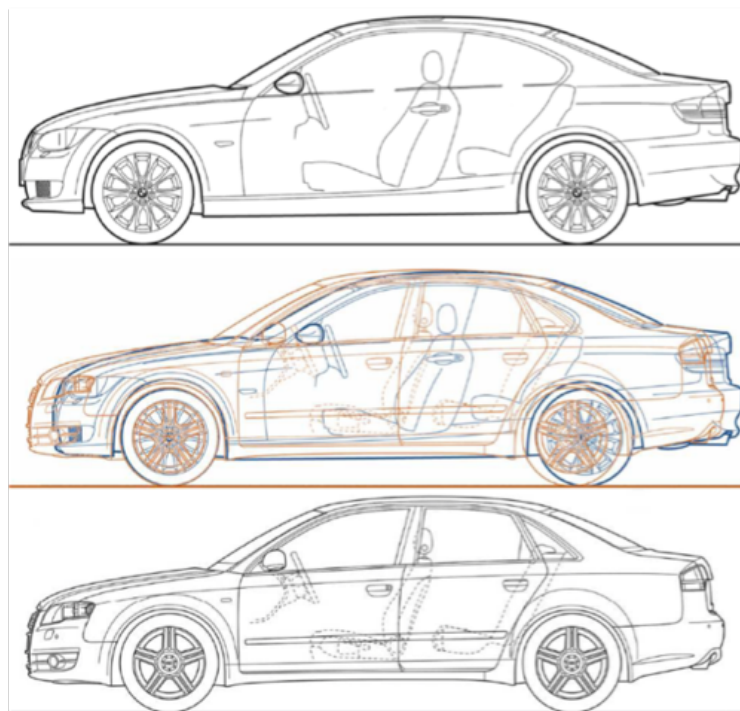
Figure 2.1: Side view of the geometries of the individual vehicles and a combined view, which is the base for the DrivAer geometry. On top is the coupé version of the E90 BMW 3 Series, on the bottom is the saloon version of the B7 Audi A4 and in the middle is a combined view.[12]

The DrivAer geometry is modular. The main body is common for all configurations. There are multiple choices for the body type, regarding the roof line, where saloon, estate and fastback configurations are available. There are also two versions of the underfloor, a smooth and a detailed one. Additionally, here is the option to include wheels and wing mirrors. In figures 2.2 to 2.5, different alternatives for the configurations are shown.
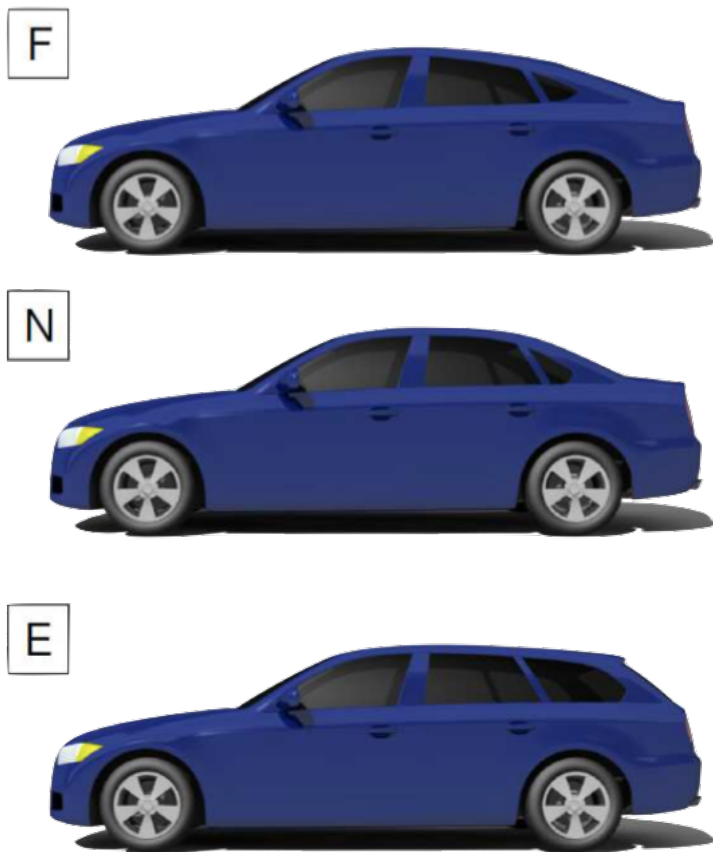
Figure 2.2: The alternatives for the roof line. Top to bottom: Fastback [F], Saloon (Notchback) [N] and Estate Back [E].
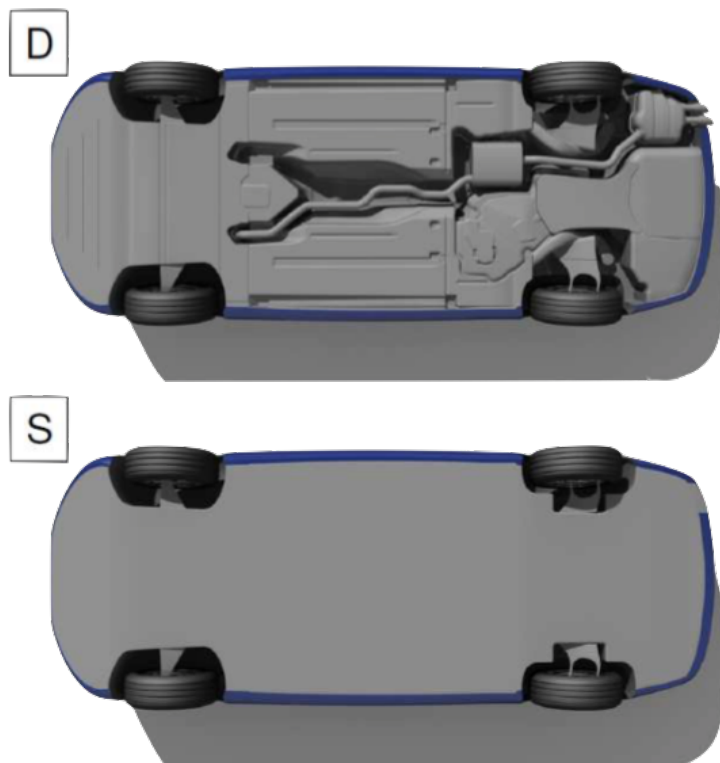
Figure 2.3: The alternatives for the underfloor: Top to bottom: Detailed [D] and Smooth [S].
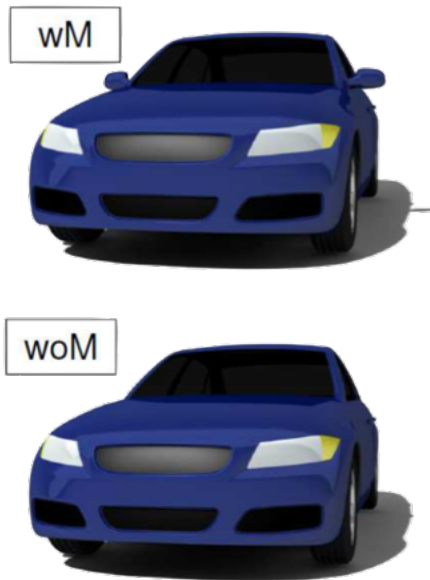
Figure 2.4: The alternatives for the wing mirrors. Top to bottom: With mirrors [wM] and Without mirrors [woM].

Figure 2.5: The alternatives for the wheels. Top to bottom: With wheels [wW] and Without wheels [woW].

The configuration used in this Diploma Thesis is a fastback with smooth underfloor, with closed wheels and mirrors.

2.2. Le Mans Grand Touring Endurance Cars

2.2.1. In General

The Le Mans Grand Touring Endurance (LMGTE) is a category of race cars in the FIA World Endurance Championship (WEC), racing alongside LMP1 and LMP2 (Le Mans Prototype 1 and 2, respectively). The cars are racing versions of road legal production models, available for public purchase by an Endurance Committee recognized dealer network. The category is split into two distinct sub-categories, the LMGTE Pro and the LMGTE Am, designed for professional and amateur racing drivers, respectively.

The vehicles are two door, 2 or 2+2 seats, open or closed cars. The engine capacity is limited to 5.5 litres and 4.0 litres for naturally aspirated and forced induction power units, respectively. The minimum dry weight of the cars is 1245 kg, subject to Balance of Performance alterations.[13] Further technical regulations are described in the official technical regulations document.

The cars are heavily modified from their road legal versions, sharing few to no parts. However, the design of the original vehicle is dominant and the respective road legal model is easily recognizable.

The models that are competed in 2019 24 hours of Le Mans, the second round of the 2019 championship, in the LMGTE categories are:

- Aston Martin Vantage,
- Aston Martin Vantage AMR,
- BMW M8 GTE,
- Chevrolet Corvette C7.R,
- Ferrari 488 GTE,
- Ferrari 488 GTE EVO,
- Ford GT,
- Porsche 911 RSR.[14] [15]

The winners of the 2019 Le Mans was the Ferrari 488 GTE EVO in the LMGTE Pro class and the Porsche 911 RSR in the LMGTE Am class.[16] [17]

Among these vehicles, different design solutions have been implemented regarding the front splitter and the rear diffuser. These solutions are presented in the next sections.

In figure 2.6 an LMP1, an LMP2, an LMGTE Pro and an LMGTE Am car renders are shown.
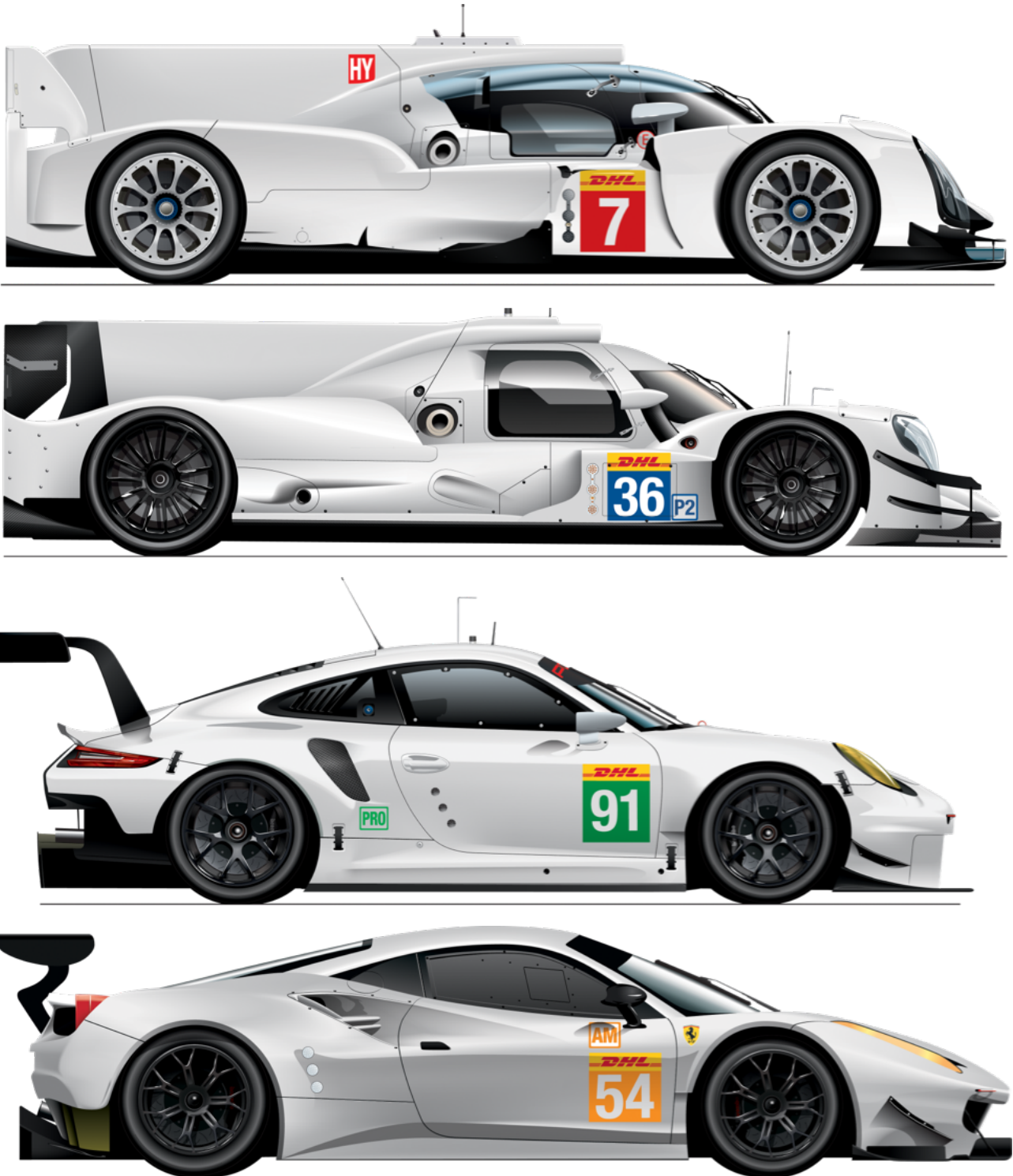
Figure 2.6: Top to bottom: An LMP1 car (Toyota TS050), an LMP2 car (Oreca 07), an LMGTE Pro car (Porsche 911 RSR) and an LMGTE Am car (Ferrari 488), all subjected to the 2017 technical regulations. Images not to scale.

2.2.2. Front Splitter

According to the 2019 technical regulations, the front splitter must be included in a free volume named V4. This free volume allows for a maximum front overhang of 1150 mm and a maximum protrusion from the vehicle front bumper of 100 mm. The volume is also bounded at the bottom by a horizontal plane at the lowest height of the bodywork (also named as reference surface) and by a horizontal plane 150 mm above it.

The original description by the regulations is as follows:

Main front aerodynamic device (Splitter)

One lower aerodynamic device may be added within Volume V4.

Material: Composite permitted.

Dimensions: Its overall length must not exceed 1150 mm, measured from the front axle centreline. Its overall width must not be greater than that of the front fenders.
*Maximum protrusion from the **perimeter of the original bodywork** (def7): 100 mm.*

Shape: Wing profile forbidden.

Continuous lower and upper surfaces. (through-flow air openings not permitted)
Leading and side edges radius = 5 mm minimum.

Le Mans aerodynamic Kit:

The shape of the lower surface of the homologated device may be modified by the addition of in-fill parts.

In figure 2.7 the schematic from the regulations explaining the volume V4 is shown.

1. Splitter Free Volume
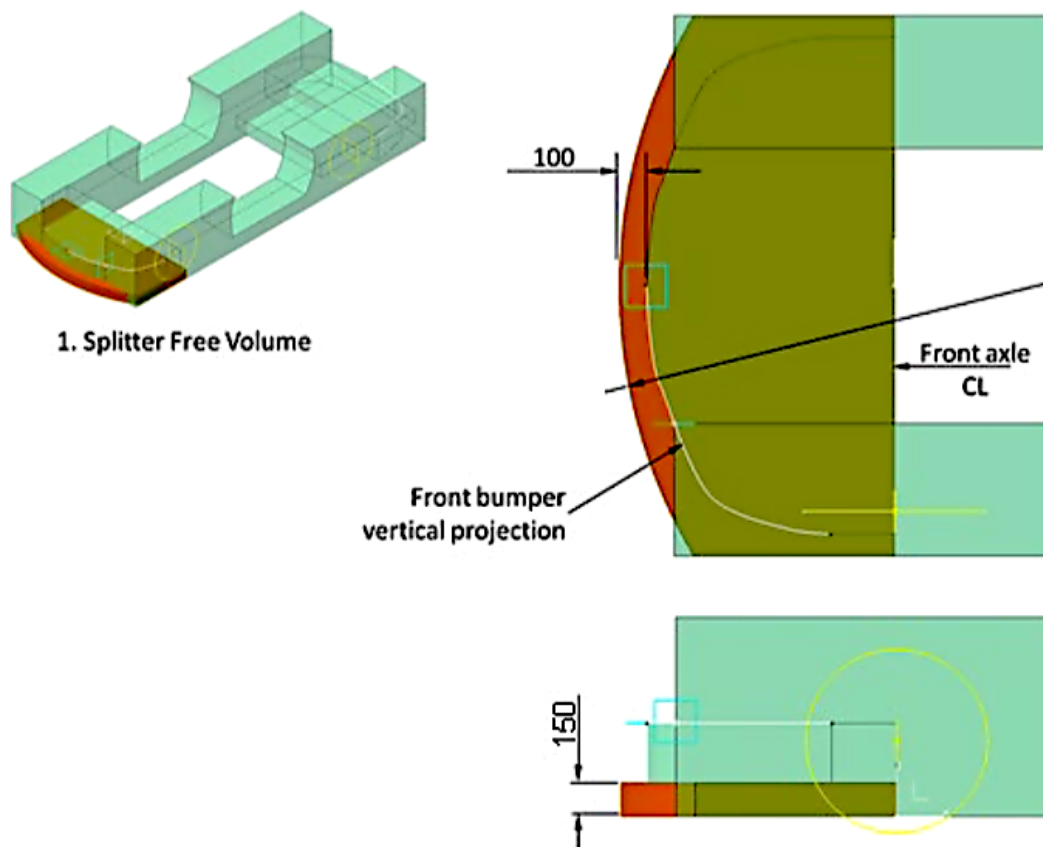
Figure 2.7: The free volume V4 concerning the front splitter, as in the 2019 Technical Regulations For Grand Touring Cars. The volume position is explained in the left picture, with the front of the car facing to the left and with yellow lines representing the outlines of the wheels. The maximum protrusion is explained in the top right corner and the maximum height in the bottom right corner.

The solutions implemented on current race cars is either a flat or a curved splitter. The curved splitter is raised towards the centreline of the car. In figure 2.8 different front splitter solutions are shown.

Figure 2.8: Different solutions for the front splitter. A flat splinter on the Chevrolet Corvette C7.R[18] (top) and a curved splitter on the Ferrari 488 GTE EVO[19] (bottom).

It is expected that the optimization results will modify the splitter into a solution resembling one of the above.

2.2.3. Rear Diffuser

According to the 2019 technical regulations, the rear must be included in a free volume named V7. This free volume allows for a maximum rear overhang of 1050 mm and a maximum protrusion from the vehicle rear bumper (dictated by a reference free volume named V5) of 100 mm. The volume is also bounded at the bottom by the reference surface and by a horizontal plane at 260 mm above it.

The original description by the regulations is as follows:

Rear diffuser

One lower aerodynamic device may be added within Volume V7.

Material: Composite permitted.

Dimensions: The overall length must not exceed 1050 mm, measured from the rear axle centreline.
At the car longitudinal centreline, the protrusion from the perimeter of the bodywork situated above Volume V5 must not be greater than 100 mm.

Shape: Wing profile forbidden.
The leading edge must be on the Reference Surface.

Fins: Permitted.

In figure 2.9 the schematic from the regulations explaining the volume V7 is shown.
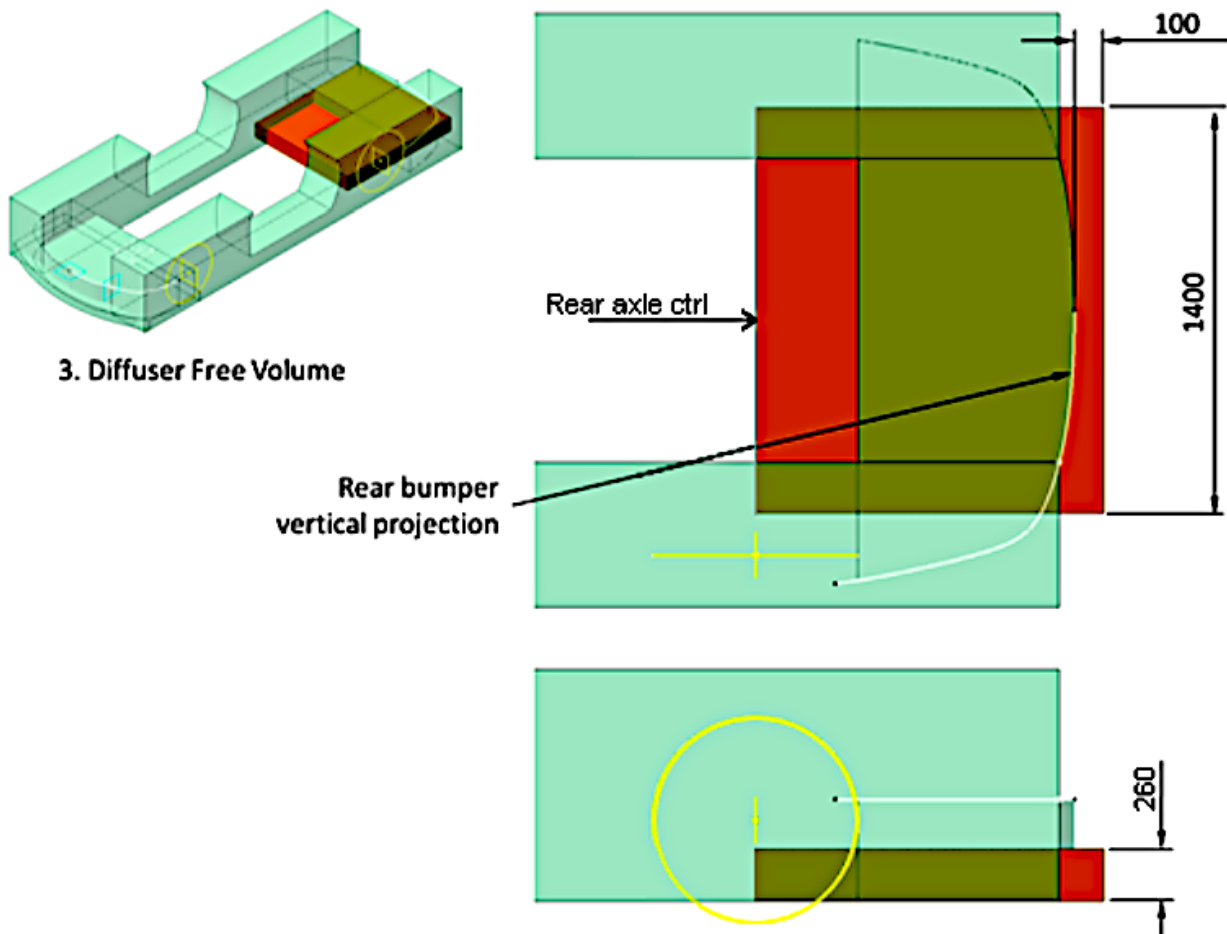
Figure 2.9: The free volume V7 concerning the rear diffuser, as in the 2019 Technical Regulations For Grand Touring Cars. The volume position is explained in the left picture, with the front of the car facing to the left and with yellow lines representing the outlines of the wheels. The maximum protrusion and maximum width are explained in the top right corner and the maximum height in the bottom right corner.[20]

There are also multiple solutions implemented for the rear diffuser. The rear diffuser perimeter, in a vertical transverse section may have rectangular shape, stepped rectangular shape or a free symmetrical curve. The rear diffuser may also have vertical longitudinal fins. The design of the BMW M8 GTE's diffuser is particularly interesting, since it is the only solution with open sidewalls. In figure 2.10, different solutions for the rear diffuser are shown.

Figure 2.10: Top to bottom: Different solutions for the rear diffuser. A rectangular diffuser on the Aston Martin Vantage[21], a stepped rectangular diffuser on the Porsche 911 RSR[22] and a curved diffuser on the Ford GT[23]. The diffuser of the BMW M8 GTE[24], which has open sidewalls is also shown at the very bottom.

Again, it is expected that the optimization results will modify the rear diffuser into a solution resembling one of the above.

2.3. Modified DrivAer Model

The modified DrivAer model was created by adding and modifying the original DrivAer geometry as distributed by the Technical University of Munich into a Computer Aided Design (CAD) software. The CAD software used was SolidWorks by Dassault Systèmes (using the license of the School of Mechanical Engineering of the NTUA). All added geometry was created in full accordance to the technical regulations. However, it must be stated that the original DrivAer model does not comply with all technical regulations, since it was not designed for the FIA World Endurance Championship. It is also noted that the aerodynamic additions were created solely by the writer of this Thesis.

A simple, flat splitter was chosen and a stepped rectangular design without fins for the diffuser was implemented. Furthermore, a flat underfloor was created under most of the body and around the diffuser. This geometry will be inserted in the optimization software and it will be compared with the results.

The exported model format was stl (stereolithography).

In figures 2.11 to 2.15, renders of the modified DrivAer geometry are shown.
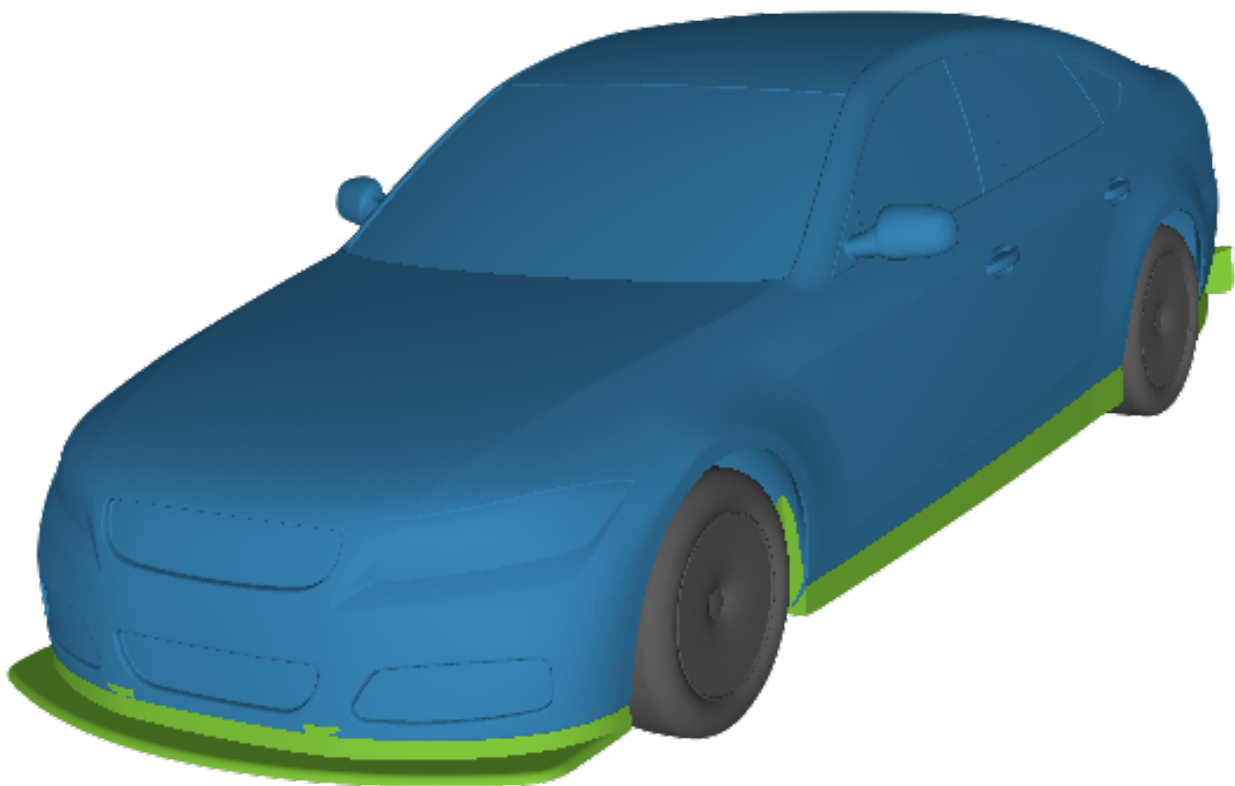
Figure 2.11: Front 3/4 view of the modified DrivAer model. With blue colour is depicted the original body geometry, with green is the floor additions and with grey are the wheels.

Figure 2.12: Rear 3/4 high elevation view of the modified DrivAer model. With blue colour is depicted the original body geometry, with green is the floor additions and with grey are the wheels.

Figure 2.13: Rear 3/4 low elevation view of the modified DrivAer model. With blue colour is depicted the original body geometry, with green is the floor additions and with grey are the wheels.

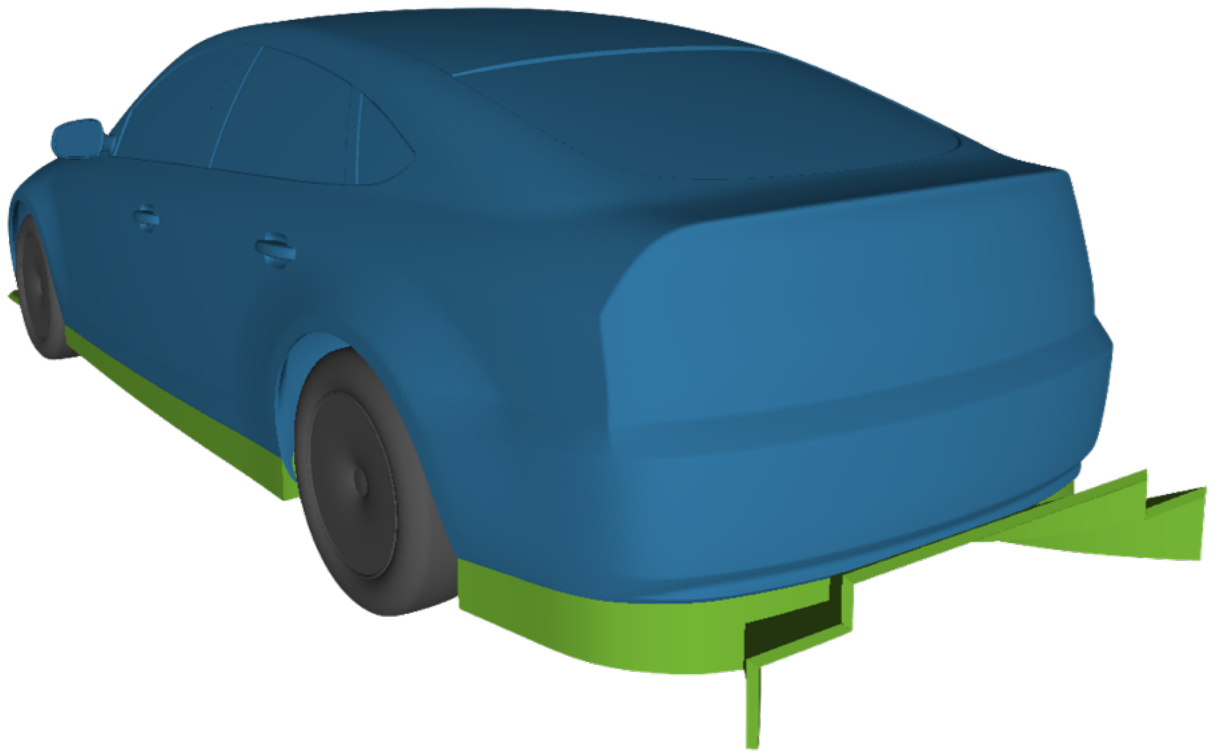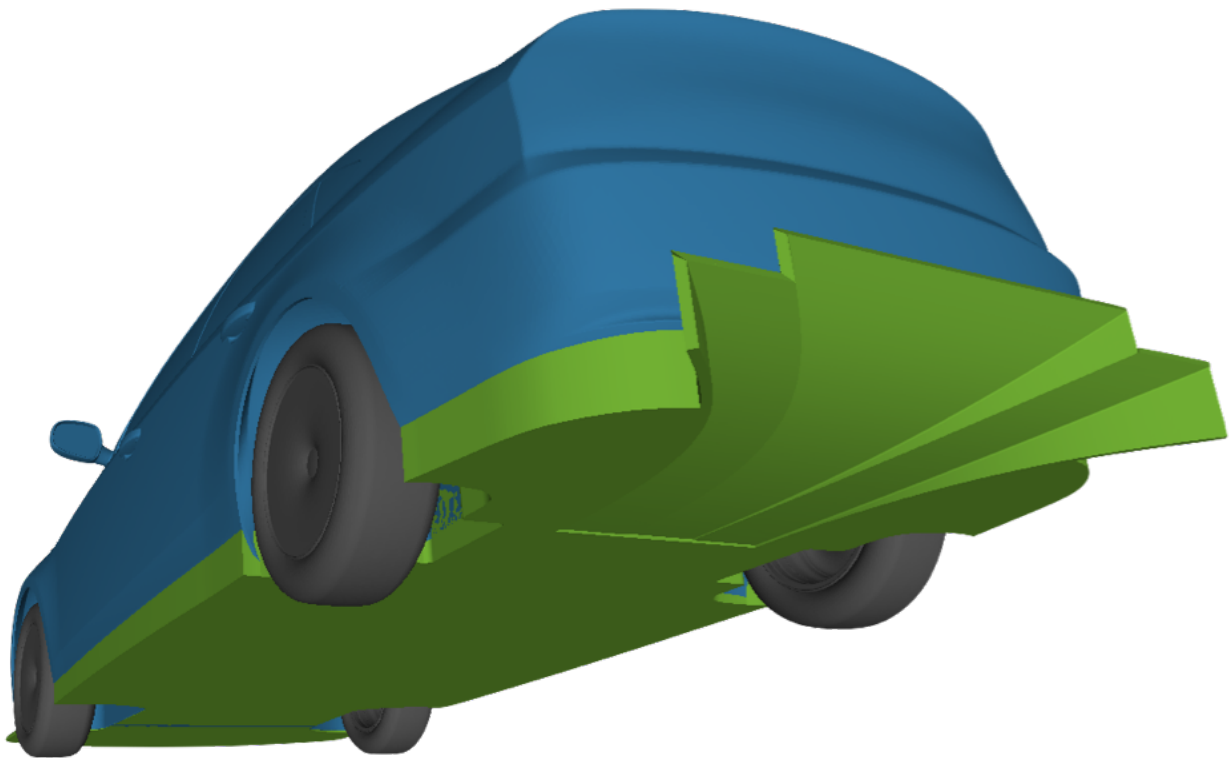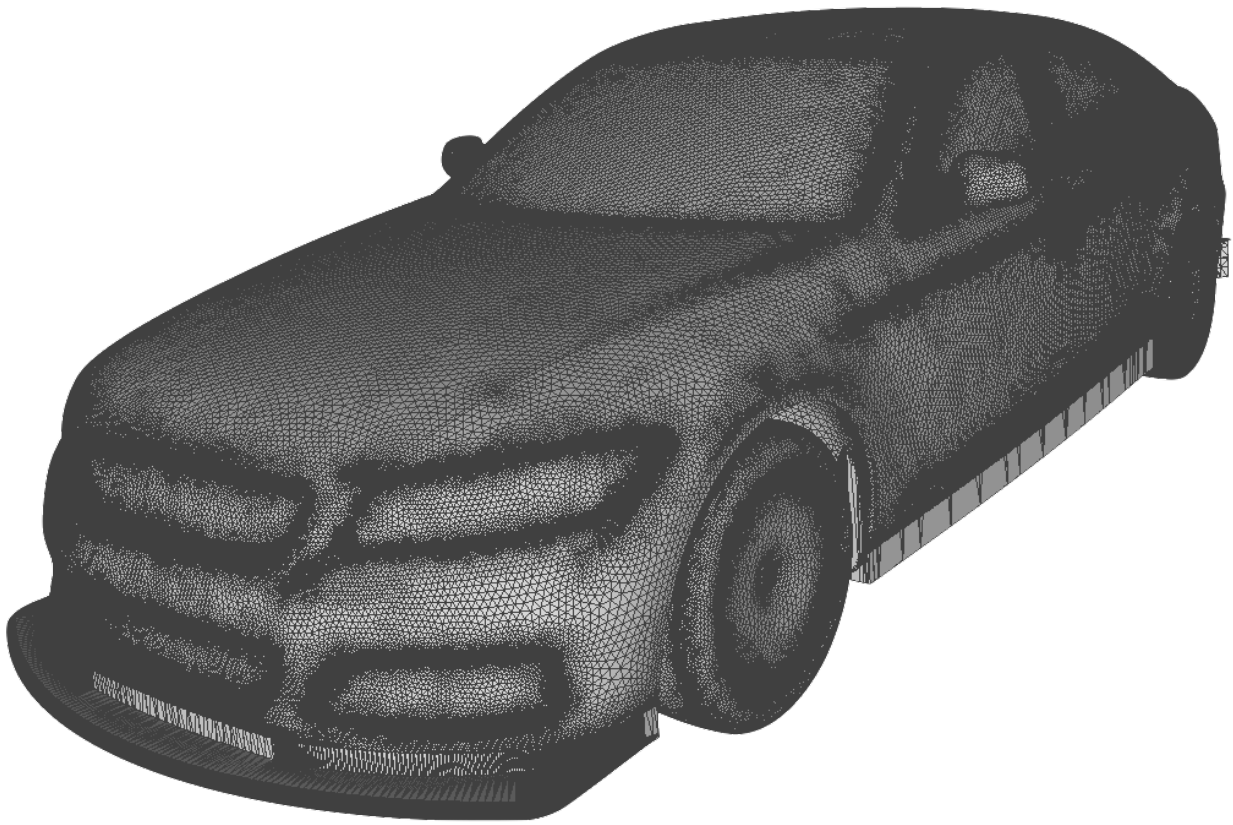*Figure 2.14: Front 3/4 view of the modified DrivAer model. With grey lines the stl geometry triangle edges are depicted.*
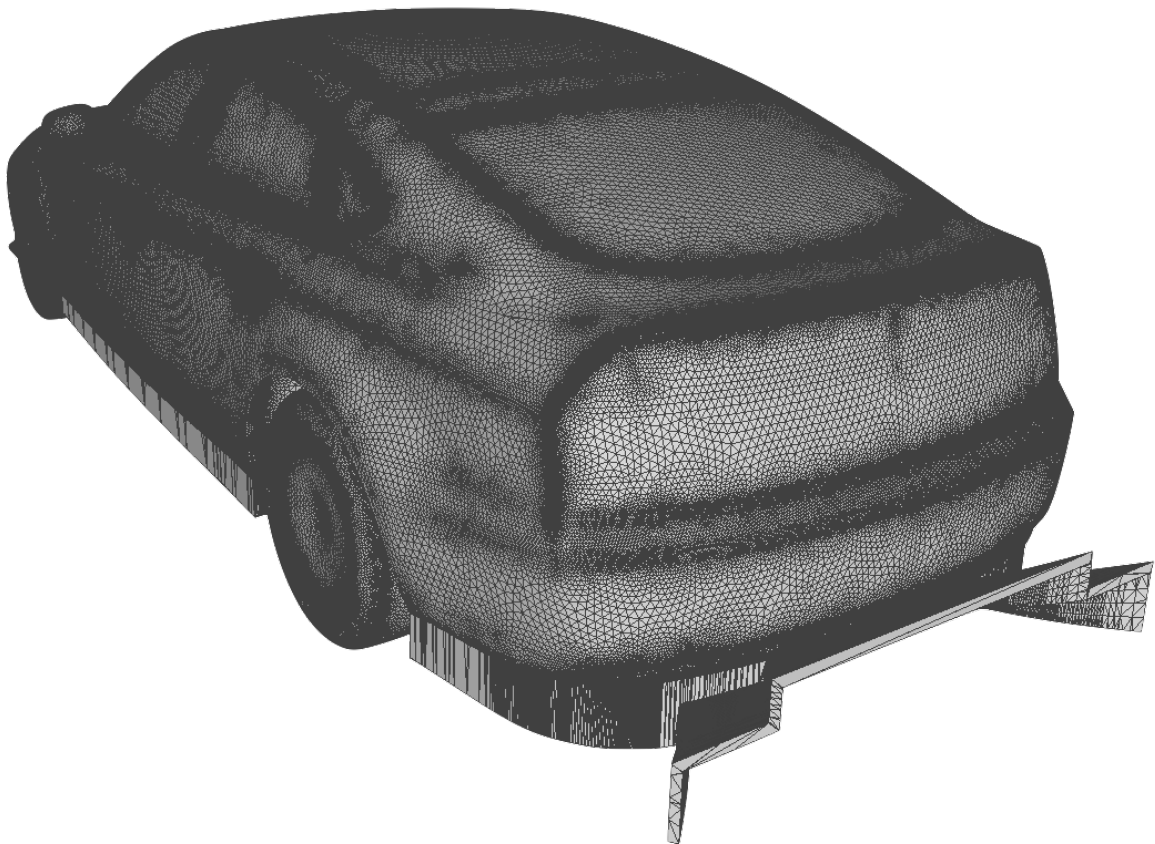
Figure 2.15: Rear 3/4 high elevation view of the modified DrivAer model. With grey lines the stl geometry triangle edges are depicted.

3. Mesh Generation

3.1. In General

3.1.1. General Procedure

The differential equations that describe the airflow around or inside an object, in most complex cases, do not have an analytical solution. A solution is reached via numerical methods solving the equations of the fluid flow. This computational domain is composed of many small simple quanta where the discretized equations are solved. These quanta are called cells and usually have a simple shape, namely tetrahedra, hexahedra, prisms, e.t.c. The total of the cells is the computational mesh. In this simulation, the mesh is hybrid, with the layers added on the vehicle and road surfaces being structured and the rest of the mesh being unstructured.

Since, in our case, the geometry is symmetrical, the computational mesh encloses half of the vehicle. The symmetry plane of the mesh is the longitudinal symmetry plane of the vehicle.

The mesh is generated by tools provided by the OpenFOAM software. The mesh generation was initialized by a structured mesh using cells with an aspect ratio close to unity created by the *blockMesh* tool. The vehicle geometry was then inserted in stl format and the mesh generation is executed using the following tools:

- The tool *surfaceFeatureExctract* helps in recognising particular geometry characteristics and improves their interpretation by the meshing software.

- The tool *snappyHexMesh* did the final detailing, which creates the cells in close proximity to the model geometry in an appropriate manner, so as to approximate the model geometry and to result in adequate thin layering for satisfactorily boundary layer computations.

Close to the far field a less fine mesh was generated, in order to save on computational costs. The flow in these points can be adequately approximated by such a sparser mesh, while the flow close to the model needs to be computed with greater precision, in order to obtain realistic values on the aerodynamic forces acting upon the vehicle.

3.1.2. Mesh Generation With The *snappyHexMesh* Tool

The *snappyHexMeshTool* is a meshing tool in the OpenFOAM software. It creates computational meshes using hexahedral cells around geometry in triangulated formats, such as stl, which is used in this case. It is also able to create computational meshes with respect to analytically defined geometry, such as planes, spheres and others. The tool can run in parallel, allowing for faster mesh generation.

Before the *snappyHexMesh* tool is run, it is necessary to create a background mesh using a tool named *blockMesh*. The *blockMesh* tool also creates the boundaries of the computational domain.

The meshing process executed by the *snappyHexMesh* is comprised by three basic procedures:

- Castellation, where the background cells are divided into smaller cells in close proximity to defined geometries.

- Snapping, where through an interactive process, the castellated mesh is projected and morphed in order to adapt to the input geometry.

- Adding layers, where prismatic cell layers are inserted in the void created by shrinking the mesh around user defined areas of the input geometry.[25]

In figure 3.1, the meshing process is depicted in an example model.
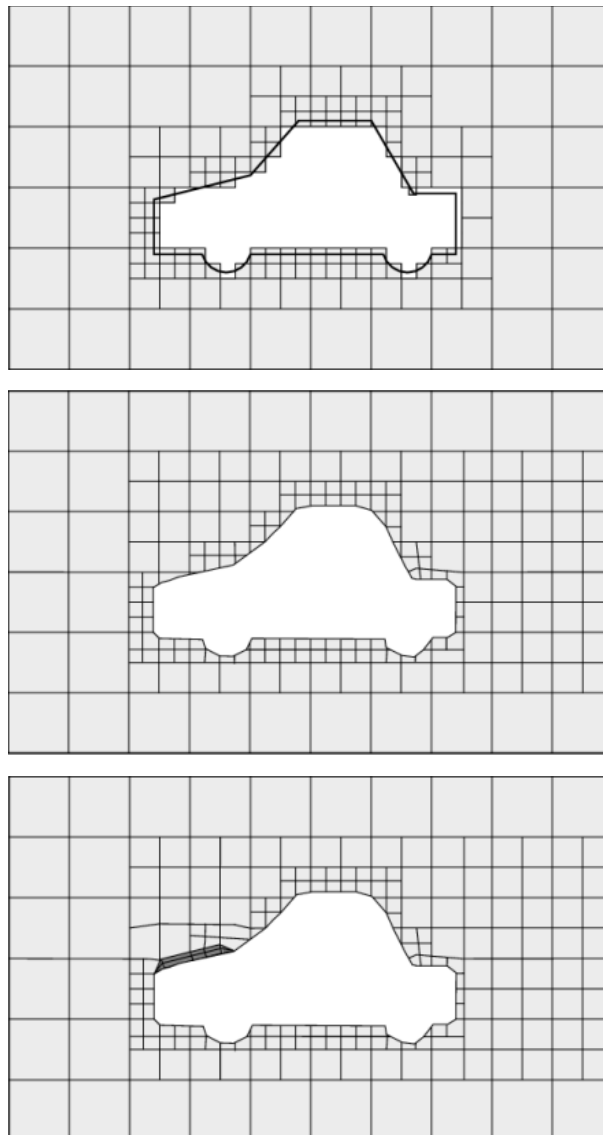
Figure 3.1: The meshing process using snappyHexMesh *in an example car model geometry. On top, the castellated mesh is shown, in the middle is the mesh after snapping and at the bottom the final mesh after layers have been added on the car bonnet is depicted.[26]*

3.2. Computational Space

3.2.1. In General

The computational domain in which the primal and adjoint flow equations are solved is defined using the *blockMesh* tool as a rectangular parallelepiped and its dimensions were allocated as such:

Total length: 70 m,

Total width: 5 m,

Total height: 8.3 m.

The dimensions above allow for adequate free space in front, on top, behind and beside the vehicle. The dimensions of this free space are presented in table 3.1.

Table 3.1: The dimensions of the free space around the vehicle.

Free Space	Total Size (m)	Length/Height Percentage
Front	19	4 times the car length
Top	6.9	4.9 times the car height
Behind	46	9.6 times the car length
Beside	5	5.6 times the car halfwidth

In order to monitor the mesh quality, the maximum aspect ratio, maximum and average cell skewness and maximum non-orthogonality were checked:

Maximum aspect ratio = 33.62.

Mesh non-orthogonality: Maximum: 64.73, Average: 7.59.

Maximum skewness = 5.83.

These indicate a mesh with no geometry flaws.

The mesh was composed of 4,846,058 cells.

In figure 3.2, the full computational domain with the model inside is shown.
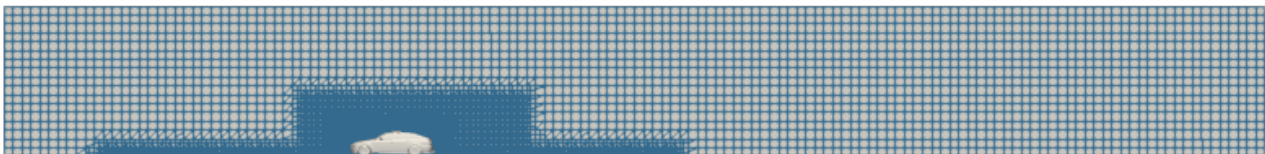
Figure 3.2: The computational domain with the vehicle model inside.

3.2.2. Refinement Spaces

Two refinement spaces are created, one with high refinement levels for the model and one with medium refinement levels for the model and its wake. The space in close proximity to and above the road is also refined.

Those two refinement space are shown in figure 3.3 in side view and in figure 3.4 in front view, with respect to the model.
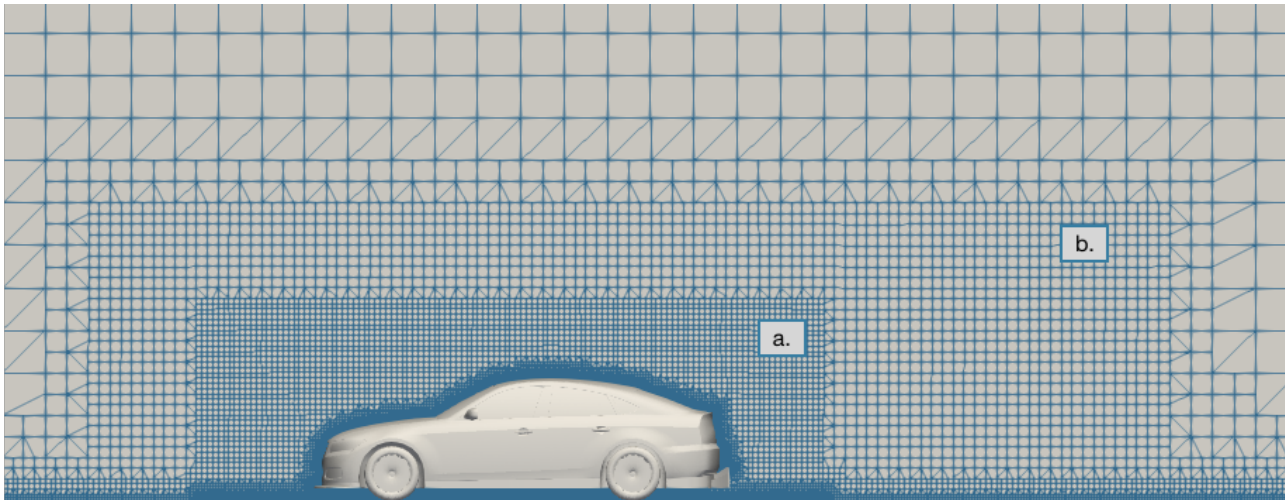
Figure 3.3: The refinement areas for the vehicle (a) and its wake (b), in side view.
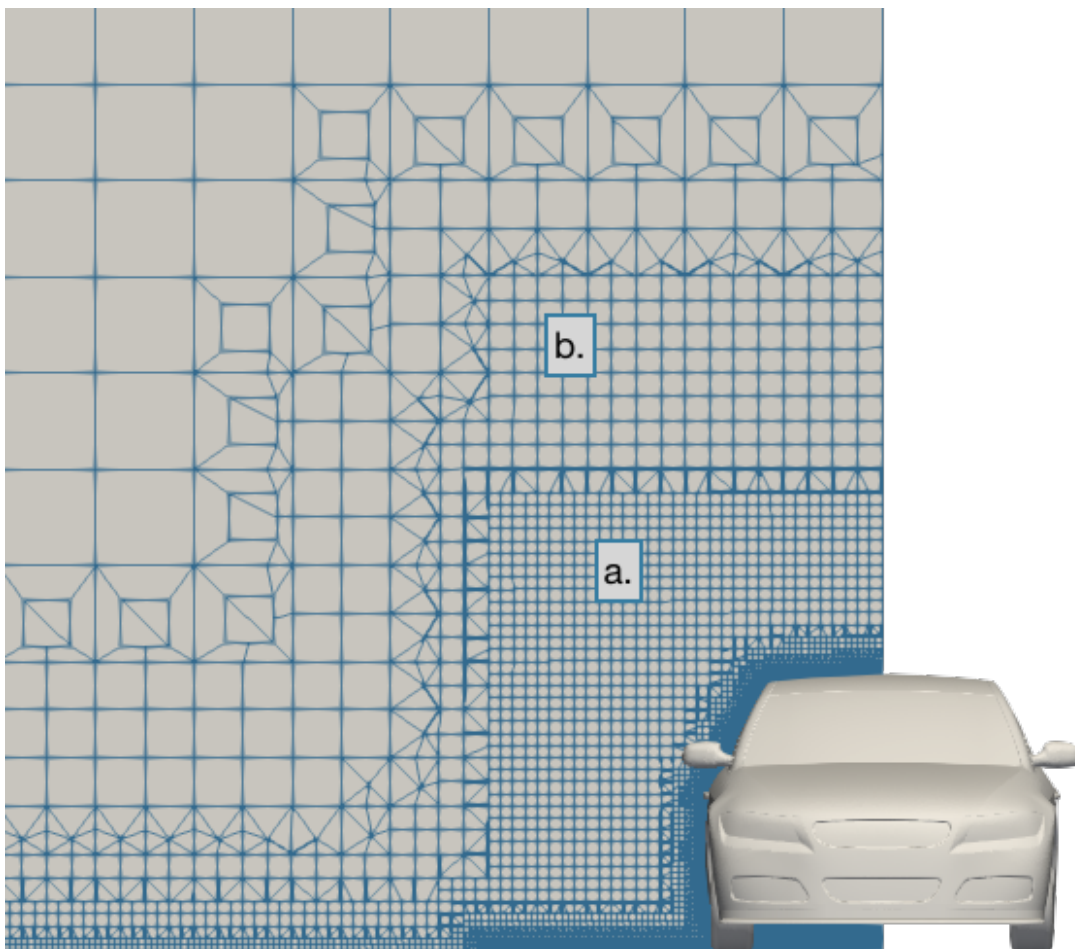
Figure 3.4: The refinement areas for the vehicle (a) and its wake (b), in front view.

3.2.3. Mesh Details

In the following figures, selected details of the mesh are presented.
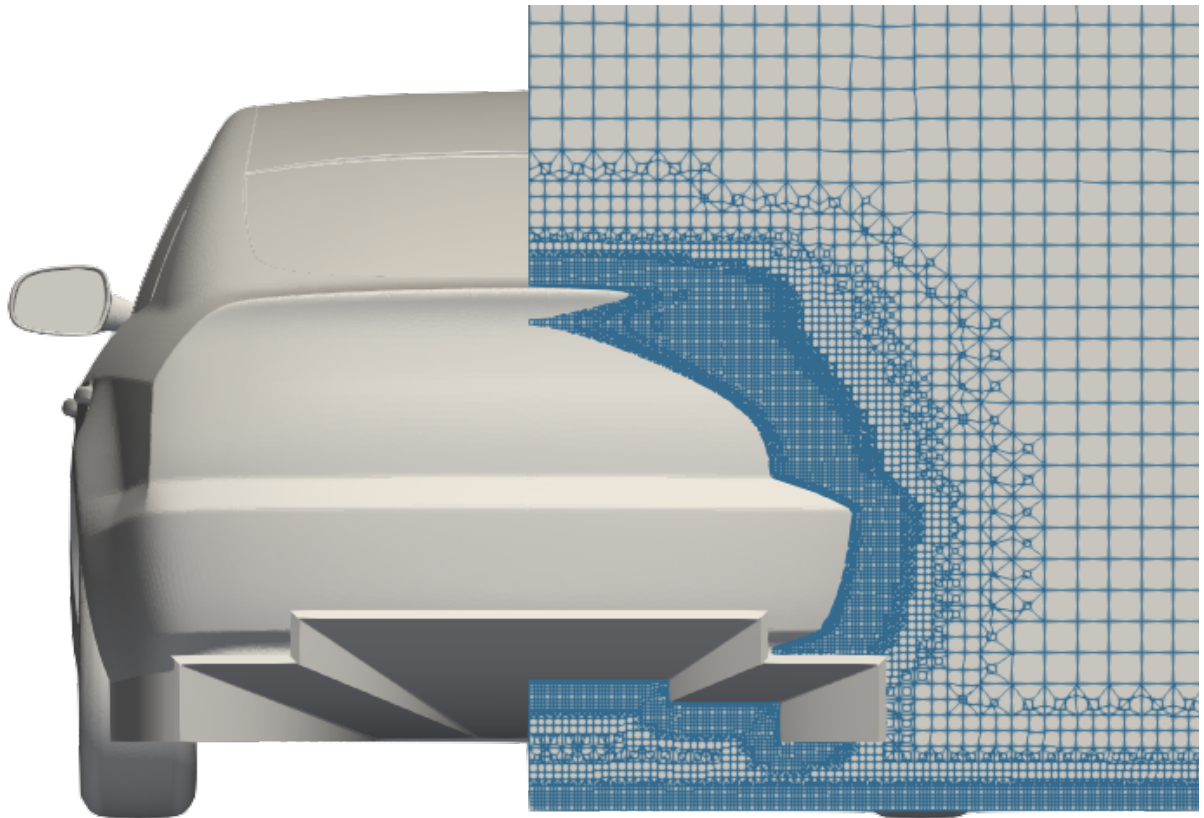
Figure 3.5: Mesh detail at the rear.
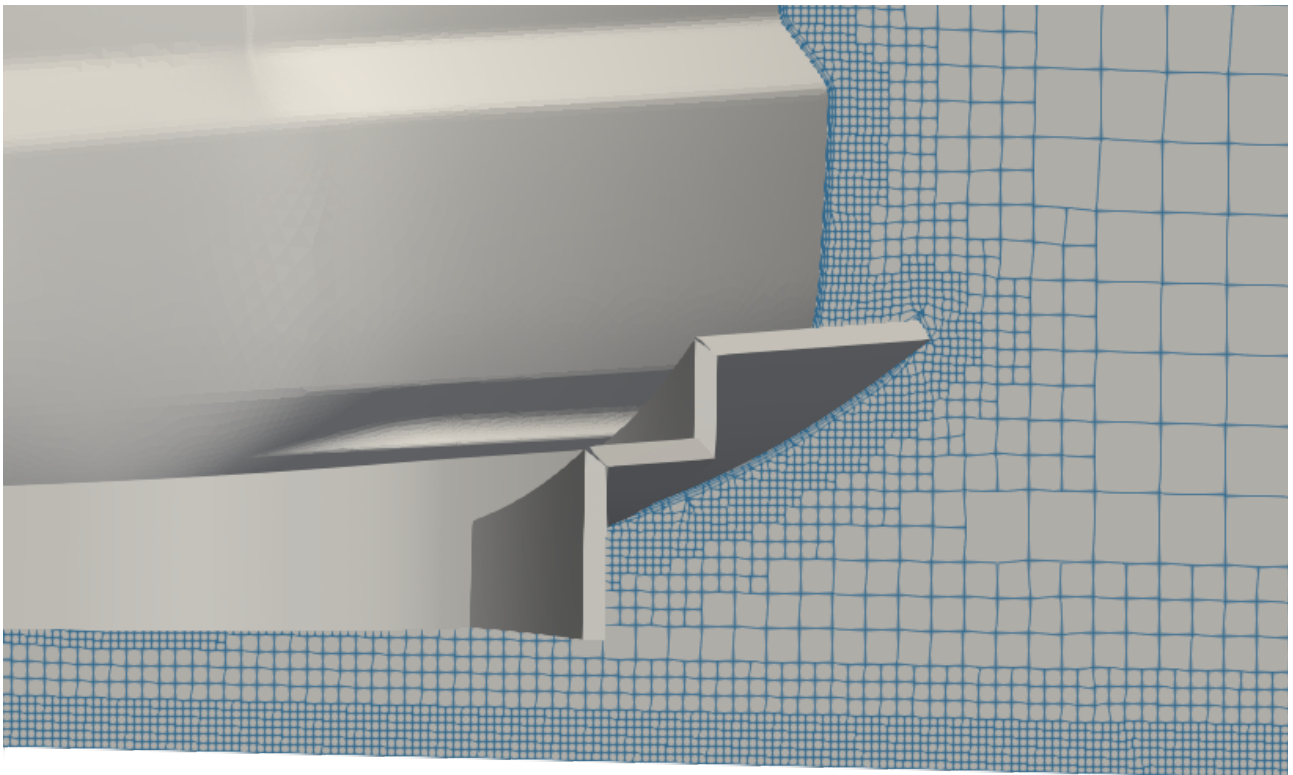
Figure 3.6: Mesh detail at the rear diffuser.
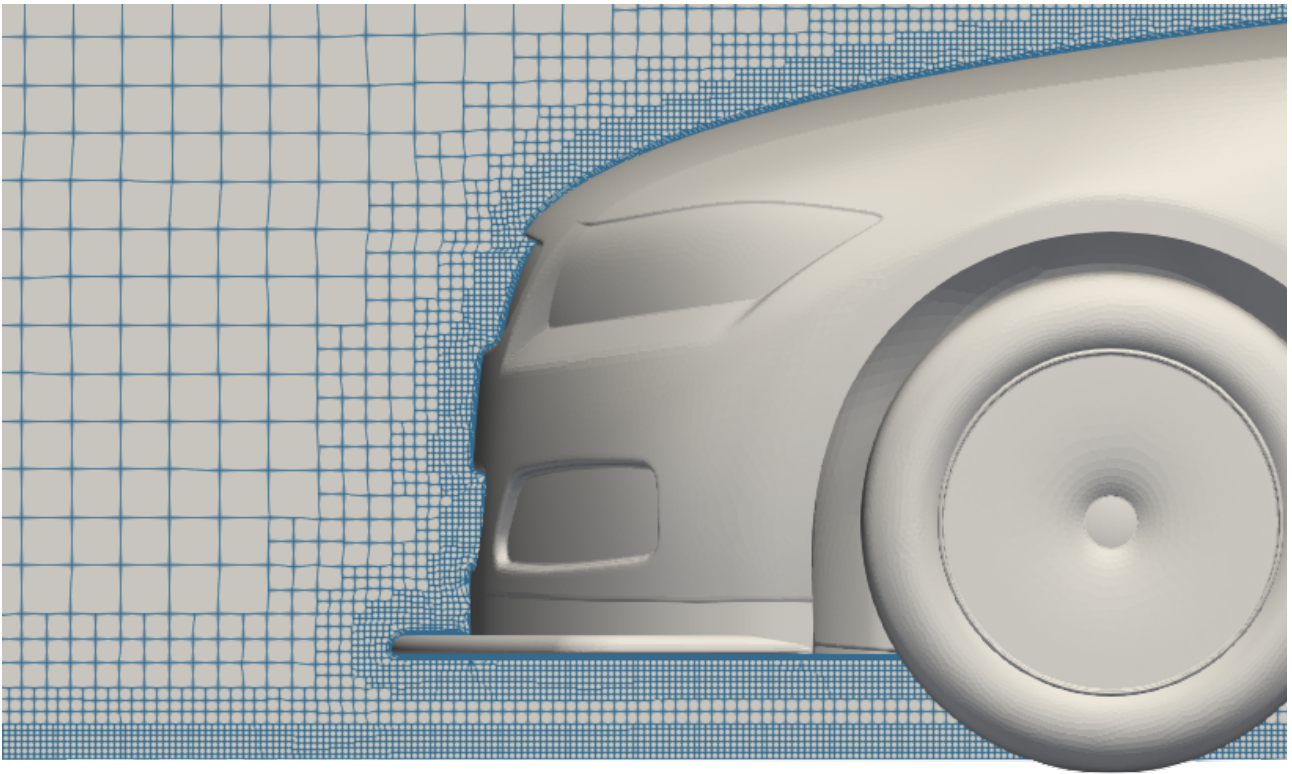
Figure 3.7: Mesh detail at the front splitter.
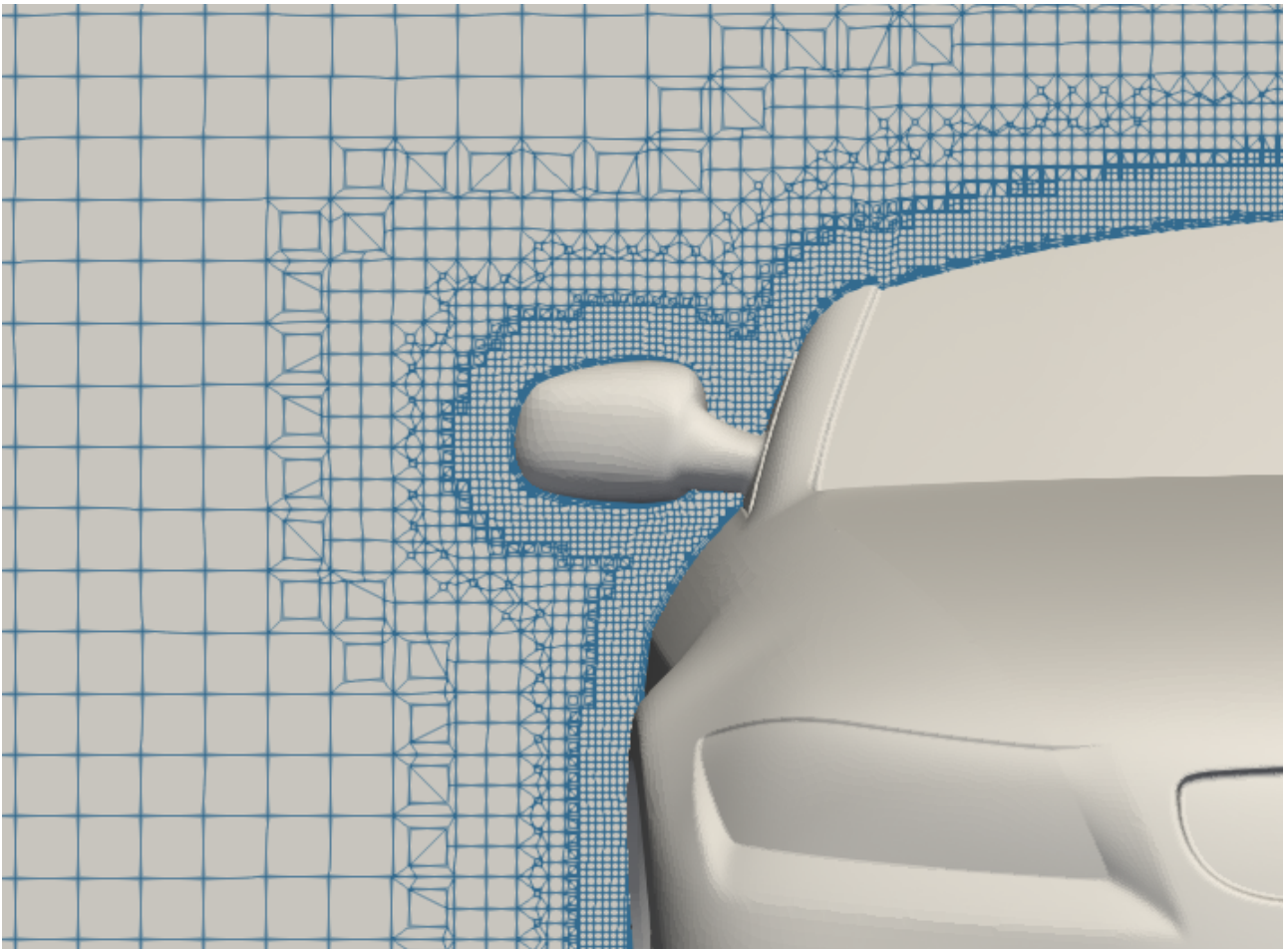
Figure 3.8: Mesh detail at the wing mirrors.
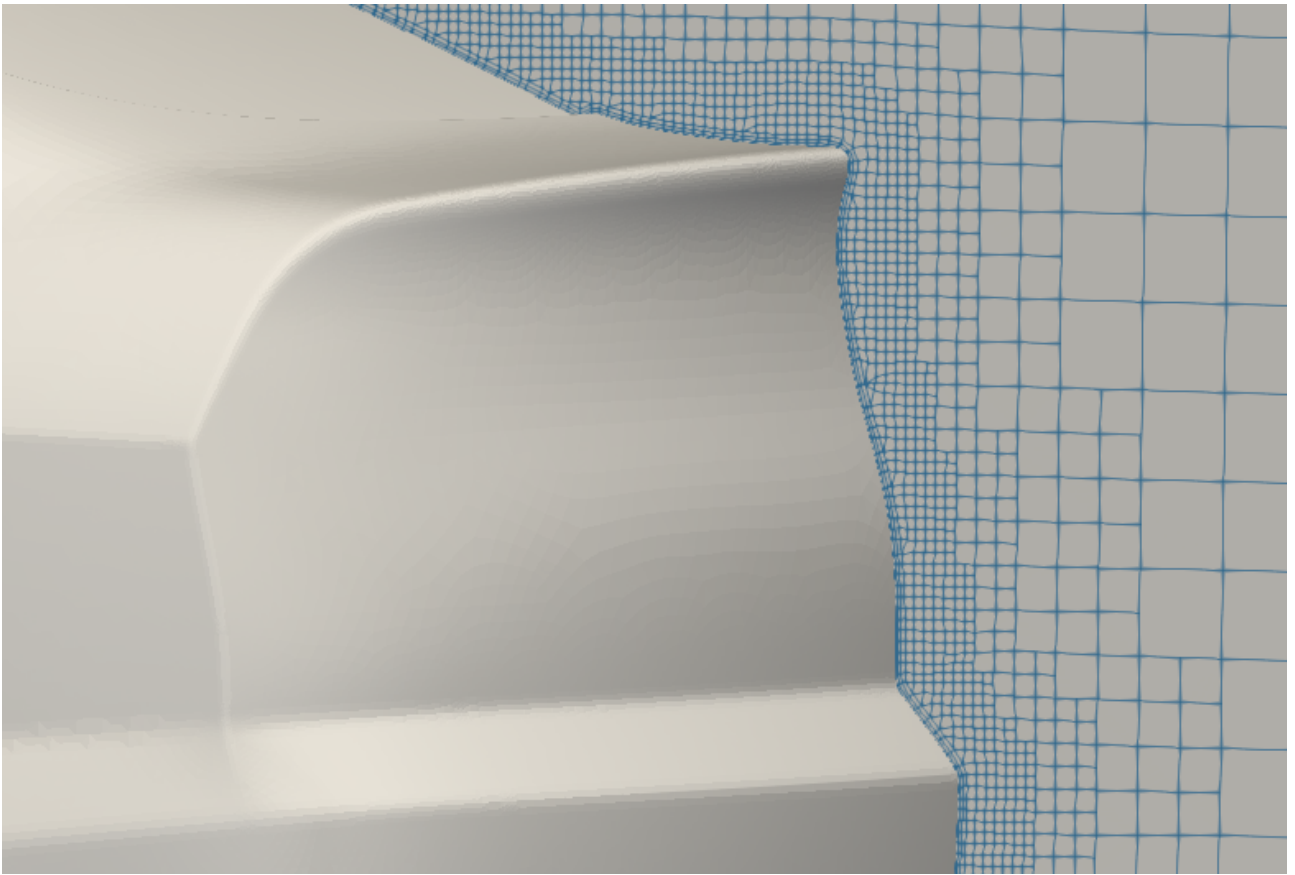
Figure 3.9: Mesh detail at the rear spoiler.

4. The Primal Flow Problem

4.1. Flow Equations

4.1.1. Theoretical Background

4.1.1.A. The Navier—Stokes Equations

Before the flow equations are introduced, it is noted that the simulation Mach number is relatively low, below 0.3. Thus, the effect of the air compressibility is almost negligible and the following equations concern the incompressible fluid flow.

The Navier—Stokes equations concerning incompressible Newtonian fluids are the following:[27]

4.1.
$$\frac{\partial u_j}{\partial x_j} = 0$$

4.2.
$$\frac{\partial u_i}{\partial t} + u_j \frac{\partial u_i}{\partial x_j} = -\frac{\partial p}{\partial x_i} + \frac{\partial}{\partial x_j}\left[\left(\nu + \nu_t\right)\left(\frac{\partial u_i}{\partial x_j} + \frac{\partial u_j}{\partial x_i}\right)\right]$$

where:

- Indices i and j: Indicate directions x, y and z; A twice repeated index implies summation according to Einstein's convention.

- u_i: Velocity component at direction i,

- x_i: Cartesian coordinate of space at direction i,

- t: Time,

- p: Static pressure divided by the constant density ρ,

- ν: Kinematic viscosity of the fluid.

Equation *(4.1)* is the continuity equation and equation *(4.2)* is the momentum conservation equation. These equations are integrated over every finite volume of the cells and are solved numerically using appropriate methods.

An alternative notation for the two equations is R^p and R^{u_j}, respectively, ignoring the time derivative for steady flows, since steady simulations are performed, is:

4.3.
$$R^p = -\frac{\partial u_j}{\partial x_j} = 0$$

4.4.
$$R^u{}_j = u_j \frac{\partial u_i}{\partial x_j} + \frac{\partial p}{\partial x_i} - \frac{\partial}{\partial x_j}\left[\left(\nu + \nu_t\right)\left(\frac{\partial u_i}{\partial x_j} + \frac{\partial u_j}{\partial x_i}\right)\right] = 0$$

4.1.1.B. Turbulence

4.1.1.B.a. About Turbulence

A summarized description of the phenomenon of turbulence, as stated by Lewis Richardson, is as follows:

Big whirls have little whirls that feed on their velocity, and little whirls have lesser whirls and so on to viscosity.[28]

The nature of a turbulent flow is chaotic. The exact computation of the flow behaviour is almost impossible. For this reason, turbulence models have been created using statistical and experimental data of turbulent flows.

For the majority of turbulent flow cases, the simplest models are derived from the application of time averaging on the original Navier—Stokes equations. The resulting equations are named Reynolds Averaged Navier—Stokes equations, or RANS for short. Time averaging means discretizing a quantity between its mean value across a large time duration and its time-dependent oscillation around this value. For example, a velocity component u is time averaged as such:

4.5.
$$u(x,t) = \bar{u}(x) + u'(x,t)$$

where:

- $\bar{u}$: The mean value of the velocity component over a time duration,
- u': The velocity component oscillation around the mean value.

In figure 4.1 the distinction between $\bar{u}$ and u' is demonstrated.
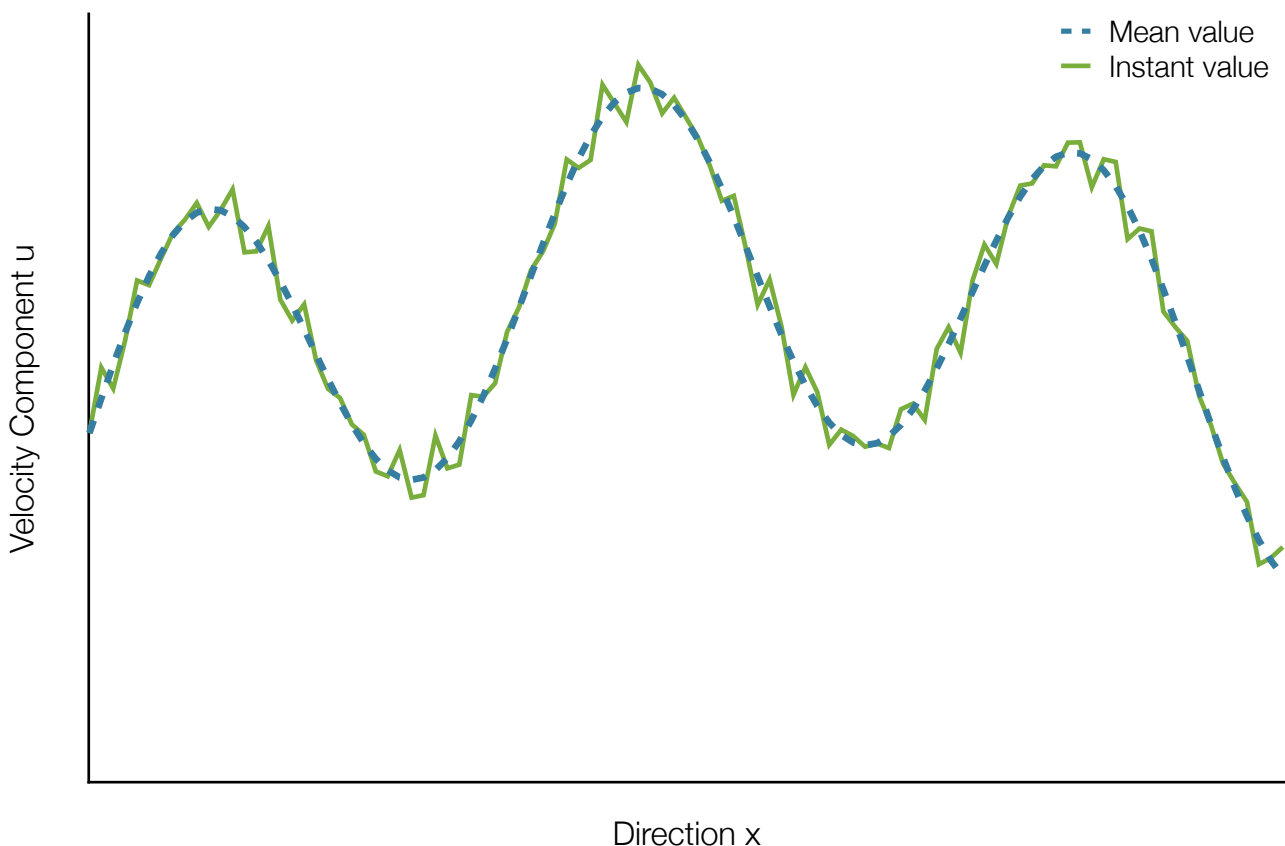
Figure 4.1: The distinction between the mean value of the velocity component u *over a time duration (blue dashed line) and the time dependent velocity component oscillation around the mean value (green continuous line).*

The time averaged momentum equation is:

4.6.
$$\overline{u}_j \frac{\partial \overline{u}_i}{\partial x_j} = \overline{f}_i + \frac{\partial}{\partial x_j}\left[-\overline{p}\delta_{ij} + v\left(\frac{\partial \overline{u}_i}{\partial x_j} + \frac{\partial \overline{u}_j}{\partial x_i} \right) - \overline{u_i' u_j'} \right]$$

where:

- δ_{ij}: The Kronecker's delta, which is equal to 0, when $i \neq j$ and equal to 1 when $i=j$,

- The Reynolds stresses $-\overline{u_i' u_j'}$ are modelled using the Boussinesq hypothesis as:[29]

4.7.
$$-\overline{u_i' u_j'} = v_t\left(\frac{\partial \overline{u}_i}{\partial x_j} + \frac{\partial \overline{u}_j}{\partial x_i} \right) - \frac{2}{3}k\delta_{ij}$$

where:

- k is the turbulence kinetic energy, defined as:

4.8.
$$k = \frac{1}{2}\overline{u_i' u_i'}$$

- v_t: The turbulent kinematic viscosity.

4.1.1.B.b. The Spalart—Allmaras Turbulence Model

The Spalart—Allmaras model is a one equation turbulence model turbulence model. It was developed primarily for external air flows. The model introduces a new variable, $\tilde{v}$, which is defined by the following equation:[30]

4.9.
$$\nu_t = \tilde{v} f_{u_1}$$

where:

- f_{u1}: A quantity defined as:

4.10.
$$f_{u_1} = \frac{X^3}{X^3 + C_{u_3}^{\ 3}}$$

where:

- X: The ratio of $\tilde{v}$ to kinematic viscosity:

4.11.
$$X = \frac{\tilde{v}}{\nu}$$

The partial differential equation of the Spalart—Allmaras turbulence model is the following:

4.12.
$$R^{\tilde{v}} = u_j \frac{\partial \tilde{v}}{\partial x_j} - C_{b_1}\left(1 - f_{t_2}\right)\tilde{S}\tilde{v} + \left(C_{w_1}f_w - \frac{C_{b_1}}{\kappa^2}f_{t_2}\right)\left(\frac{\tilde{v}}{d}\right)^2 - \frac{1}{\sigma}\left[\frac{\partial}{\partial x_j}\left[(\nu + \tilde{v})\frac{\partial \tilde{v}}{\partial x_j}\right] - C_{b_2}\frac{\partial \tilde{v}}{\partial x_i}\frac{\partial \tilde{v}}{\partial x_i}\right] = 0$$

where:

- d: The distance of each point to the nearest wall,
- The following quantities are constants of the model:
    - $\sigma = 2/3$,
    - $C_{b1} = 0.1355$,
    - $C_{b2} = 0.622$,
    - $\kappa = 0.41$,
    - $C_{w1} = 3.239$,
    - $C_{w2} = 0.3$,
    - $C_{w3} = 2$,
    - $C_{u1} = 7.1$,
    - $C_{t3} = 1.2$,
    - $C_{t4} = 0.5$,
- The following equations are used for computation of the rest of the model quantities:[31]

4.13.
$$\tilde{S} = \Omega + \frac{\tilde{v}}{\kappa^2 d^2} f_{u_2}$$

4.14.
$$\Omega = \sqrt{2W_{ij}W_{ij}}$$

4.15.
$$W_{ij} = \frac{1}{2}\left(\frac{\partial u_i}{\partial x_j} - \frac{\partial u_j}{\partial x_i}\right)$$

4.16.
$$f_{u_2} = 1 - \frac{X}{1 + Xf_{u_1}}$$

4.17.
$$f_w = g\left[\frac{1 + C_{w_3}^6}{g^6 + C_{w_3}^6}\right]$$

4.18.
$$g = r + C_{W_2}\left(r^6 - 6\right)$$

4.19.
$$r = \min\left\{\frac{\tilde{v}}{\tilde{S}\kappa^2 d^2}, 10\right\}$$

4.20.
$$f_{t_2} = C_{t_3} e^{-C_{t_3}X^2}$$

The production P and dissipation D terms are given by:

4.21.
$$P(\tilde{v}) = C_{b_1}\tilde{Y}$$

4.22.
$$D(\tilde{v}) = C_{w_1} f_w\left(\tilde{Y}\right)\frac{\tilde{v}}{d^2}$$

where:

4.23.
$$\tilde{Y} = Yf_{u_3} + \frac{\tilde{v}}{d^2\kappa^2}f_{u_2}$$

where Y is the vorticity magnitude:

4.24.
$$Y = \left|e_{ijk}\frac{\partial u_k}{\partial x_j}\right|$$

4.1.2. Boundary Conditions

4.1.2.A. On The Boundaries Of The Computational Domain

4.1.2.A.a. Inlet

At the inlet of the computational domain, the following boundary conditions are set:

- The velocity components (u_x, u_y, u_z) are set as (36, 0, 0) m/s on the inlet, as a Dirichlet boundary condition. The resulting inlet velocity magnitude of 36 m/s defines the Reynolds number, by implementing the following equation:

4.25.
$$\mathrm{Re} = \frac{U_\infty L_{ref}}{\nu}$$

where L_{ref}, a reference length of the geometry, which, in this Diploma Thesis, is the vehicle wheelbase, which is 2.786 m.

The flow Reynolds number is:

Re = 6.7×10^6

- The gradient of the pressure at the direction normal to the inlet is set to zero, as a Neumann boundary condition.
- The value of $\tilde{\nu}$ is set to 2.38×10^{-3} m^2/s, about five times the kinematic viscosity of air.[32]
- The value of the turbulent kinematic viscosity is set to 2.38×10^{-3} m^2/s.

4.1.2.A.b. Outlet

At the outlet of the computational domain, the following boundary conditions are set:

- The gradient of the velocity components in the direction normal to the outlet is set to zero.
- The pressure at the outlet is set to zero.
- The gradient of $\tilde{\nu}$ at the direction normal to the outlet is set to zero.
- The gradient of the turbulent kinematic viscosity in the direction normal to the outlet is set to zero.

4.1.2.A.c. Road

The road is considered fixed, thus, the following boundary conditions are set:

- The velocity components are set to 0 m/s, as a Dirichlet boundary condition.
- The gradient of the pressure on the road in the direction normal to it is set to zero.
- The value of $\tilde{\nu}$ is set to zero.
- The boundary condition of the turbulent kinematic viscosity is set to a condition based on turbulent kinetic energy, using a wall function, defined by the following equation:

4.26.
$$\nu_t = \frac{u_\tau^{\,2}}{\dfrac{\partial u}{\partial n}} - \nu$$

where:

- u_τ: Friction velocity, defined by:

4.27.

$$u_\tau = \sqrt{\frac{\tau_w}{\rho}}$$

- $\boldsymbol{n}$: The normal to the surface unit vector.[33]

4.1.2.A.d. Side & Top

At the side and top of the computational domain, the following boundary conditions are set:

- The boundary condition for the velocity provides a slip constraint.

- The gradient of the pressure on the side and top of the computational domain in the direction normal to each of them is set to zero.

- The gradient of $\tilde{v}$ at the direction normal to the surface is set to zero.

- The gradient of the turbulent kinematic viscosity in the direction normal to the surface is set to zero.

4.1.2.A.e. Symmetry Plane

At the symmetry plane, a boundary condition named *symmetryPlane* is implemented for all quantities, modelling the symmetry of the simulation.

4.1.2.B. On The Vehicle

On the vehicle, the following boundary conditions were set:

- The velocity is set to zero on the body of the car.

- The gradient of the pressure in the direction normal to the surface is set to zero.

- The value of $\tilde{v}$ is set to zero.

- The boundary condition of the turbulent kinematic viscosity is set to a condition based on turbulent kinetic energy, using a wall function, the same one used on the road.

4.1.3. Forces

4.1.3.A.

The aerodynamic forces on a body in a stream of fluid are due to pressure and shear distribution over the body surface.[34] The two forces that are of interest are drag **D** and lift **L**. These are components of the total force **F** that is exerted from a fluid to a body, that is computed by the following equation:[35]

4.28.
$$\vec{F} = \oiint_S p n_i \, ds - \oiint_S \tau_{ij} n_j \, ds$$

where:

- **n**: The normal to the surface unit vector,
- **t**: The tangent to the surface unit vector,
- τ_{ij}: The shear stress components on the body surface.

The drag **D** is the component of **F** parallel to the free stream flow and the lift **L** is the component perpendicular to it.

The aerodynamic performance of a body concerning drag and lift are often stated using the respective drag and lift coefficients, defined as:

4.29.
$$C_D = \frac{D}{\frac{1}{2} \rho_\infty A_{ref} U_\infty}$$

4.30.
$$C_L = \frac{L}{\frac{1}{2} \rho_\infty A_{ref} U_\infty}$$

where:

- ρ_∞: The fluid free stream density,
- A_{ref}: A reference area for the body. In this case, this is the frontal area of the car,
- U_∞: The fluid free stream velocity.[36]

4.2. Numerical Solution Using OpenFOAM

The steady-state simulation is carried out using the SIMPLE algorithm, according to the following procedure:

- The discretized momentum equation is solved and an intermediate velocity field u^* is computed, using an initial estimation or previous iteration data for the pressure gradient:

4.31.
$$a_P u^*_{P,i} = \sum_{N=1}^{NB(P)} a_N u^*_{N,i} - \frac{\partial p^*}{\partial x_i} + b^*_i$$

where:

- P: The cell index in which the momentum equations are discretized,
- $NB(P)$: Its adjacent cells,
- b: A vector referring to explicitly considered source terms that might be present in the momentum equations,
- a_P and a_N: Coefficients that result from the discretization of the convection and diffusion terms in equation (4.4) It should be noted that the diagonal coefficient a_P is the same for all the components of the momentum equations,
- p^*: Initial estimation or previous iteration pressure data,

- The following equation for the pressure is formed and solved, determining the new pressure field that satisfies the continuity equation:

4.32.
$$\frac{\partial}{\partial x_j}\left(\frac{1}{a_P}\frac{\partial p}{\partial x_j}\right) = \frac{\partial \hat{u}_{P,j}}{\partial x_j}$$

where:

4.33.
$$\hat{u}_{P,j} = \frac{1}{a_P} H_{P,j}\left(\mathbf{v}^*\right)$$

4.34.
$$H_{P,j}\left(\mathbf{v}^*\right) = \sum_{N=1}^{NB(P)} a_N u^*_{N,j} + b^*_j$$

- Relaxation is applied to certain flow quantities,
- The fluid volume flux at the mesh faces m_f is updated, using the following equation:

4.35.
$$m_f = u_{f,j} S_{f,j} = \overline{\hat{u}_{f,j}} S_{f,j} - \frac{1}{a_f}\left(\frac{\partial p}{\partial x_j} S_j\right)_f$$

where:

- **S**: The normal to the surface vector dimensionalized with the surface area,

- $\left(\dfrac{\partial p}{\partial x_j} S_j\right)_f$: The normal to the surface pressure gradient,

- The velocities are corrected according to the new pressure field, using the following equation:

4.36.
$$u_{P,i} = \hat{u}_{P,i} - \frac{1}{a_P}\frac{\partial p}{\partial x_i}$$

- The boundary values of the flow quantities are renewed,
- The cycle repeats until adequate convergence has been achieved.[37]

This algorithm is set by creating the necessary OpenFOAM case documents. The desired initial and boundary conditions are set, along with numerous other parameters concerning the computational processes. An initialization is computed by solving the potential flow, using the *potentialFoam* tool. Then, the steady-state Navier—Stokes equations and the turbulence model equations are solved according to the aforementioned SIMPLE algorithm, using the *simpleFoam* tool.

The discretization of the equations is second order accurate. In table 4.1, the discretization schemes used are listed.[38]

Table 4.1: The discretisation schemes used in the simulation.

Operation	Discretization Scheme	
	Name	Meaning
∇	cellLimited Gauss linear	Cell Limited, Second Order, Gaussian Integration
$\nabla\cdot$	bounded Gauss linearUpwind	Second Order, Bounded
∇^2	Gauss linear corrected	Second Order, Unbounded

Consequently, the flow model is second order accurate. The relaxation factors are set to 0.2 for the pressure, the velocity and the $\tilde{v}$ variable.

4.3. Results

4.3.1. Convergence

4.3.1.A. Flow Quantities

The residuals of the flow equations for the modified car model during the simulation are presented in figure 4.2.
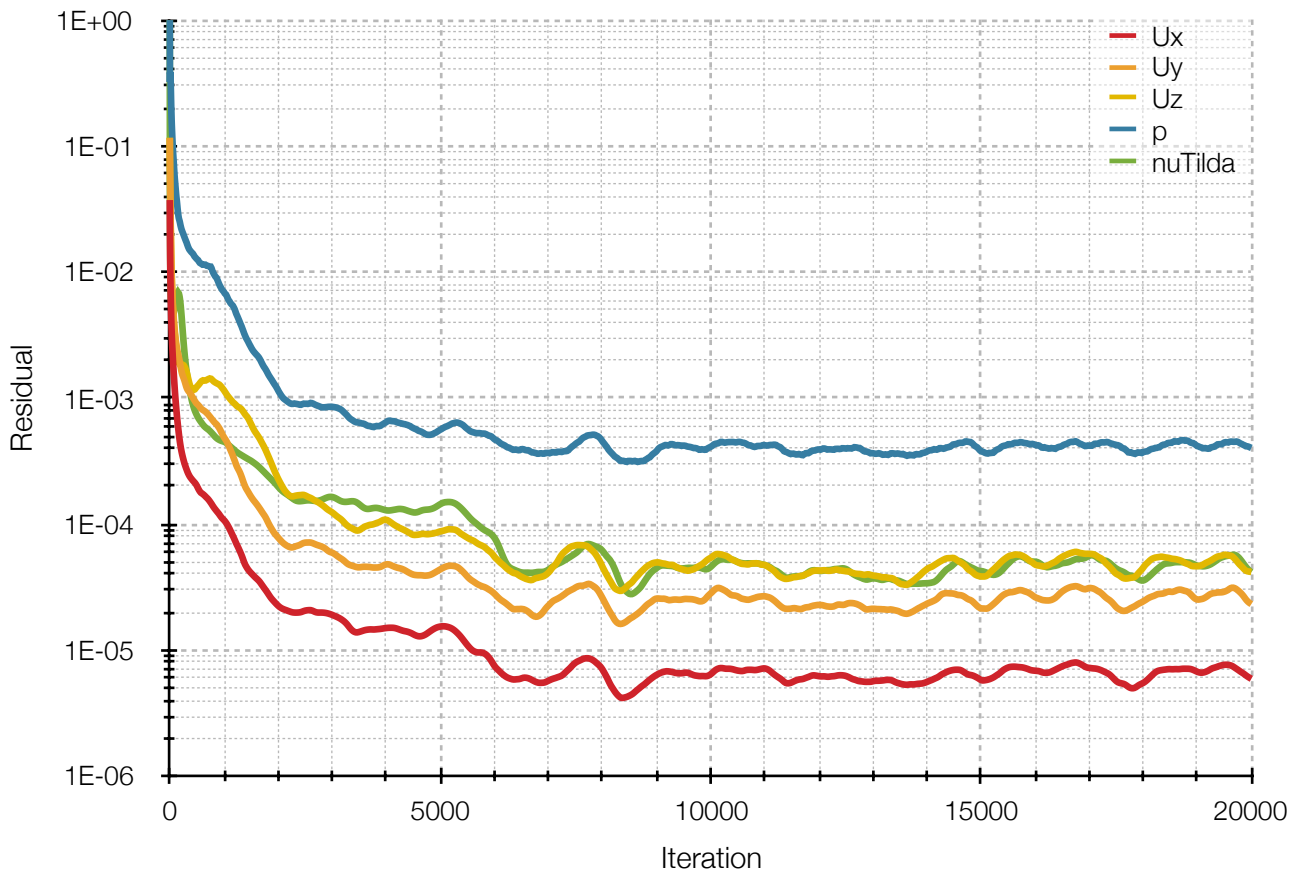
Figure 4.2: Convergence of the residuals of the flow equations during the simulation of the modified model.

It is clearly shown that the mean value of the residuals has been converged. The residuals are oscillating around this mean value.

In the following, the last iteration is considered as the solution.

4.3.1.B. Forces

The convergence of the force coefficients during the simulation of the modified model is presented in figure 4.3.
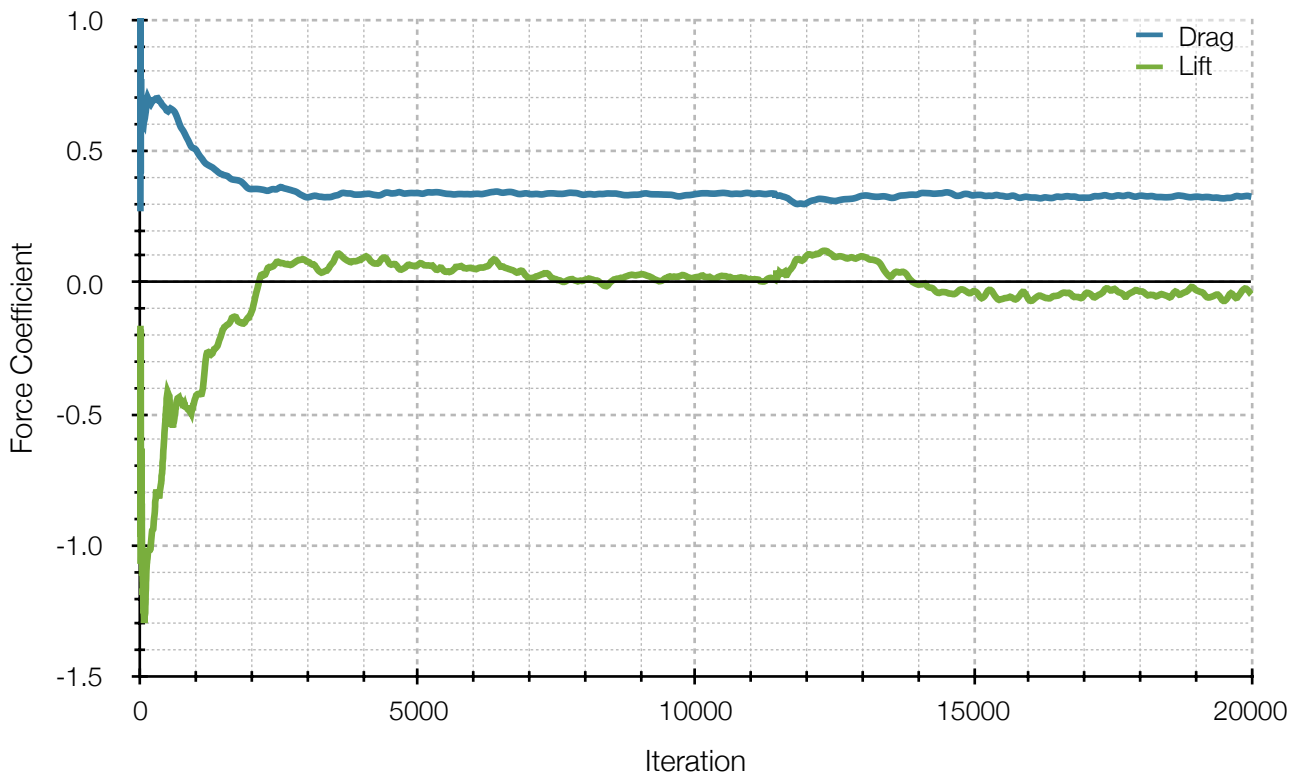
Figure 4.3: The convergence of the force coefficients during the simulation of the modified model.

Again, the mean values of the force coefficients have been stabilized.

The car body produces a negative overall effect of lift, meaning it produces downforce.

The mean value of the coefficients of the last 1000 iterations are considered the results. These mean values with their corresponding standard deviations σ are:

μ_{CD} = **0.326,**

σ_{CD} = **0.003,**

μ_{CL} = **-0.046,**

σ_{CL} = **0.014.**

4.3.2. Comparison With The Original Geometry

4.3.2.A. Forces

In table 4.2 a comparison between the force coefficient of the original DrivAer geometry and the modified model is presented.

Table 4.2: Aerodynamic coefficients of the original models and the modified DrivAer model.

Model	Coefficient	
	Drag	Lift
Original DrivAer	0.365	0.116
Modified DrivAer	0.326	-0.046
Difference To Original (%)	-10.68%	-139.66%

It is clear that the overall aerodynamic performance is improved. There is a 11% decrease on drag and a 140% decrease on lift, meaning that the vehicle is creating negative lift, that is net downforce.

The reduction in the lift gives way to more aggressive aerodynamic solutions, such as the introduction of a rear wing, the increase in the vehicle rake, the increase in the diffuser tip angle, an increase in the spoiler size and the introduction of winglets at certain places such as the front bumpers.

It is also noted that the final optimized solution is expected to give better results for the lift, however there may be an increase of drag, since the optimization process may automatically tend to implement some of the aforementioned more aggressive solutions.

4.3.2.B. Flow Field

4.3.2.B.a. Velocity Magnitude

In figure 4.4, the computed fields for the velocity magnitude are shown, for the original DrivAer geometry and the modified one.
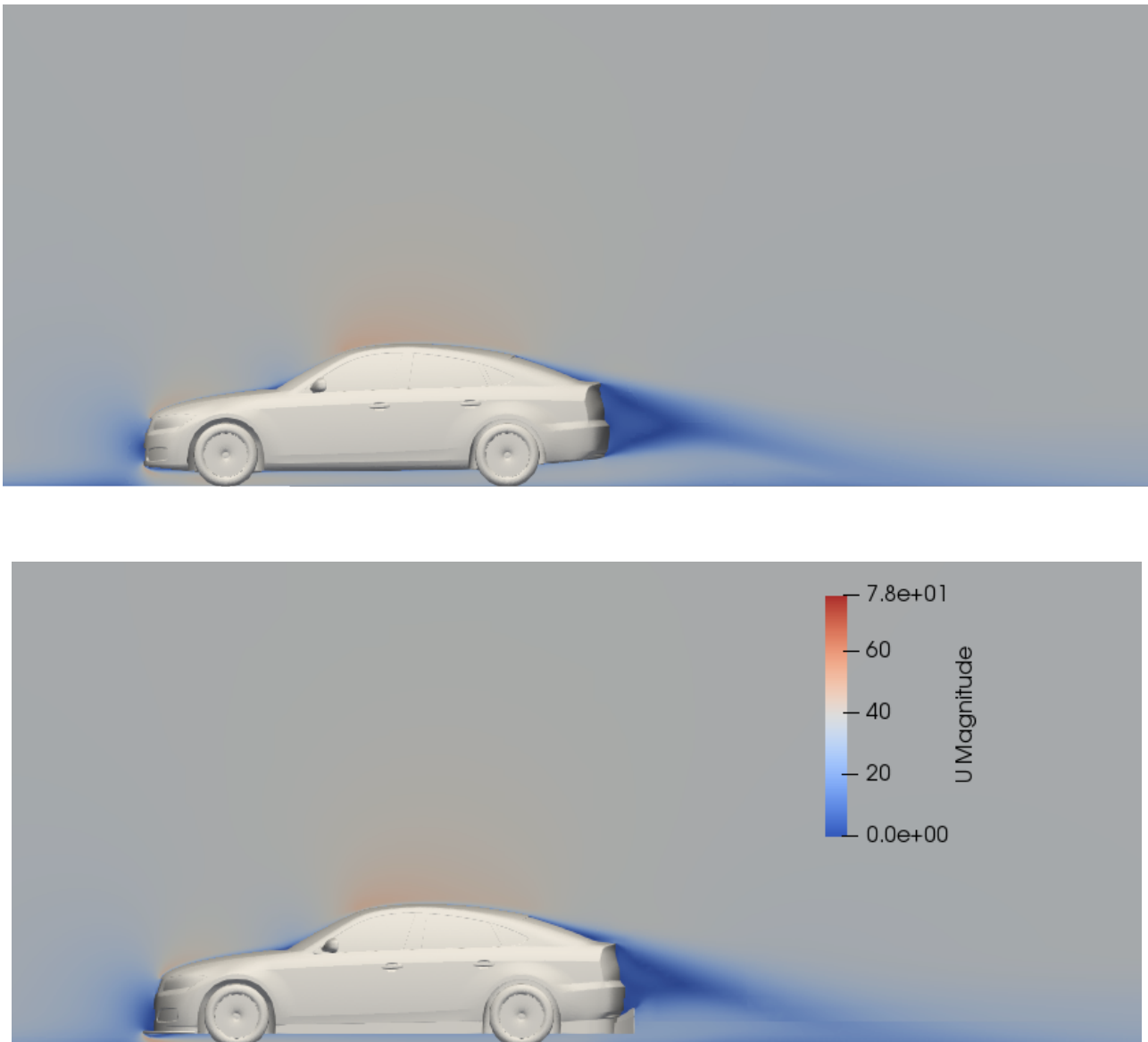
Figure 4.4: Velocity magnitude field for the original geometry (top) and for the geometry with the LM GTE modifications (bottom). The colour scale is the same for the two fields and the units are m/s.

The following remarks can be made:

- There are clear differences in the wake of the car. The wake is slightly shorter in the modified geometry.

- The airflow is faster under the floor of the modified geometry, thus pressure is less and downforce is created.

- The underbody upsweep is also visible right behind the diffuser.

- On both models the magnitude of the velocity is maximum on the roof of the car, decreasing the pressure and inducing lift.

4.3.2.B.b. Pressure

4.3.2.B.b.I. Symmetry Plane

In figure 4.5, the resultant fields for the pressure are shown, for the original DrivAer geometry and the modified one at the symmetry plane.
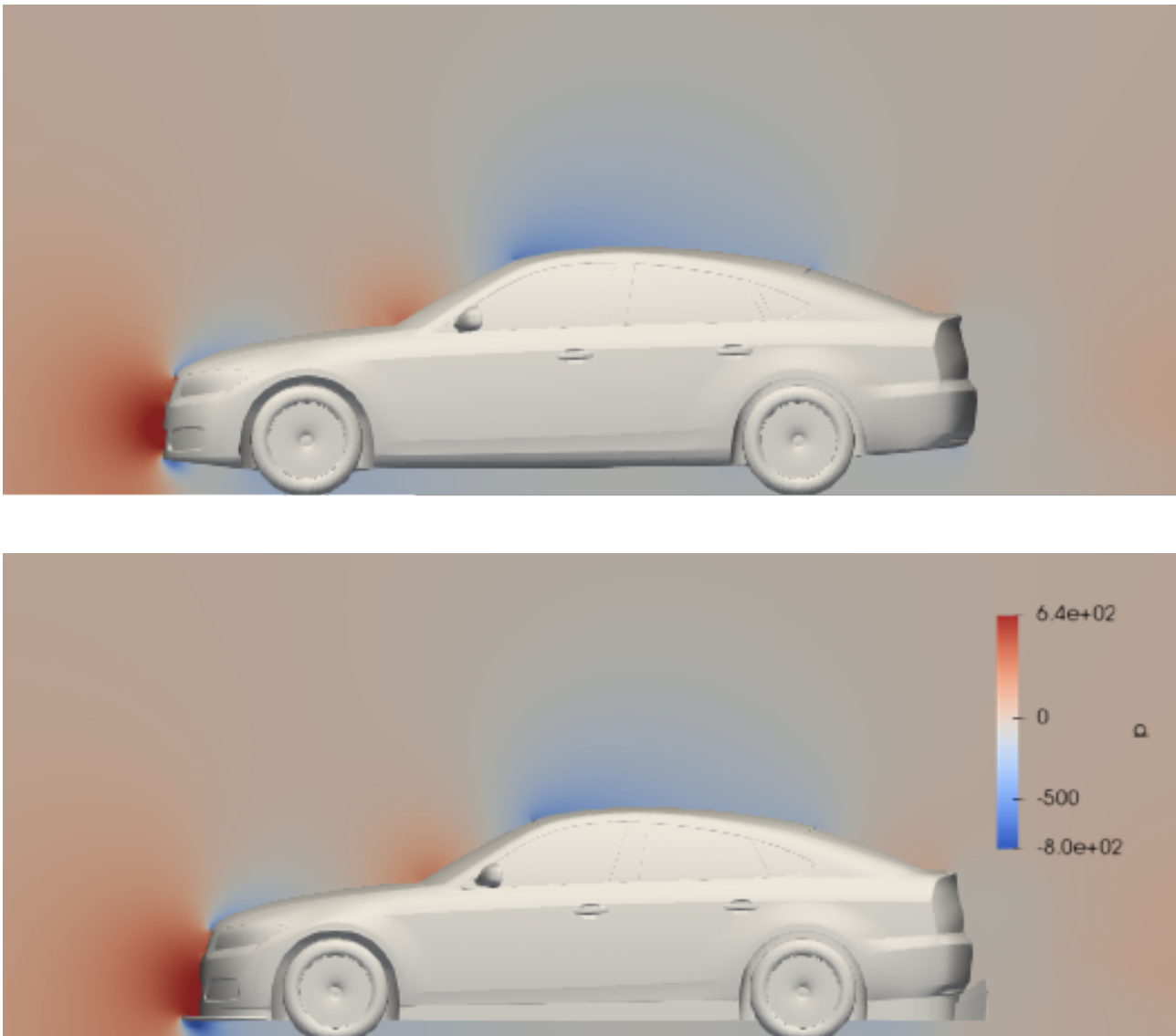
Figure 4.5: Pressure field for the original geometry (top) and for the geometry with the LM GTE modifications (bottom). The colour scale is the same for the two fields and the units are Pa, with the zero set to the ambient pressure

The following are noted:

- The pressure on the upper side of the splitter is relatively high, while on the bottom side it is relatively low, creating downforce at the front of the car.

- The pressure seems relatively smaller under the underfloor of the modified car.

- There is a low pressure zone on the roof of both cars, which combined with the moderate underfloor pressure induces lift.

In figures 4.6 to 4.9, a comparison of the pressure distribution on the car body is presented. Half of the car is the original geometry and half of the car is the geometry with the modifications.
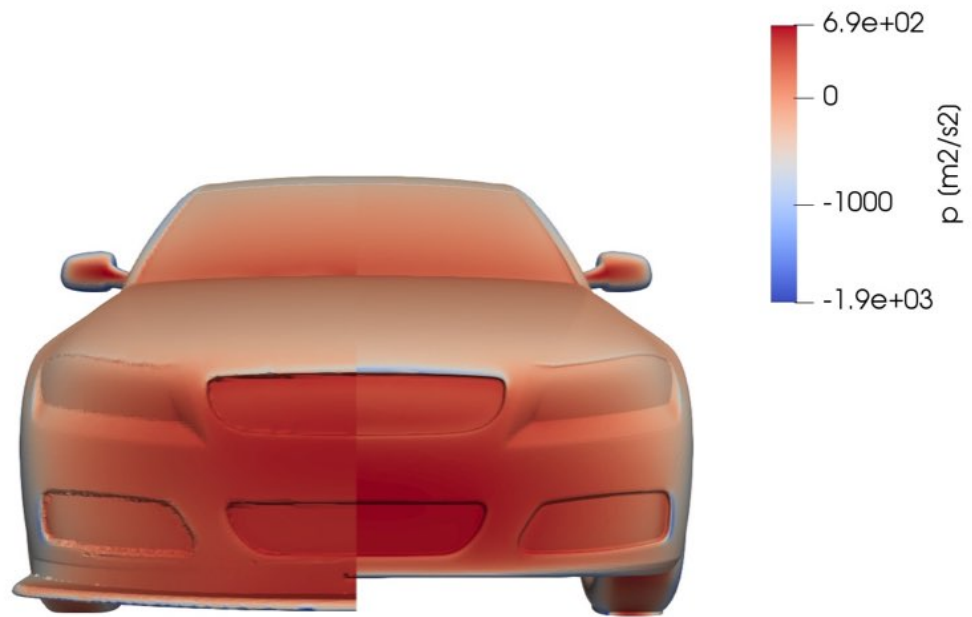
Figure 4.6: Comparison of the pressure distribution on the car body, between the original car geometry (port side) and the modified geometry (starboard side), in front view. The colour scale is the same for the two fields and the zero is set to the ambient pressure.
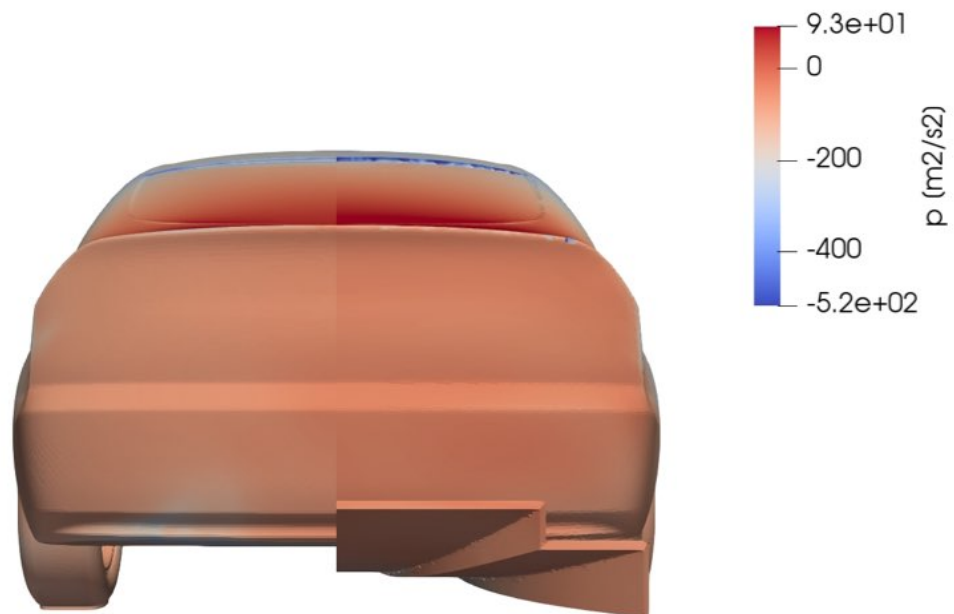
Figure 4.7: Comparison of the pressure distribution on the car body, between the original car geometry (port side) and the modified geometry (starboard side), in rear view. The colour scale is the same for the two fields and the zero is set to the ambient pressure.
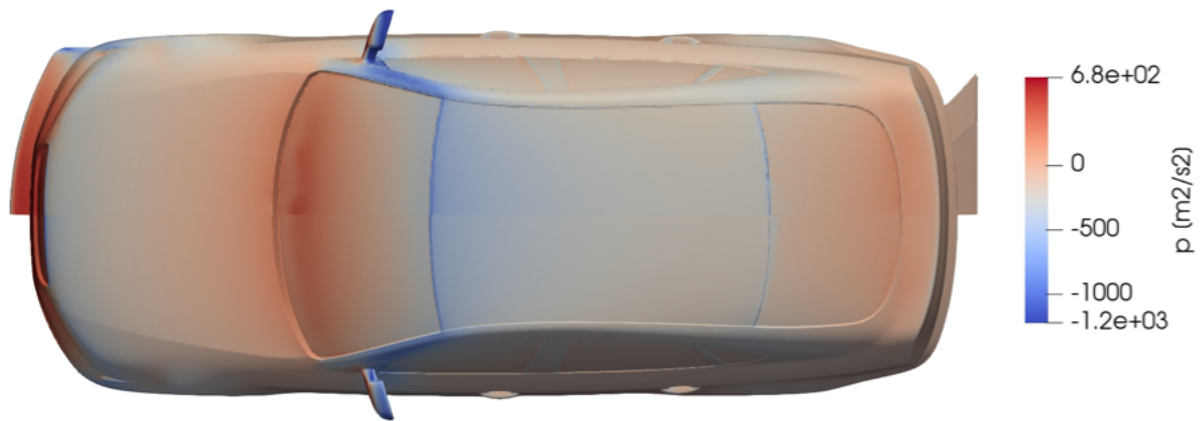
Figure 4.8: Comparison of the pressure distribution on the car body, between the original car geometry (bottom) and the modified geometry (top), in top view. The colour scale is the same for the two fields and the zero is set to the ambient pressure.

Figure 4.9: Comparison of the pressure distribution on the car body, between the original car geometry (top) and the modified geometry (bottom), in bottom view. The colour scale is the same for the two fields and the zero is set to the ambient pressure.

In addition to the previous points, it is noted that the pressure distribution at the underfloor is more uniform with the modified floor. However, the pressure distribution is relatively similar between the two models.

In figure 4.10, the variable $\tilde{v}$ field is shown for the original DrivAer geometry and the modified one, at their symmetry plane.
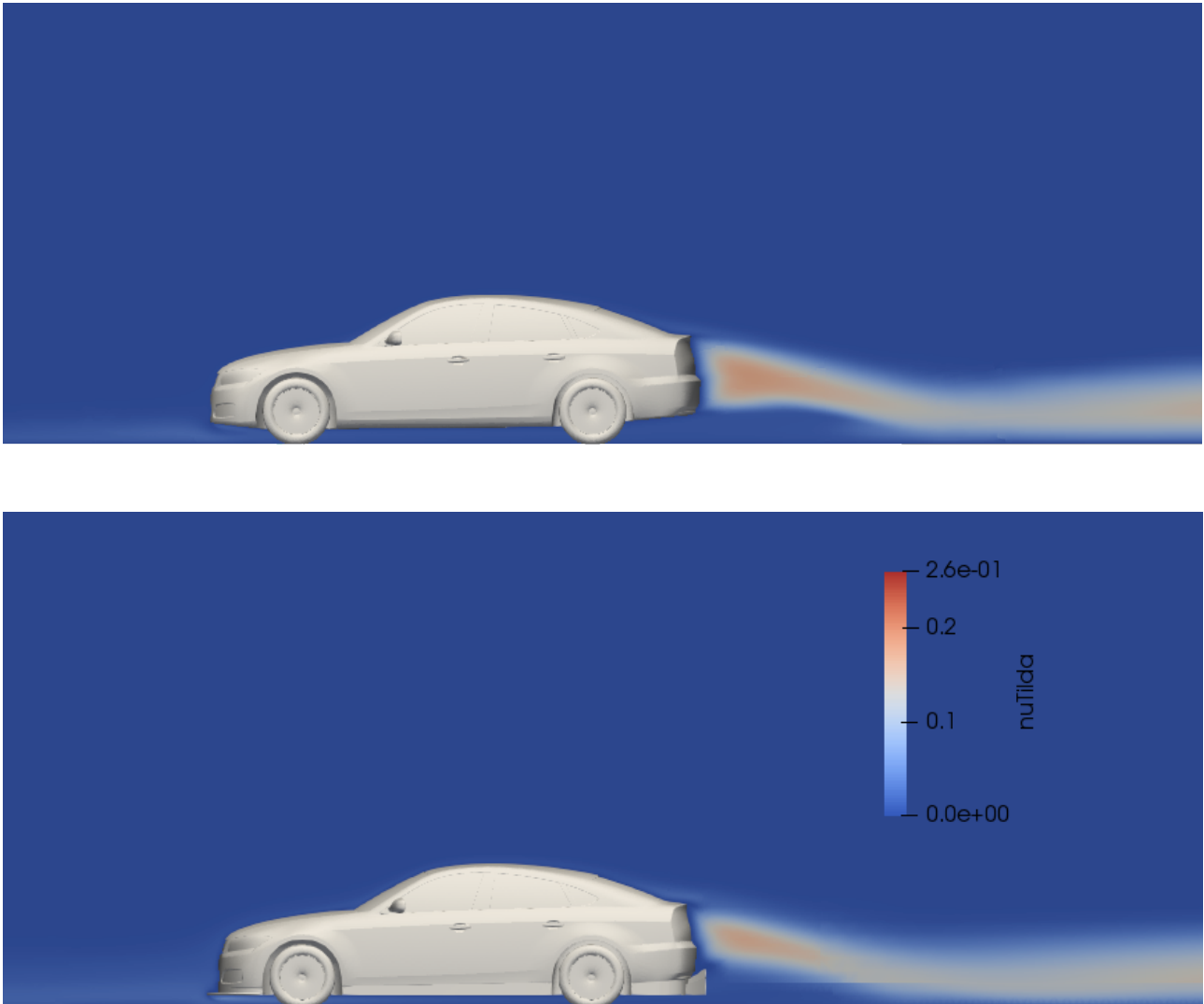
Figure 4.10: The variable $\tilde{v}$ field for the original geometry (top) and for the geometry with the LM GTE modifications (bottom) at their symmetry plane. The colour scale is the same for the two fields and the units are m^2/s.

The variable $\tilde{v}$ is again mostly zero, apart from the wake of the vehicle. The two fields are very similar, apart from the area directly behind the vehicle, where the variable $\tilde{v}$ is slightly larger for the original geometry.

5. The Adjoint Flow Problem

5.1. The Optimization Cycle

In gradient-based optimization methods, numerous candidate optimal solutions are simulated sequentially. After the initial solution, which is directly or indirectly set by the user, a next candidate solution has to be reached. This is done by computing the direction in which the objective function is reduced (for minimization problems) or increased (for maximization problems). The quantities that indicate this direction are the sensitivity derivatives, which are the derivatives of the objective function with respect to the design variables.

In the adjoint method, the sensitivity derivatives are computed after solving the adjoint flow field. This field is computed by solving the adjoint field equations and their boundary conditions. These equations are relatively similar to the Navier—Stokes Equations and their boundary conditions.

The solution of the adjoint flow field requires full knowledge of the primal flow field, which is the solution of the Navier—Stokes equations. Consequently, in the adjoint-assisted optimization algorithm, the adjoint flow equations must be solved and also the Navier—Stokes equations at each cycle and their solution must be stored until the cycle is complete.

One of the advantages of the adjoint method, is that the computational cost is independent of the number of design variables. In contrast to other methods of computing sensitivity derivatives, such as direct differentiation, where the computational cost is directly proportional to the number of the design variables, the adjoint method is a valuable tool for shape optimization problems with complex geometries, as is the optimization of a car surface. The optimization costs of the adjoint method, on the other hand, are proportional to the number of objective functions. As a result, this optimization tool may not be the most suitable solution for all optimization problems. The engineer is called to evaluate and decide on the optimization tools according to each problem characteristics.

It has to be noted that the design variables are not always the variables of the CAD software that describe the model geometry. If the CAD software cannot be incorporated into the optimization cycle for automatic generation of the next solution, the geometry is described by an analytical, parametrically described geometry type, such as spline or Bézier surfaces. The design variables then become the parameters that describe the analytical geometry. After the termination of the optimization, the geometry may then be reconstructed in the CAD software. It is noted that not only the model geometry is parameterized, but also every CFD point in the parameterized space. This means that, in every geometry deformation, there is usually no need for remeshing and that the cells keep their previous flow quantities' values as the next initialization.

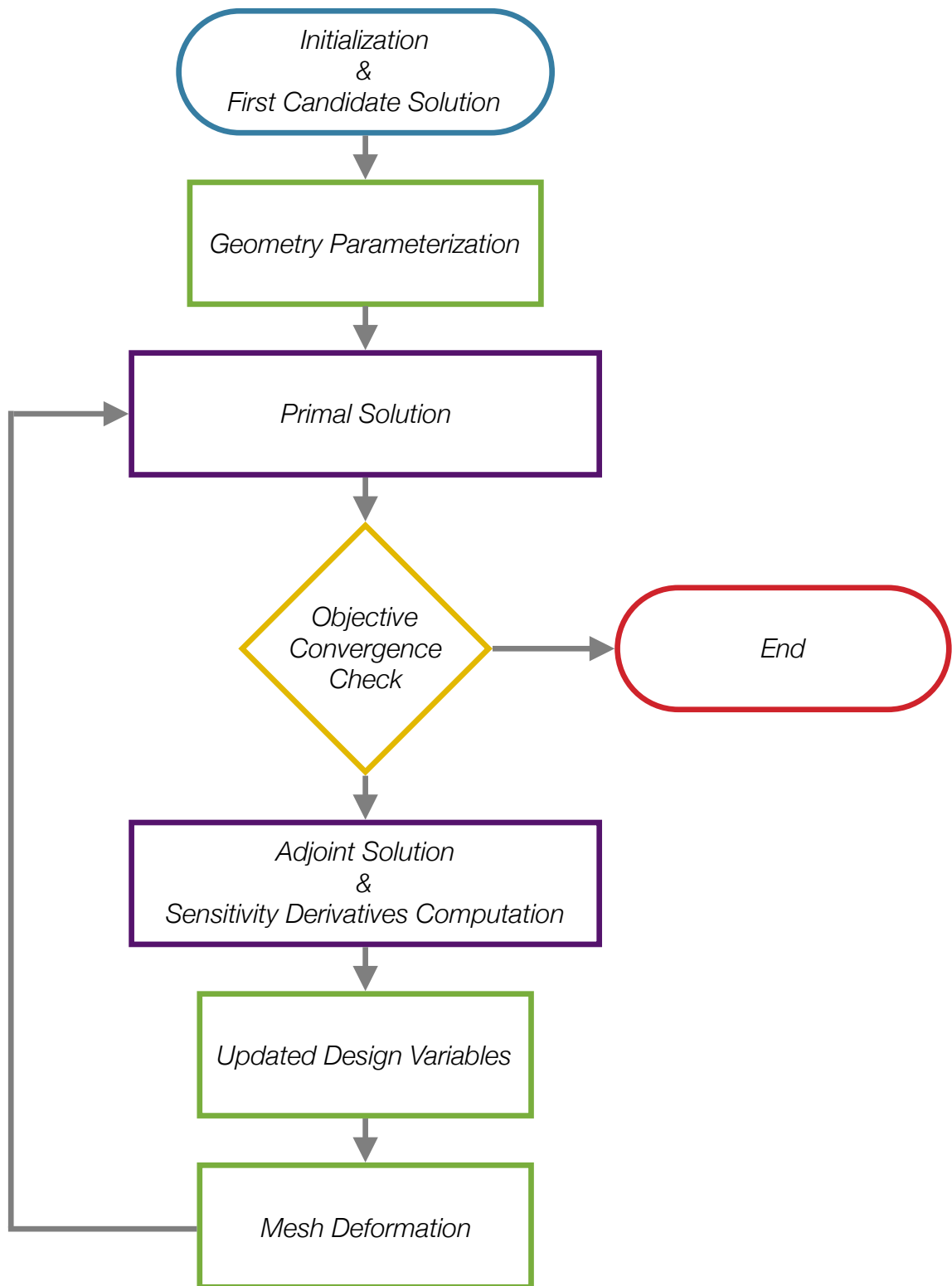The optimization algorithm is depicted in figure 5.1.[39]

Figure 5.1: The optimization algorithm using the adjoint method with a free form deformation method. Purple boxes indicate processes with high computational cost.

5.2. Continuous Adjoint

5.2.1. Introduction To Continuous Adjoint

With the continuous adjoint method the adjoint flow equations and the adjoint boundary conditions are derived, solved and then, the sensitivity derivatives of the objective function are computed.

In this analysis, the hypothesis of "frozen turbulence" is not made and the adjoint equations to the Spalart—Allmaras model are also solved.

Let F be the objective function and b_n the design variables, where $n = 1, 2, ..., N_p$. The results of the primal problem, the pressure distribution p and the velocity distribution u are stored in a vector U. Naturally, the pressure and velocity distribution and, consequently, vector U, are dependent on the model geometry, which is described by the design variables, stored in vector b. So, symbolically:

5.1.
$$\vec{U} = \vec{U}(\vec{b})$$

The value of the objective function is dependent on the design variables, but also dependent on the pressure and velocity distribution U. Symbolically:

5.2.
$$F = F\left(\vec{b}, \vec{U}(\vec{b})\right)$$

taking into account the dependence of F and U from the grid coordinates x as well, equation *(5.II)* extends to:

5.3.
$$F = F\left(\vec{b}, \vec{x}(b), \vec{U}(\vec{x}(b), \vec{b})\right)$$

Let v be the adjoint velocity, q the adjoint pressure and $\tilde{v}_a$ the adjoint variable $\tilde{v}$.

The augmented objective function is defined, by adding to the objective function two volume integrals of the product of the adjoint velocity and the residual $R^u{}_i$ and the adjoint pressure and the residual R^p, respectively:

5.4.
$$F_{aug} = F + \oiiint_\Omega v_i R^u{}_i \, d\Omega + \oiiint_\Omega q R^p \, d\Omega + \oiiint_\Omega \tilde{v}_a R^{\tilde{v}} \, d\Omega$$

where Ω is the computational domain.

It is noted that since equations *(4.3)* and *(4.4)* are true, $F_{aug} \equiv F$.

Using the Lebniz theorem, by differentiating with b_n, equation *(5.4)* becomes:

$$\frac{\delta F_{aug}}{\delta b_n} = \frac{\delta F}{\delta b_n} + \frac{\delta}{\delta b_n} \oiiint_\Omega v_i R^u{}_i \, d\Omega + \frac{\delta}{\delta b_n} \oiiint_\Omega q R^p \, d\Omega + \frac{\delta}{\delta b_n} \oiiint_\Omega \tilde{v}_a R^{\tilde{v}} \, d\Omega \Rightarrow$$

5.5. $$\frac{\delta F_{aug}}{\delta b_n} = \frac{\delta F}{\delta b_n} + \oiiint_\Omega v_i \frac{\partial R^u{}_i}{\partial b_n} d\Omega + \oiiint_\Omega q \frac{\partial R^p}{\partial b_n} d\Omega + \oiiint_\Omega \tilde{v}_a \frac{\partial R^{\tilde{v}}}{\partial b_n} d\Omega + \oiint_S \left(v_i R^u{}_i + q R^p + \tilde{v}_a R^{\tilde{v}}\right) n_k \frac{\delta x_k}{\delta b_n} dS$$

where:

- **n**: A vector containing all the vertical vectors to the surface S,

- x_k: Points describing the surface S,

- S is the boundary of the computational domain. This boundary can be divided into the following boundary surfaces:

  - S_I: The inlet surface,

  - S_O: The outlet surface,

  - S_E: The side and top surfaces,

  - S_S: The symmetry plane,

  - S_R: The road,

  - S_{Mb}: The surface of the vehicle model.

  It is true that $S = S_I \cup S_O \cup S_E \cup S_S \cup S_R \cup S_{Mb}$.

In addition, the S_{Mb} is the only surface dependent by the design variables, hence the index b, while the geometry of the rest surfaces if fixed and independent of the design variables b_n, which means that the x_k derivatives with respect to b_n is zero in $S \setminus S_{Mb}$. Consequently, equation *(5.V)* can be written as:

5.6. $$\frac{\delta F_{aug}}{\delta b_n} = \frac{\delta F}{\delta b_n} + \iiint_{\mho} v_i \frac{\partial R^u_{\ i}}{\partial b_n} d\mho + \iiint_{\mho} q \frac{\partial R^p}{\partial b_n} d\mho + \iiint_{\mho} \tilde{v}_a \frac{\partial R^{\tilde{v}}}{\partial b_n} d\mho + \oiint_{S_{M_b}} \left(v_i R^u_{\ i} + q R^p + \tilde{v}_a R^{\tilde{v}} \right) n_k \frac{\delta x_k}{\delta b_n} dS$$

It is also noted that for any quantity Q, the notation $\delta Q / \delta b_n$ means the total variation in Q, due to a variation in b_n. Additionally, the notation $\partial Q / \partial b_n$ the variation in Q caused due to changes in the flow variables, not including direct contributions due to geometry alterations caused by b_n variations. The following is true:[40]

5.7. $$\frac{\delta Q}{\delta b_n} = \frac{\partial Q}{\partial b_n} + \frac{\partial Q}{\partial x_k} \frac{\delta x_k}{\delta b_n}$$

If the quantity Q is computed on a surface, the following is true:

5.8. $$\frac{\delta Q}{\delta b_n} = \frac{\partial Q}{\partial b_n} + \frac{\partial Q}{\partial x_k} n_k \frac{\delta x_m}{\delta b_n} n_m$$

5.2.2. The Objective Function & Its Differentiation

In cases such as the present, where the objective function, such as the downforce, is a surface integrated quantity, the following expression is valid:

5.9.
$$F = \oiint_S F_S \, dS = \oiint_S F_{S_i} n_i \, dS$$

By differentiating the above equation:

5.10.
$$\frac{\delta F}{\delta b_n} = \frac{\delta}{\delta b_n} \oiint_S F_{S_i} n_i \, dS$$

The differential of the surface integral in equation *(5.10)* can be developed as:

5.11.
$$\frac{\delta}{\delta b_n} \oiint_S F_{S_i} n_i \, ds = \oiint_{S_{M_b}} \frac{\delta F_{S_i}}{\delta b_n} n_i \, dS + \oiint_{S_{M_b}} F_{S_i} \frac{\delta n_i}{\delta b_n} \, dS + \oiint_{S_{M_b}} F_{S_i} n_i \frac{\delta dS}{\delta b_n}$$

By taking into account equation *(5.8)*, equation *(5.11)* becomes:

5.12.
$$\frac{\delta}{\delta b_n} \oiint_S F_{S_i} n_i \, dS = \oiint_{S_{M_b}} \frac{\partial F_{S_i}}{\partial b_n} n_i \, dS + \oiint_{S_{M_b}} n_i \frac{\partial F_{S_i}}{\partial x_m} n_m \frac{\delta x_k}{\delta b_n} n_k \, dS + \oiint_{S_{M_b}} F_{S_i} \frac{\delta n_i}{\delta b_n} \, dS + \oiint_{S_{M_b}} F_{S_i} n_i \frac{\delta(dS)}{\delta b_n}$$

By implementing the chain rule, the partial derivative of *F* is:

5.13.
$$\frac{\partial F_{S_i}}{\partial b_n} = \frac{\partial F_{S_i}}{\partial u_k} \frac{\partial u_k}{\partial b_n} + \frac{\partial F_{S_i}}{\partial p} \frac{\partial p}{\partial b_n} + \frac{\partial F_{S_i}}{\partial \tau_{kj}} \frac{\partial \tau_{kj}}{\partial b_n}$$

where τ_{kj} is the stress tensor.

After substitution, the resultant equation is:

5.14.
$$\frac{\delta}{\delta b_n} \oiint_S F_{S_i} n_i \, dS = \oiint_{S_{M_b}} \frac{\partial F_{S_i}}{\partial u_k} n_i \frac{\partial u_k}{\partial b_n} \, dS + \oiint_{S_{M_b}} \frac{\partial F_{S_i}}{\partial p} n_i \frac{\partial p}{\partial b_n} \, dS + \oiint_{S_{M_b}} \frac{\partial F_{S_i}}{\partial \tau_{kj}} n_i \frac{\partial \tau_{kj}}{\partial b_n} \, dS$$
$$+ \oiint_{S_{M_b}} n_i \frac{\partial F_{S_i}}{\partial x_m} n_m \frac{\delta x_k}{\delta b_n} n_k \, dS + \oiint_{S_{M_b}} F_{S_i} \frac{\delta n_i}{\delta b_n} \, dS + \oiint_{S_{M_b}} F_{S_i} n_i \frac{\delta(dS)}{\delta b_n}$$

The derivatives of the geometrical quantities are developed using the following identities from differential geometry:[41]

5.15.
$$\frac{\delta n_i}{\delta b_n} = -\frac{\partial_\tau}{\partial x_i} \left(\frac{\delta x_k}{\delta b_n} n_k \right)$$

5.16.
$$\frac{\delta(dS)}{\delta b_n} = -\kappa \frac{\delta x_\kappa}{\delta b_n} n_k \, dS$$

where:

- $\partial_\tau/\partial x_i$: The tangental derivative,

- κ: The mean curvature of the surface.

After substitution:

5.17.
$$\frac{\delta}{\delta b_n} \iint_S F_{S_i} n_i \, dS = \iint_{S_{M_b}} \frac{\partial F_{S_i}}{\partial u_k} n_i \frac{\partial u_k}{\partial b_n} \, dS + \iint_{S_{M_b}} \frac{\partial F_{S_i}}{\partial p} n_i \frac{\partial p}{\partial b_n} \, dS + \iint_{S_{M_b}} \frac{\partial F_{S_i}}{\partial \tau_{kj}} n_i \frac{\partial \tau_{kj}}{\partial b_n} \, dS$$

$$+ \iint_{S_{M_b}} n_i \frac{\partial F_{S_i}}{\partial x_m} n_m \frac{\delta x_k}{\delta b_n} n_k \, dS - \iint_{S_{M_b}} F_{S_i} \frac{\partial_\tau}{\partial x_i} \left(\frac{\delta x_k}{\delta b_n} n_k \right) dS - \iint_{S_{M_b}} F_{S_i} n_i \kappa \frac{\delta x_\kappa}{\delta b_n} n_k \, dS$$

Substituting in equation *(5.10)*, the final expression of *δF/δb$_n$* becomes:

5.18.
$$\frac{\delta F}{\delta b_n} = \iint_{S_{M_b}} \frac{\partial F_{S_i}}{\partial u_k} n_i \frac{\partial u_k}{\partial b_n} \, dS + \iint_{S_{M_b}} \frac{\partial F_{S_i}}{\partial p} n_i \frac{\partial p}{\partial b_n} \, dS + \iint_{S_{M_b}} \frac{\partial F_{S_i}}{\partial \tau_{kj}} n_i \frac{\partial \tau_{kj}}{\partial b_n} \, dS$$

$$+ \iint_{S_{M_b}} n_i \frac{\partial F_{S_i}}{\partial x_m} n_m \frac{\delta x_k}{\delta b_n} n_k \, dS - \iint_{S_{M_b}} F_{S_i} \frac{\partial_\tau}{\partial x_i} \left(\frac{\delta x_k}{\delta b_n} n_k \right) dS - \iint_{S_{M_b}} F_{S_i} n_i \kappa \frac{\delta x_\kappa}{\delta b_n} n_k \, dS$$

5.2.3. The Adjoint Field Equations

5.2.3.A. Adjoint Mean Flow Equations

In equation *(5.6)*, the partial derivatives of the Navier—Stokes equations with respect to the design variables b_n are included. These can be developed by differentiating the Navier—Stokes equations with respect to the design variables b_n. It is noted that, due to the nature of the $\partial/\partial b_n$ and the $\delta/\delta b_n$ operators applied to a quantity Q, the following statements are generally true:

5.19.
$$\frac{\partial}{\partial b_n}\left(\frac{\partial Q}{\partial x_j}\right) = \frac{\partial}{\partial x_j}\left(\frac{\partial Q}{\partial b_n}\right)$$

$$\frac{\delta}{\delta b_n}\left(\frac{\partial Q}{\partial x_j}\right) \neq \frac{\partial}{\partial x_j}\left(\frac{\delta Q}{\delta b_n}\right)$$

The resultant differentiated equations are:

5.20.
$$\frac{\partial R^p}{\partial b_n} = -\frac{\partial}{\partial x_j}\left(\frac{\partial u_j}{\partial b_n}\right)$$

5.21.
$$\frac{\partial R^u_j}{\partial b_n} = \frac{\partial u_j}{\partial b_n}\frac{\partial u_i}{\partial x_j} + u_j\frac{\partial}{\partial x_j}\left(\frac{\partial u_i}{\partial b_n}\right) + \frac{\partial}{\partial x_j}\left(\frac{\partial p}{\partial b_n}\right) - \frac{\partial}{\partial x_j}\left[(\nu+\nu_t)\frac{\partial}{\partial b_n}\left(\frac{\partial u_i}{\partial x_j}+\frac{\partial u_j}{\partial x_i}\right)\right] - \frac{\partial}{\partial x_j}\left[\frac{\partial \nu_t}{\partial b_n}\left(\frac{\partial u_i}{\partial x_j}+\frac{\partial u_j}{\partial x_i}\right)\right]$$

5.22.
$$\frac{\partial R^{\tilde{\nu}}}{\partial b_n} = \frac{\partial \tilde{\nu}}{\partial x_j}\frac{\partial u_j}{\partial b_n} + u_j\frac{\partial}{\partial x_j}\left(\frac{\partial \tilde{\nu}}{\partial b_n}\right) - \frac{\partial}{\partial x_j}\left[\left(\nu+\frac{\tilde{\nu}}{\sigma}\right)\frac{\partial}{\partial x_j}\left(\frac{\partial \tilde{\nu}}{\partial b_n}\right)\right] - \frac{1}{\sigma}\frac{\partial}{\partial x_j}\left(\frac{\partial \tilde{\nu}}{\partial b_n}\frac{\partial \tilde{\nu}}{\partial x_j}\right) - 2\frac{C_{b_2}}{\sigma}\frac{\partial \tilde{\nu}}{\partial x_j}\frac{\partial}{\partial x_j}\left(\frac{\partial \tilde{\nu}}{\partial b_n}\right) + \tilde{\nu}\left(-\frac{\partial P}{\partial b_n}+\frac{\partial D}{\partial b_n}\right) + (-P+D)\frac{\partial \tilde{\nu}}{\partial b_n}$$

The differentiation of production and dissipation terms yield:[42]

5.23.
$$-\frac{\partial P}{\partial b_n}+\frac{\partial D}{\partial b_n} = C_{\tilde{\nu}}\frac{\partial \tilde{\nu}}{\partial b_n} + C_d\frac{\partial d}{\partial b_n} + C_Y\frac{1}{Y}e_{mjk}\frac{\partial u_k}{\partial x_j}e_{mli}\frac{\partial}{\partial x_l}\left(\frac{\partial u_i}{\partial b_n}\right)$$

where:

5.24.
$$C_{\tilde{\nu}} = \left(-C_{b_1}-C_{w_1}C\frac{r}{\tilde{Y}}\right)\left(\frac{\partial f_{u_3}}{\partial \tilde{\nu}}Y + \frac{f_{u_2}}{\kappa^2 d^2} + \frac{\partial f_{u_2}}{\partial \tilde{\nu}}\frac{\tilde{\nu}}{\kappa^2 d^2}\right) + C_{w_1}C\frac{r}{\tilde{Y}} + C_{w_1}\frac{f_w}{d^2}$$

5.25.
$$C_d = -\frac{2}{d^3}\left[c_{w_1}rC\left(d^2-\frac{\tilde{\nu}f_{u_2}}{\kappa^2\tilde{Y}}\right) + C_{w_1}f_w\tilde{\nu} - C_{b_1}\frac{f_{u_2}}{\kappa^2}\tilde{\nu}\right]$$

5.26.
$$C_Y = \left(-C_{b1}-C_{w1}C\frac{r}{\tilde{Y}}\right)f_{u_3}$$

5.27.
$$C = \frac{c_{w_1}\tilde{\nu}^2}{d^2}\left[1+c_{w2}\left(6r^5-1\right)\right]\frac{c_{w_3}^{\,6}}{g^6+c_{w_3}^{\,6}}\left(\frac{1+c_{w_3}^{\,6}}{g^6+c_{w_3}^{\,6}}\right)^{\frac{1}{6}}$$

$$5.28. \qquad \frac{\partial f_{u_2}}{\partial \tilde{v}} = -\frac{3}{\nu C_{u_2}}\left(1+\frac{X}{C_{u_2}}\right)^{-4}$$

$$5.29. \qquad \frac{\partial f_{u_3}}{\partial \tilde{v}} = \frac{1}{C_{u_2}}\left(\frac{f_{u_1}}{\nu}+X\frac{\partial f_{u_1}}{\partial \nu}\right)\left[3\left(1+\frac{X}{C_{u_2}}\right)+\left(\frac{X}{C_{u_2}}\right)^2\right]\left(1+\frac{X}{C_{u_2}}\right)^{-3}$$

$$+\frac{1}{\nu C_{u_2}{}^2}\left(1+Xf_{u1}\right)\left(3+2\frac{X}{C_{u_2}}\right)C_{u_2}{}^2\left(1+\frac{X}{C_{u_2}}\right)^{-3}$$

$$-3\frac{\left(1+Xf_{u1}\right)}{\nu C_{u_2}{}^2}\left[3\left(1+\frac{X}{C_{u_2}}\right)+\left(\frac{X}{C_{u_2}}\right)^2\right]\left(1+\frac{X}{C_{u_2}}\right)^{-4}$$

Using the Green–Gauss theorem and by substituting equation *(5.10)*, the volume integral $\oiiint_{\mho} q\frac{\partial R^p}{\partial b_n}d\mho$ in equation *(5.6)* is developed as:

$$5.30. \qquad \oiiint_{\mho} -q\frac{\partial}{\partial x_j}\left(\frac{\partial u_j}{\partial b_n}\right)d\mho = \oiiint_{\mho} q\frac{\partial q}{\partial x_j}\frac{\partial u_j}{\partial b_n}d\mho - \oiint_{S} q\frac{\partial u_j}{\partial b_n}n_j dS$$

Similarly, concerning the volume integral $\oiiint_{\mho} v_i\frac{\partial R^u{}_i}{\partial b_n}d\mho$ in equation *(5.6)*, the inviscid terms are developed as:

$$5.31. \quad \oiiint_{\mho} v_i\frac{\partial u_j}{\partial b_n}\frac{\partial u_i}{\partial x_j}d\mho + \oiiint_{\mho} v_i u_j\frac{\partial}{\partial x_j}\left(\frac{\partial u_i}{\partial b_n}\right)d\mho = \oiiint_{\mho} v_i\frac{\partial u_j}{\partial b_n}\frac{\partial u_i}{\partial x_j}d\mho + \oiint_{S} v_i u_j n_j\frac{\partial u_j}{\partial b_n}dS + \oiiint_{\mho}\frac{\partial}{\partial x_j}\left(v_i u_j\right)\frac{\partial u_i}{\partial b_n}d\mho$$

and:

$$5.32. \qquad \oiiint_{\mho} v_i\frac{\partial}{\partial x_i}\left(\frac{\partial p}{\partial b_n}\right)d\mho = -\oiiint_{\mho}\frac{\partial v_i}{\partial x_i}\frac{\partial p}{\partial b_n}d\mho + \oiint_{S} v_i n_i\frac{\partial p}{\partial b_n}dS$$

The viscous terms are developed as:

$$-\oiiint_{\mho} v_i\frac{\partial}{\partial x_j}\left[\left(\nu+\nu_t\right)\frac{\partial}{\partial b_n}\left(\frac{\partial u_i}{\partial x_j}+\frac{\partial u_j}{\partial x_i}\right)\right]d\mho = \oiiint_{\mho}\left(\nu+\nu_t\right)\frac{\partial v_i}{\partial x_j}\frac{\partial}{\partial b_n}\left(\frac{\partial u_i}{\partial x_j}+\frac{\partial u_j}{\partial x_i}\right)d\mho - \oiint_{S} v_i\left(\nu+\nu_t\right)\frac{\partial}{\partial b_n}\left(\frac{\partial u_i}{\partial x_j}+\frac{\partial u_j}{\partial x_i}\right)n_j dS \Rightarrow$$

$$5.33. -\oiiint_{\mho} v_i\frac{\partial}{\partial x_j}\left[\left(\nu+\nu_t\right)\frac{\partial}{\partial b_n}\left(\frac{\partial u_i}{\partial x_j}+\frac{\partial u_j}{\partial x_i}\right)\right]d\mho = \oiiint_{\mho}\left(\nu+\nu_t\right)\frac{\partial v_i}{\partial x_j}\frac{\partial}{\partial x_j}\left(\frac{\partial u_i}{\partial b_n}\right)d\mho + \oiiint_{\mho}\left(\nu+\nu_t\right)\frac{\partial v_i}{\partial x_j}\frac{\partial}{\partial x_i}\left(\frac{\partial u_j}{\partial b_n}\right)d\mho$$

$$-\oiint_{S} v_i\left(\nu+\nu_t\right)\frac{\partial}{\partial b_n}\left(\frac{\partial u_i}{\partial x_j}+\frac{\partial u_j}{\partial x_i}\right)n_j dS$$

The two resultant volume integrals can further be developed as:

5.34.
$$\oiiint_\mho (v+v_t)\frac{\partial v_i}{\partial x_j}\frac{\partial}{\partial x_j}\left(\frac{\partial u_i}{\partial b_n}\right)d\mho = -\oiiint_\mho \frac{\partial}{\partial x_j}\left((v+v_t)\frac{\partial v_i}{\partial x_j}\right)\frac{\partial u_i}{\partial b_n}d\mho + \oiint_S (v+v_t)\frac{\partial v_i}{\partial x_j}n_j\frac{\partial u_i}{\partial b_n}dS$$

and:

$$\oiiint_\mho (v+v_t)\frac{\partial v_i}{\partial x_j}\frac{\partial}{\partial x_i}\left(\frac{\partial u_j}{\partial b_n}\right)d\mho = -\oiiint_\mho \frac{\partial}{\partial x_i}\left((v+v_t)\frac{\partial v_i}{\partial x_j}\right)\frac{\partial u_j}{\partial b_n}d\mho + \oiint_S (v+v_t)\frac{\partial v_i}{\partial x_j}n_i\frac{\partial u_j}{\partial b_n}dS \Rightarrow$$

5.35.
$$\oiiint_\mho (v+v_t)\frac{\partial v_i}{\partial x_j}\frac{\partial}{\partial x_i}\left(\frac{\partial u_j}{\partial b_n}\right)d\mho = -\oiiint_\mho \frac{\partial}{\partial x_i}\left((v+v_t)\frac{\partial v_j}{\partial x_i}\right)\frac{\partial u_i}{\partial b_n}d\mho + \oiint_S (v+v_t)\frac{\partial v_j}{\partial x_i}n_j\frac{\partial u_i}{\partial b_n}dS$$

Similarly for the terms concerning the adjoint variable $\tilde{v}$, using the Green—Gauss theorem and by substituting equation *(5.10)*, the first volume integral is developed as:

The final term in equation *(5.21)* is developed as:

5.36.
$$-\oiiint_\mho v_i\frac{\partial}{\partial x_j}\left[\frac{\partial v_t}{\partial x_j}\left(\frac{\partial u_i}{\partial x_j}+\frac{\partial u_j}{\partial x_i}\right)\right]d\mho = +\oiiint_\mho v_i\left(\frac{\partial u_i}{\partial x_j}+\frac{\partial u_j}{\partial x_i}\right)n_j\frac{\partial v_t}{\partial \tilde{v}}\frac{\partial \tilde{v}}{\partial b_n}d\mho - \oiint_S \frac{\partial v_i}{\partial x_j}\left(\frac{\partial u_i}{\partial x_j}+\frac{\partial u_j}{\partial x_i}\right)\frac{\partial v_t}{\partial \tilde{v}}\frac{\partial \tilde{v}}{\partial b_n}dS$$

where $\partial v_t/\partial \tilde{v}$ is given by:

5.37.
$$\frac{\partial v_t}{\partial \tilde{v}} = f_{u_1} + \tilde{v}\frac{\partial f_{u_1}}{\partial \tilde{v}} = f_{u_1} + \frac{3C_{u_1}{}^3 X^2}{\left(X^3+C_{u_1}{}^3\right)^2}$$

Similarly for the terms concerning the adjoint variable $\tilde{v}$, using the Green—Gauss theorem and by substituting equation *(5.10)*, a term by term analysis follows:

5.38.
$$\oiiint_\mho \tilde{v}_a\frac{\partial \tilde{v}}{\partial x_j}\frac{\partial u_j}{\partial b_n}d\mho + \oiiint_\mho \tilde{v}_a u_j\frac{\partial}{\partial x_j}\left(\frac{\partial \tilde{v}}{\partial b_n}\right)d\mho = \oiiint_\mho \tilde{v}_a\frac{\partial \tilde{v}}{\partial x_j}\frac{\partial u_j}{\partial b_n}d\mho - \oiiint_\mho \frac{\partial\left(\tilde{v}_a u_j\right)}{\partial x_j}\left(\frac{\partial \tilde{v}}{\partial b_n}\right)d\mho + \oiiint_S \tilde{v}_a u_j n_j\frac{\partial \tilde{v}}{\partial b_n}dS$$

and:

5.39.
$$-\oiiint_\mho \tilde{v}_a\frac{\partial}{\partial x_j}\left[\left(v+\frac{\tilde{v}}{\sigma}\right)\frac{\partial}{\partial x_j}\left(\frac{\partial \tilde{v}}{\partial b_n}\right)\right]d\mho = \oiiint_\mho \frac{\partial}{\partial x_j}\left[\left(v+\frac{\tilde{v}}{\sigma}\right)\frac{\partial \tilde{v}_a}{\partial x_j}\right]\frac{\partial \tilde{v}}{\partial b_n}d\mho + \oiiint_S \frac{\partial \tilde{v}_a}{\partial x_j}n_j\left(v+\frac{\tilde{v}}{\sigma}\right)\frac{\partial \tilde{v}}{\partial b_n}dS - \oiiint_S \tilde{v}_a n_j\left(v+\frac{\tilde{v}}{\sigma}\right)\frac{\partial}{\partial x_j}\left(\frac{\partial \tilde{v}}{\partial b_n}\right)dS$$

and:

5.40.
$$-\oiiint_\mho \tilde{v}_a\frac{1}{\sigma}\frac{\partial}{\partial x_j}\left(\frac{\partial \tilde{v}}{\partial b_n}\frac{\partial \tilde{v}}{\partial x_j}\right)d\mho = \oiiint_\mho \frac{1}{\sigma}\frac{\partial \tilde{v}_a}{\partial x_j}\frac{\partial \tilde{v}}{\partial b_n}\frac{\partial \tilde{v}}{\partial x_j}d\mho - \oiiint_S \tilde{v}_a\frac{1}{\sigma}\frac{\partial \tilde{v}}{\partial x_j}n_j\frac{\partial \tilde{v}}{\partial b_n}dS$$

and:

5.41.
$$-\oiiint_\mho 2\tilde{v}_a\frac{C_{b_2}}{\sigma}\frac{\partial \tilde{v}}{\partial x_j}\frac{\partial}{\partial x_j}\left(\frac{\partial \tilde{v}}{\partial b_n}\right)d\mho = \oiiint_\mho 2\frac{C_{b_2}}{\sigma}\frac{\partial}{\partial x_j}\left(\tilde{v}_a\frac{\partial \tilde{v}}{\partial x_j}\right)\frac{\partial \tilde{v}}{\partial b_n}d\mho - \oiiint_S 2\tilde{v}_a\frac{C_{b_2}}{\sigma}\frac{\partial \tilde{v}}{\partial x_j}n_j\frac{\partial \tilde{v}}{\partial b_n}dS$$

and, finally:

$$5.42. \quad \iiint_\Im \tilde{v}_a \tilde{v} \left(-\frac{\partial P}{\partial b_n} + \frac{\partial D}{\partial b_n} \right) d\Im = \iiint_\Im \tilde{v}_a \tilde{v} C_{\tilde{v}} \frac{\partial \tilde{v}}{\partial b_n} d\Im + \iiint_\Im \tilde{v}_a \tilde{v} C_d \frac{\partial d}{\partial b_n} d\Im - \iiint_\Im \frac{\partial}{\partial x_l} \left(\tilde{v}_a \tilde{v} C_Y \frac{1}{Y} e_{mjk} \frac{\partial u_k}{\partial x_j} e_{mli} \right) \frac{\partial u_i}{\partial b_n} d\Im + \iint_S \tilde{v}_a \tilde{v} C_Y \frac{1}{Y} e_{mjk} \frac{\partial u_k}{\partial x_j} e_{mli} n_l \frac{\partial u_i}{\partial b_n} dS$$

By substituting equations *(5.30)* to *(5.36)* and *(5.38)* to *(5.42)* into equation *(5.6)*, and utilizing equation *(5.18)* the following expression of the augmented objective function is formed.

$$5.43. \quad \frac{\delta F_{aug}}{\delta b_n} = \iint_S \left[v_i u_j n_j + (v + v_t) \left(\frac{\partial v_i}{\partial x_j} + \frac{\partial v_j}{\partial x_i} \right) n_j - q n_i + \tilde{v}_a \tilde{v} C_Y \frac{1}{Y} e_{mjk} \frac{\partial u_k}{\partial x_j} e_{mli} n_l + \frac{\partial F_{S_k}}{\partial u_i} n_k \right] \frac{\partial u_i}{\partial b_n} dS$$

$$+ \iint_S \left[v_j n_j + \frac{\partial F_{S_i}}{\partial p} n_i \right] \frac{\partial p}{\partial b_n} dS$$

$$+ \iint_S \left[\tilde{v}_a u_j n_j + \left(v + \frac{\tilde{v}}{\sigma} \right) \frac{\partial \tilde{v}_a}{\partial x_j} n_j - \frac{\tilde{v}_a}{\sigma} (1 + 2C_{b_2}) \frac{\partial \tilde{v}}{\partial x_j} n_j + \frac{\partial F_{S_k}}{\partial \tilde{v}} n_i \right] \frac{\partial \tilde{v}}{\partial b_n} dS$$

$$+ \iint_S \left[-v_i n_j + \frac{\partial F_{S_i}}{\partial \overleftrightarrow{\tau}_{ij}} n_k \right] \frac{\partial \tau_{ij}}{\partial b_n} dS - \iint_S \tilde{v}_a \left(v + \frac{\tilde{v}}{\sigma} \right) \frac{\partial}{\partial b_n} \left(\frac{\partial \tilde{v}}{\partial x_j} \right) n_j dS$$

$$+ \iint_{S_{M_b}} n_i \frac{\partial F_{S_i}}{\partial x_m} n_m \frac{\delta x_k}{\delta b_n} n_k dS + \iint_{S_{M_b}} F_{S_i} \frac{\delta n_i}{\delta b_n} dS + \iint_{S_{M_b}} F_{S_i} n_i \frac{\delta(dS)}{\delta b_n}$$

$$+ \iint_{S_{M_b}} \left[v_i R^u_i + q R^p + \tilde{v}_a R^{\tilde{v}} \right] \frac{\delta x_k}{\delta b_n} n_k dS + \iiint_\Im \tilde{v} \tilde{v}_a C_d \frac{\partial d}{\partial b_n} d\Im$$

$$+ \iiint_\Im R^u_i \frac{\partial u_i}{\partial b_n} d\Im + \iiint_\Im R^q \frac{\partial p}{\partial b_n} d\Im + \iiint_\Im R^{\tilde{v}_a} \frac{\partial \tilde{v}}{\partial b_n} d\Im$$

In order to avoid computing the partial derivatives of **U**, the multipliers of $\partial u_i/\partial b_n$, $\partial p/\partial b_n$ and $\partial \tilde{v}/\partial b_n$ in the final two volume integrals are set to zero. This determines the adjoint mean flow equations, which are the following:[43]

$$5.44. \quad R^q = -\frac{\partial v_j}{\partial x_j} = 0$$

$$5.45. \quad R^v_i = v_j \frac{\partial u_j}{\partial x_i} - \frac{\partial(u_j v_i)}{\partial x_j} + \frac{\partial q}{\partial x_i} - \frac{\partial}{\partial x_j} \left((v + v_t) \left(\frac{\partial v_i}{\partial x_j} + \frac{\partial v_j}{\partial x_i} \right) \right) = 0$$

$$5.46. \quad R^{\tilde{v}_a} = -\frac{\partial(u_j \tilde{v}_a)}{\partial x_j} - \frac{\partial}{\partial x_j} \left[\left(v + \frac{\tilde{v}}{\sigma} \right) \frac{\partial \tilde{v}_a}{\partial x_j} \right] + \frac{1}{\sigma} \frac{\partial \tilde{v}_a}{\partial x_j} \frac{\partial \tilde{v}}{\partial x_j} + \frac{2C_{b_2}}{\sigma} \frac{\partial}{\partial x_j} \left(\tilde{v}_a \frac{\partial \tilde{v}}{\partial x_j} \right) + \tilde{v}_a \tilde{v} C_{\tilde{v}} + \frac{\partial v_t}{\partial \tilde{v}} \frac{\partial v_i}{\partial x_j} \left(\frac{\partial u_i}{\partial x_j} + \frac{\partial u_j}{\partial x_i} \right) + (-P + D) \tilde{v}_a = 0$$

Equation *(5.44)* is the adjoint continuity equation, equation *(5.45)* is the adjoint momentum equation and equation *(5.45)* is the adjoint turbulence model equation. Note the similarity between the adjoint mean flow equations and the primal mean flow equations, *(4.3)*, *(4.4)* and *(4.12)*. Also note that, in contrast to the primal momentum equation, the adjoint momentum equation is linear.

It should also be noted that equation 5.43 is the sensitivity expression of the SI approach.[44] In this Diploma Thesis, the E-SI method has been used, which introduces an extra adjoint variable and equation in order to avoid the computation of the $\partial x_k / \partial b_n$ terms. This is achieved by assuming a Laplacian model for the grid node displacements:

5.47.
$$R_i^m = \frac{\partial^2 m_i}{\partial x_j^{\,2}} = 0$$

where m_i: are the Cartesian displacements of the grid nodes.

By incorporating equation *(5.47)* into equation *(5.4)*, equation *(5.4)* becomes:

5.48.
$$F_{aug} = F + \oiiint_{\mho} v_i R^u_{\,i} \, d\mho + \oiiint_{\mho} q R^p \, d\mho + \oiiint_{\mho} \tilde{v}_a R^{\tilde{v}} \, d\mho + \oiiint_{\mho} m_i^a R_i^m \, d\mho$$

where m^a_i: are the adjoint Cartesian displacements of the grid nodes.

Similarly to the aforementioned developments, using the Leibniz theorem the new term is developed as:

5.49.
$$\frac{\delta}{\delta b_n} \oiiint_{\mho} m_i^a R_i^m \, d\mho = +\oiiint_{\mho} \frac{\partial^2 m_i^a}{\partial x_j^{\,2}} \frac{\delta x_i}{\delta b_n} \, d\mho + \oiint_{S} m_i^a R_i^m n_k \frac{\delta x_k}{\delta b_n} \, dS + \oiint_{S} m_i^a n_j \frac{\partial}{\partial x_j} \left(\frac{\delta x_i}{\delta b_n} \right) dS - \oiint_{S_w} \frac{\partial m_i^a}{\partial x_j} n_j \frac{\delta x_i}{\delta b_n} \, dS$$

Since the extra term added to the objective function includes only variations in grid coordinates with respect to b_n, the adjoint flow field equations and their boundary conditions are the same. The sensitivity derivatives expression is the same, with the addition of some new terms resulting from equation *(5.49)*. By zeroing the coefficient of $\partial x_k / \partial b_n$ in the field integrals, the adjoint equation for the m^a_i becomes:

5.50.
$$R_k^{m^a} = \frac{\partial^2 m_k^a}{\partial x_j^{\,2}} + \frac{\partial}{\partial x_j} \left(v_i u_j \frac{\partial u_i}{\partial x_k} + v_j \frac{\partial p}{\partial x_k} + \tau^a_{\,ij} \frac{\partial u_i}{\partial x_k} - v_j \frac{\partial \tau_{ij}}{\partial x_k} - q \frac{\partial u_j}{\partial x_k} \right) = 0$$

5.2.3.B. Adjoint Boundary Conditions

5.2.3.B.a. Resultant Equation

After satisfying the adjoint mean flow equations, equation *(5.43)* becomes:

$$
5.51. \quad \frac{\delta F_{aug}}{\delta b_n} = \oiint_S \left[v_i u_j n_j + \left(v + v_t\right)\left(\frac{\partial v_i}{\partial x_j} + \frac{\partial v_j}{\partial x_i}\right) n_j - q n_i + \tilde{v}_a \tilde{v} C_Y \frac{1}{Y} e_{mjk} \frac{\partial u_k}{\partial x_j} e_{mli} n_l + \frac{\partial F_{S_k}}{\partial u_i} n_k \right] \frac{\partial u_i}{\partial b_n} dS
$$

$$
+ \oiint_S \left[v_j n_j + \frac{\partial F_{S_i}}{\partial p} n_i \right] \frac{\partial p}{\partial b_n} dS
$$

$$
+ \oiint_S \left[\tilde{v}_a u_j n_j + \left(v + \frac{\tilde{v}}{\sigma}\right)\frac{\partial \tilde{v}_a}{\partial x_j} n_j - \frac{\tilde{v}_a}{\sigma}\left(1 + 2 C_{b_2}\right)\frac{\partial \tilde{v}}{\partial x_j} n_j + \frac{\partial F_{S_k}}{\partial \tilde{v}} n_i \right] \frac{\partial \tilde{v}}{\partial b_n} dS
$$

$$
+ \oiint_S \left[-v_i n_j + \frac{\partial F_{S_i}}{\partial \overleftrightarrow{\tau}_{ij}} n_k \right] \frac{\partial \tau_{ij}}{\partial b_n} dS - \oiint_S \tilde{v}_a \left(v + \frac{\tilde{v}}{\sigma}\right)\frac{\partial}{\partial b_n}\left(\frac{\partial \tilde{v}}{\partial x_j}\right) n_j \, dS
$$

$$
+ \oiint_{S_{M_b}} n_i \frac{\partial F_{S_i}}{\partial x_m} n_m \frac{\delta x_k}{\delta b_n} n_k \, dS + \oiint_{S_{M_b}} F_{S_i} \frac{\delta n_i}{\delta b_n} dS + \oiint_{S_{M_b}} F_{S_i} n_i \frac{\delta(dS)}{\delta b_n}
$$

$$
+ \oiint_{S_{M_b}} \left[v_i R^u_{\ i} + q R^p + \tilde{v}_a R^{\tilde{v}} \right] \frac{\delta x_k}{\delta b_n} n_k \, dS + \oiiint_\mho \tilde{v} \tilde{v}_a C_d \frac{\partial d}{\partial b_n} d\mho
$$

$$
+ \oiint_S m_i^a R_i^m n_k \frac{\delta x_k}{\delta b_n} dS + \oiint_S m_i^a n_j \frac{\partial}{\partial x_j}\left(\frac{\delta x_i}{\delta b_n}\right) dS - \oiint_{S_W} \frac{\partial m_i^a}{\partial x_j} n_j \frac{\delta x_i}{\delta b_n} dS
$$

Using equation *(5.51)* and the primal boundary conditions, the adjoint boundary conditions will be determined.

5.2.3.B.b. On The Boundaries Of The Computational Domain

5.2.3.B.b.I. Inlet

At the inlet of the computational domain, since S_I is fixed, $\delta x_k / \delta b_n = 0$ and from the primal boundary conditions, the following is true:

$$
5.52. \quad \frac{\delta u_i}{\delta b_n} = \frac{\partial u_i}{\partial b_n} = 0
$$

As a result, the first integral of equation *(5.51)* is zero. In order to set the remaining integrals equal to zero, the following boundary conditions are set:

$$
5.53. \quad v_{\langle n \rangle} = v_j n_j = -\frac{\partial F_{S_{I,i}}}{\partial p} n_i
$$

$$
5.54. \quad v^I_{\langle t \rangle} = \frac{\partial F_{S_{I,k}}}{\partial \overleftrightarrow{\tau}_{ij}} n_k t_i^I n_j + \frac{\partial F_{S_{I,k}}}{\partial \overleftrightarrow{\tau}_{ij}} n_k t_j^I n_i
$$

5.55.
$$v^{II}_{\langle t \rangle} = \frac{\partial F_{S_{I,k}}}{\partial \tau_{ij}} n_k t^{II}_i n_j + \frac{\partial F_{S_{I,k}}}{\partial \tau_{ij}} n_k t^{II}_j n_i$$

where:

- t^I_i, t^{II}_i: The components of the tangent to the surface unit vectors,
- $v^I_{\langle i \rangle}$, $v^{II}_{\langle i \rangle}$: The components of the adjoint velocity, parallel to the surface unit vectors t^I_i and t^{II}_i, respectively.

Since for the adjoint pressure no condition results from equation *(5.51)*, its boundary condition is set as a zero Neumann condition.

In order to make equation *(5.51)* independent of the term $\frac{\partial}{\partial b_n}\left(\frac{\partial \tilde{v}}{\partial b_n}\right)n_j$, a zero Dirichlet boundary condition is imposed on $\tilde{v}_a$:

5.56.
$$\tilde{v}_a = 0$$

In order to make equation *(5.51)* independent of the term $\frac{\partial}{\partial x_j}\left(\frac{\delta x_k}{\delta b_n}\right)$, a zero Dirichlet boundary condition is imposed on m^a_k:

5.57.
$$m^a_k = 0$$

Note that the area integrals of equation *(5.51)* are zero on any other surface than S_{Mb},

5.2.3.B.b.II. Outlet

At the outlet, since S_O is fixed, $\delta x_k/\delta b_n = 0$ and from the primal boundary conditions, the following is true:

5.58.
$$\frac{\delta p}{\delta b_n} = \frac{\partial p}{\partial b_n} = 0$$

As a result, the second integral in equation *(5.51)* is zero. In order to eliminate the first term, the integrant must be set equal to zero:

5.59.
$$v_i u_j n_j + \left(v + v_t\right)\left(\frac{\partial v_i}{\partial x_j} + \frac{\partial v_j}{\partial x_i}\right)n_j - q n_i + \tilde{v}_a \tilde{v} C_Y \frac{1}{Y} e_{mjk} \frac{\partial u_k}{\partial x_j} e_{mli} n_l + \frac{\partial F_{S_k}}{\partial u_i} n_k = 0$$

In the case of 3D flows, equation *(5.59)* includes four unknown quantities (the three components of the adjoint velocity and the adjoint pressure). Therefore, one of them must be extrapolated from the interior of the domain. This is chosen to be the normal component of the adjoint velocity v_n. By multiplying equation *(5.59)* with the normal to the surface vector n_i the adjoint pressure can be determined as:

5.60.
$$q = v_{\langle n \rangle} u_{\langle n \rangle} + 2\left(v + v_t\right)\frac{\partial v_{\langle n \rangle}}{\partial n} + \frac{\partial F_{S_k}}{\partial u_i} n_i n_k + \tilde{v}_a \tilde{v} C_Y \frac{1}{Y} e_{mjk} \frac{\partial u_k}{\partial x_j} e_{mli} n_l n_i = 0$$

The tangential adjoint velocity components can be obtained by multiplying equation *(5.59)* with the tangent to the surface vectors t^I_i, t^{II}_i, as following, and solving the resultant Robin boundary condition:

$$5.61. \qquad u_n v_{\langle t \rangle} + \left(v + v_t \right) \left(\frac{\partial v^I_{\langle t \rangle}}{\partial n} + \frac{\partial v_{\langle n \rangle}}{\partial t^I_i} \right) + \frac{\partial F_{S_k}}{\partial u_i} n_k t^I_i - \tilde{v}_a \tilde{v} C_Y \frac{1}{Y} e_{mjk} \frac{\partial u_k}{\partial x_j} e_{mzi} n_z t^I_i = 0$$

After zeroing the coefficient of $\partial \tilde{v}/\partial b_n$, a Robin boundary condition is imposed on $\tilde{v}_a$:

$$5.62. \qquad \tilde{v}_a u_j n_j + \left(v + \frac{\tilde{v}}{\sigma} \right) \frac{\partial \tilde{v}_a}{\partial x_j} n_j + \frac{\partial F_{S_k}}{\partial \tilde{v}} n_i = 0$$

A zero Dirichlet boundary condition is imposed on m^a_k.

5.2.3.B.b.III. Road, Side & Top

At the road, side and top, namely the fixed walls of the domain, the primal boundary conditions are similar to those imposed at the inlet. The resultant adjoint boundary conditions are the following:

$$5.63. \qquad v_{\langle n \rangle} = -\frac{\partial F_{S_{w,i}}}{\partial p} n_i$$

$$5.64. \qquad v^I_{\langle t \rangle} = \frac{\partial F_{S_{w,k}}}{\partial \tau_{ij}} n_k t^I_i n_j + \frac{\partial F_{S_{w,k}}}{\partial \tau_{ij}} n_k t^I_j n_i$$

$$5.65. \qquad v^{II}_{\langle t \rangle} = \frac{\partial F_{S_{w,k}}}{\partial \tau_{ij}} n_k t^{II}_i n_j + \frac{\partial F_{S_{w,k}}}{\partial \tau_{ij}} n_k t^{II}_j n_i$$

along with a zero Dirichlet condition for $\tilde{v}_a$, m^a_k and a zero Neumann condition for the adjoint pressure.

5.2.3.B.b.IV. Symmetry Plane

On the symmetry plane, the objective function is not defined. In order to set the remaining terms of equation *(5.51)* equal to zero, the following boundary conditions are set:

$$5.66. \qquad v_{\langle n \rangle} = 0$$

$$5.67. \qquad \frac{\partial v^I_{\langle t \rangle}}{\partial n} = 0$$

A symmetry plane boundary condition is imposed on $\tilde{v}_a$.

Again, a zero Dirichlet condition for m^a_k and a zero Neumann condition for the adjoint pressure are imposed.

5.2.3.B.c. On The Vehicle

The vehicle surface is the parameterized geometry of the simulation, that may vary through the simulation cycles. While $\delta u_i / \delta b_n = 0$, in general it is $\delta x_k / \delta b_n \neq 0$. As a result, taking equation *(5.8)* into account, the following is true:

$$5.68. \qquad \frac{\partial u_i}{\partial b_n} = -\frac{\partial u_i}{\partial x_k} n_k \frac{\delta x_m}{\delta b_n} n_m$$

The first integral of equation *(5.51)* is analyzed as:

$$5.69. \quad \oiint_{S_{M_b}} \left[v_i u_{\langle n \rangle} + (\nu + \nu_t) \left(\frac{\partial v_i}{\partial x_j} + \frac{\partial v_j}{\partial x_i} \right) n_j - q n_i \right] \frac{\partial u_i}{\partial b_n} \, dS = \oiint_{S_{M_b}} \left[(\nu + \nu_t) \left(\frac{\partial v_i}{\partial x_j} + \frac{\partial v_j}{\partial x_i} \right) n_j - q n_i \right] \frac{\partial u_i}{\partial b_n} n_k \frac{\delta x_m}{\delta b_n} n_m \, dS$$

The resultant integral contains terms only from the primal and the adjoint fields and from the surface displacement, as a result it can be computed and added to the sensitivity derivatives expression.

The second and third integrals can be also set equal to zero, by imposing the following conditions:

$$5.70. \qquad v_{\langle n \rangle} = -\frac{\partial F_{S_{M_b},i}}{\partial p} n_i$$

$$5.71. \qquad v^I_{\langle t \rangle} = \frac{\partial F_{S_{M_b},k}}{\partial \tau_{ij}} n_k t^I_i n_j + \frac{\partial F_{S_{M_b},k}}{\partial \tau_{ij}} n_k t^I_j n_i$$

$$5.72. \qquad v^{II}_{\langle t \rangle} = \frac{\partial F_{S_{M_b},k}}{\partial \tau_{ij}} n_k t^{II}_i n_j + \frac{\partial F_{S_{M_b},k}}{\partial \tau_{ij}} n_k t^{II}_j n_i$$

A zero Dirichlet condition for $\tilde{v}_a$, m^a_k and a zero Neumann condition for the adjoint pressure are imposed.[45]

5.2.3.C. Final Expression Of The Sensitivity Derivatives

After satisfying the adjoint mean flow equations, the adjoint turbulence model equations and the adjoint boundary conditions, the final expression of the sensitivity derivatives formulated by the E-SI approach is:[46]

5.73.

$$
\begin{aligned}
\frac{\delta F_{aug}}{\delta b_n} = & \oiint_{S_{M_b}} \left[(v + v_t)\left(\frac{\partial v_i}{\partial x_j} + \frac{\partial v_j}{\partial x_i} \right) n_j - q n_i + \frac{\partial F_{S_{M_b,l}}}{\partial u_i} n_l \right] \frac{\partial u_i}{\partial b_n} \frac{\delta x_m}{\delta b_n} dS \\
& + \oiint_{S_{M_b}} \frac{\partial F_{S_{M_b,i}}}{\partial x_m} \frac{\partial u_i}{\partial b_n} n_i \frac{\delta x_k}{\delta b_n} dS + \oiint_{S_{M_b}} F_{S_{M_b,i}} n_i \frac{\delta(dS)}{\delta b_n} \\
& + \oiint_{S_{M_b}} \frac{\partial m_i^a}{\partial x_j} n_i \frac{\delta x_i}{\delta b_n} dS \\
& - \oiint_{S_{M_b}} \left[\left(-v_k n_k + \frac{\partial F_{S_{M_b,k}}}{\partial \tau_{lz}} n_k n_l n_z \right) \left(\tau_{ij} \frac{\delta(n_i n_j)}{\delta b_n} + \frac{\partial \tau_{ij}}{\partial x_m} \frac{\delta x_k}{\delta b_n} n_i n_j \right) \right] dS \\
& - \oiint_{S_{M_b}} \left[\frac{\partial F_{S_{M_b,k}}}{\partial \tau_{lz}} n_k t_l^I t_z^I \left(\tau_{ij} \frac{\delta(t_i^I t_j^I)}{\delta b_n} + \frac{\partial \tau_{ij}}{\partial x_k} n_k \frac{\delta x_k}{\delta b_n} t_i^I t_j^I \right) \right] dS \\
& - \oiint_{S_{M_b}} \left[\left(\frac{\partial F_{S_{M_b,k}}}{\partial \tau_{lz}} n_k \left(t_l^{II} t_z^I + t_l^I t_z^{II} \right) \right) \left(\tau_{ij} \frac{\delta(t_i^{II} t_j^I)}{\delta b_n} + \frac{\partial \tau_{ij}}{\partial x_k} n_k \frac{\delta x_k}{\delta b_n} t_i^{II} t_j^I \right) \right] dS \\
& - \oiint_{S_{M_b}} \left[\left(\frac{\partial F_{S_{M_b,k}}}{\partial \tau_{lz}} n_k t_l^{II} t_z^{II} \right) \left(\tau_{ij} \frac{\delta(t_i^{II} t_j^{II})}{\delta b_n} + \frac{\partial \tau_{ij}}{\partial x_k} \frac{\delta x_k}{\delta b_n} t_i^{II} t_j^{II} \right) \right] dS
\end{aligned}
$$

It is noted that for the optimization with the FFD method, the FI approach for the sensitivity derivatives is used, which results in the following expression:

5.74.

$$\frac{\delta F_{aug}}{\delta b_n} = \iiint_{\mho} \left(-v_i u_j \frac{\partial u_i}{\partial x_k} - u_j \frac{\partial p}{\partial x_k} - \tau_{ij}^a \frac{\partial u_i}{\partial x_k} + u_i \frac{\partial \tau_{ij}^a}{\partial x_k} + q \frac{\partial u_j}{\partial x_k} \right) \frac{\partial}{\partial x_j} \left(\frac{\delta x_k}{\delta b_n} \right) d\mho$$

$$+ \oiint_{S_{M_b}} F_{S_{M_b,i}} n_i \frac{\delta(dS)}{\delta b_n}$$

$$- \oiint_{S_{M_b}} \left(-v_k n_k + \frac{\partial F_{S_{M_b,k}}}{\partial \tau_{lz}} n_k n_l n_z \right) \tau_{ij} \frac{\delta(n_i n_j)}{\delta b_n} dS$$

$$- \oiint_{S_{M_b}} \frac{\partial F_{S_{M_b,k}}}{\partial \tau_{lz}} n_k t_l^I t_z^I \tau_{ij} \frac{\delta(t_i^I t_j^I)}{\delta b_n} dS$$

$$- \oiint_{S_{M_b}} \left(\frac{\partial F_{S_{M_b,k}}}{\partial \tau_{lz}} n_k \left(t_l^{II} t_z^I + t_l^I t_z^{II} \right) \right) \tau_{ij} \frac{\delta(t_i^{II} t_j^I)}{\delta b_n} dS$$

$$- \oiint_{S_{M_b}} \left(\frac{\partial F_{S_{M_b,k}}}{\partial \tau_{lz}} n_k t_l^{II} t_z^{II} \right) \tau_{ij} \frac{\delta(t_i^{II} t_j^{II})}{\delta b_n} dS$$

The computation of the sensitivity derivatives are finally used in determining the next set of design variables, for the next optimization cycle, using the steepest descent method:

5.75.

$$b_n\big|^{new} = b_n\big|^{old} - \eta \frac{\delta F}{\delta b_n}$$

where η is a weighing factor.

5.3. Results

5.3.1. Convergence

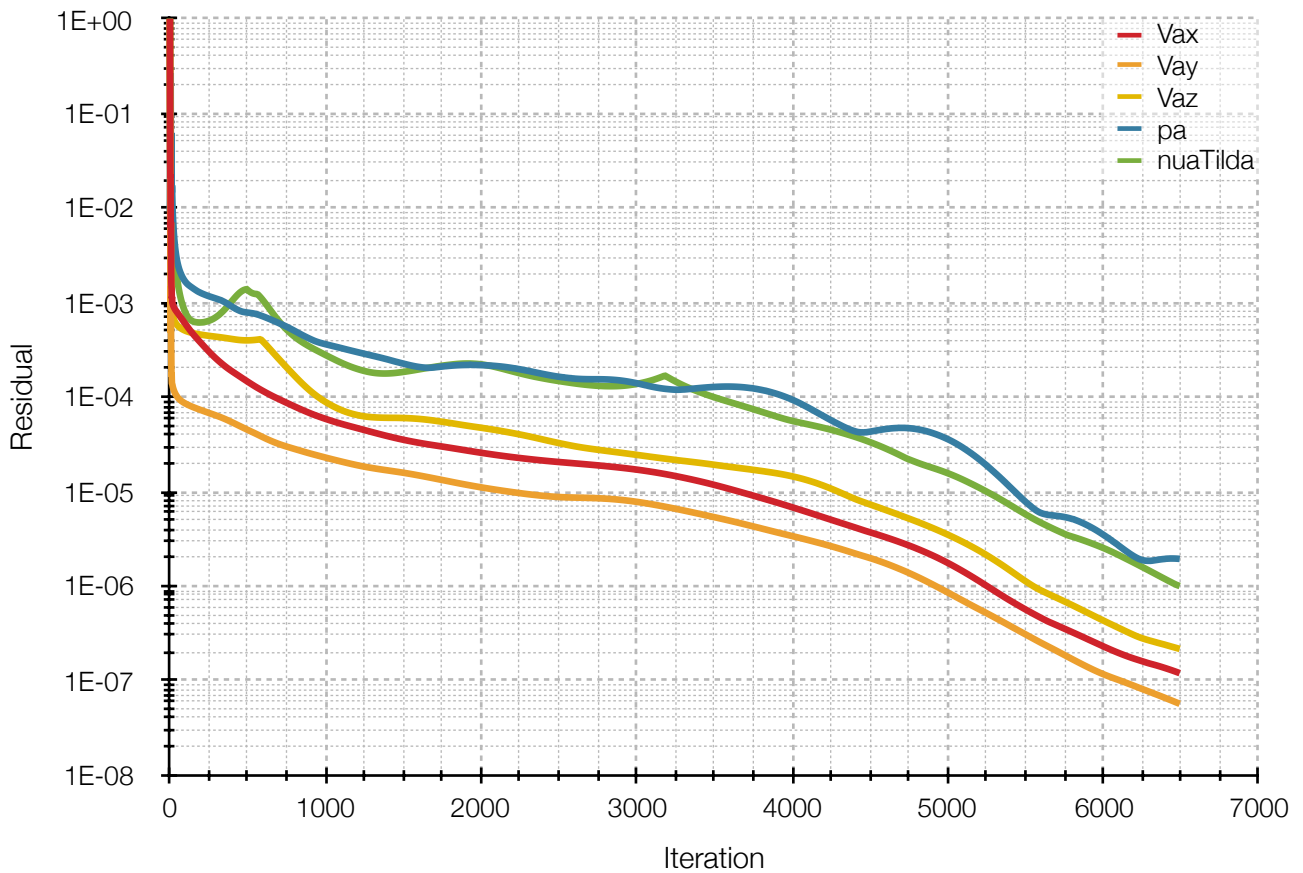The residuals of the adjoint equations during the simulation are presented in figure 5.2.

Figure 5.2: Convergence of the residuals of the adjoint flow equations during the simulation.

It is clearly shown that the mean value of the residuals has been reduced significantly and noticeably faster that the primal residuals.

The fields presented onwards concern the last iteration of the solution.

5.3.2. Adjoint Flow Field

5.3.2.A. Adjoint Velocity

In figure 5.3, the adjoint velocity magnitude at the car symmetry plane is shown.

Figure 5.3: Adjoint velocity magnitude at the modified car symmetry plane.

It is noted that most of the field is apparently very small on magnitude, however there are high velocity areas at the front of the splitter, the tip of the spoiler and the tip of the diffuser.

In figures 5.4 to 5.7, the adjoint velocity magnitude distribution on the car body is shown. It is noted that no boundary condition sets the adjoint velocity to zero on the vehicle body, as in the primal velocity.

Figure 5.4: Adjoint velocity magnitude distribution on the modified car body, in front 3/4 high elevation view. Results are presented on the right half of the car.
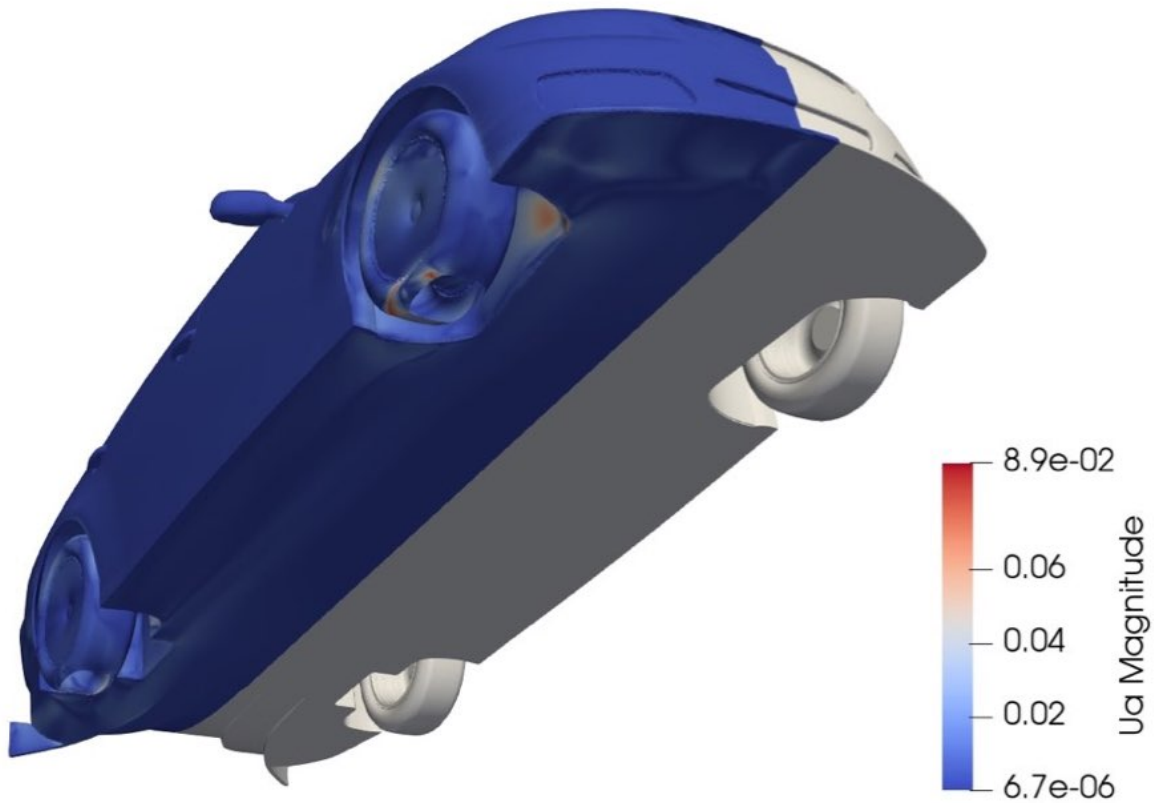
Figure 5.5: Adjoint velocity magnitude distribution on the modified car body, in front 3/4 low elevation view. Results are presented on the right half of the car.

Figure 5.6: Adjoint velocity magnitude distribution on the modified car body, in rear 3/4 high elevation view. Results are presented on the right half of the car.
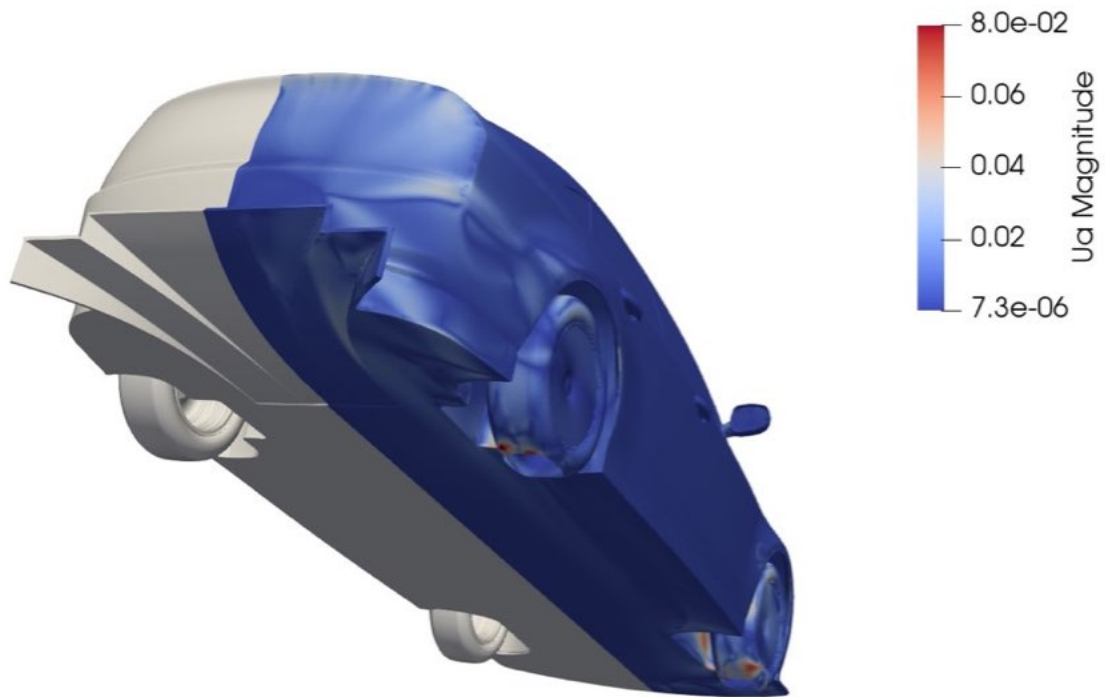
Figure 5.7: Adjoint velocity magnitude distribution on the modified car body, in rear 3/4 low elevation view. Results are presented on the right half of the car.

The main areas where the adjoint velocity is higher is at the rear, the front and rear edges of the underfloor and the wheels and wheel arches. The general impression given by the adjoint velocity is like the primal velocity when the vehicle is moving on reverse.

5.3.2.B. Adjoint Pressure

In figure 5.8, the adjoint pressure field on the car symmetry plane is shown.
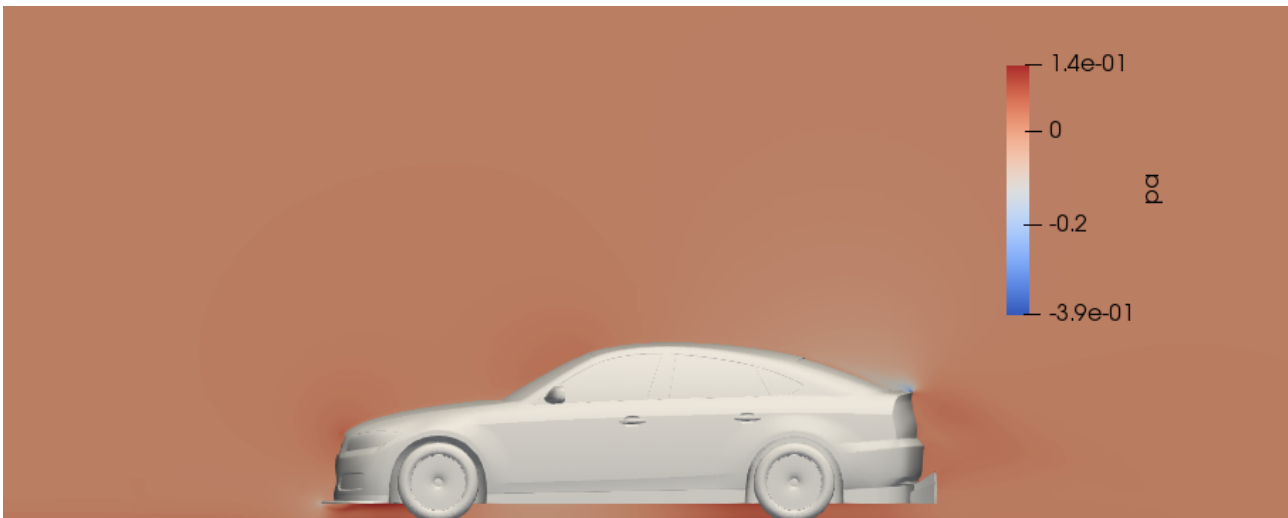

Figure 5.8: Adjoint pressure field at the modified car symmetry plane.

The adjoint pressure field is vastly different from the primal one. The pressure is mostly uniform, with the main differences located at the tip of the front splitter and at the tip of the rear spoiler.

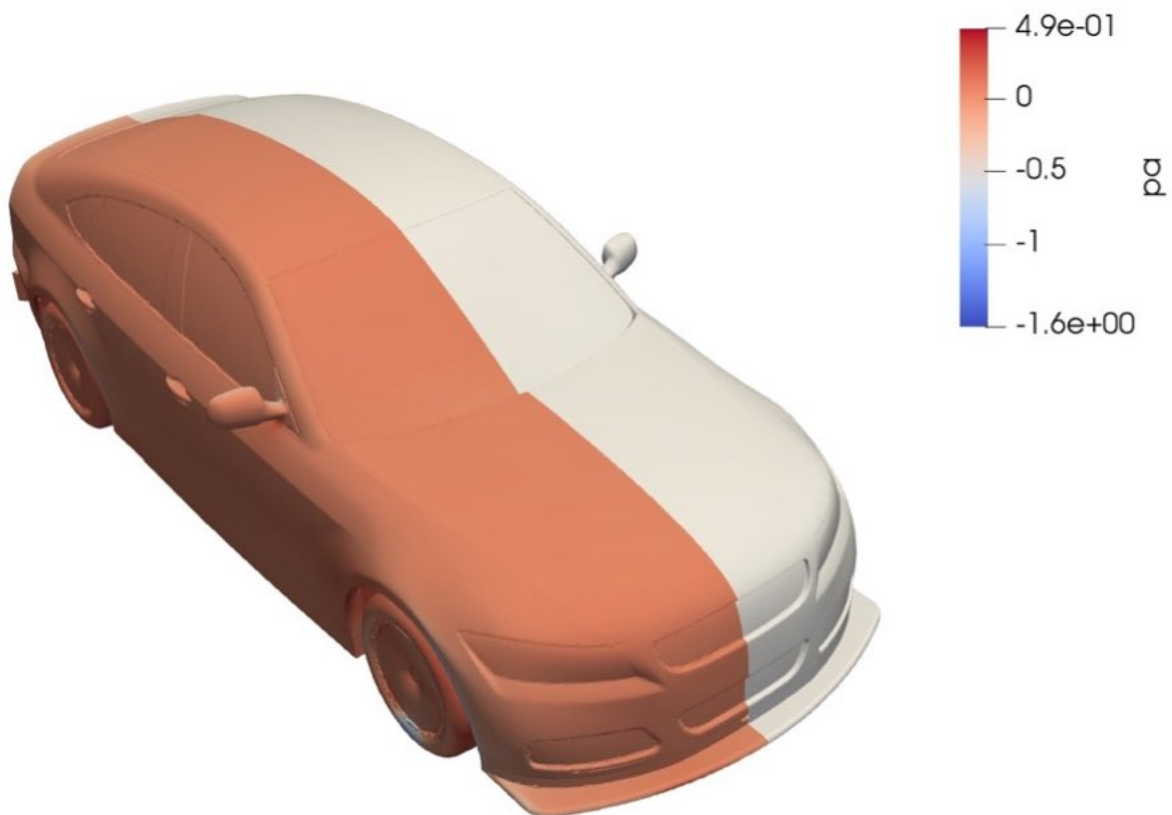In figures 5.9 to 5.12, the adjoint pressure distribution on the car body is shown.

Figure 5.9: Adjoint pressure distribution on the modified car body, in front 3/4 high elevation view. The results are presented on the right half of the car.

Figure 5.10: Adjoint pressure distribution on the modified car body, in front 3/4 low elevation view. The results are presented on the right half of the car.

Figure 5.11: Adjoint pressure distribution on the modified car body, in rear 3/4 high elevation view. The results are presented on the right half of the car.
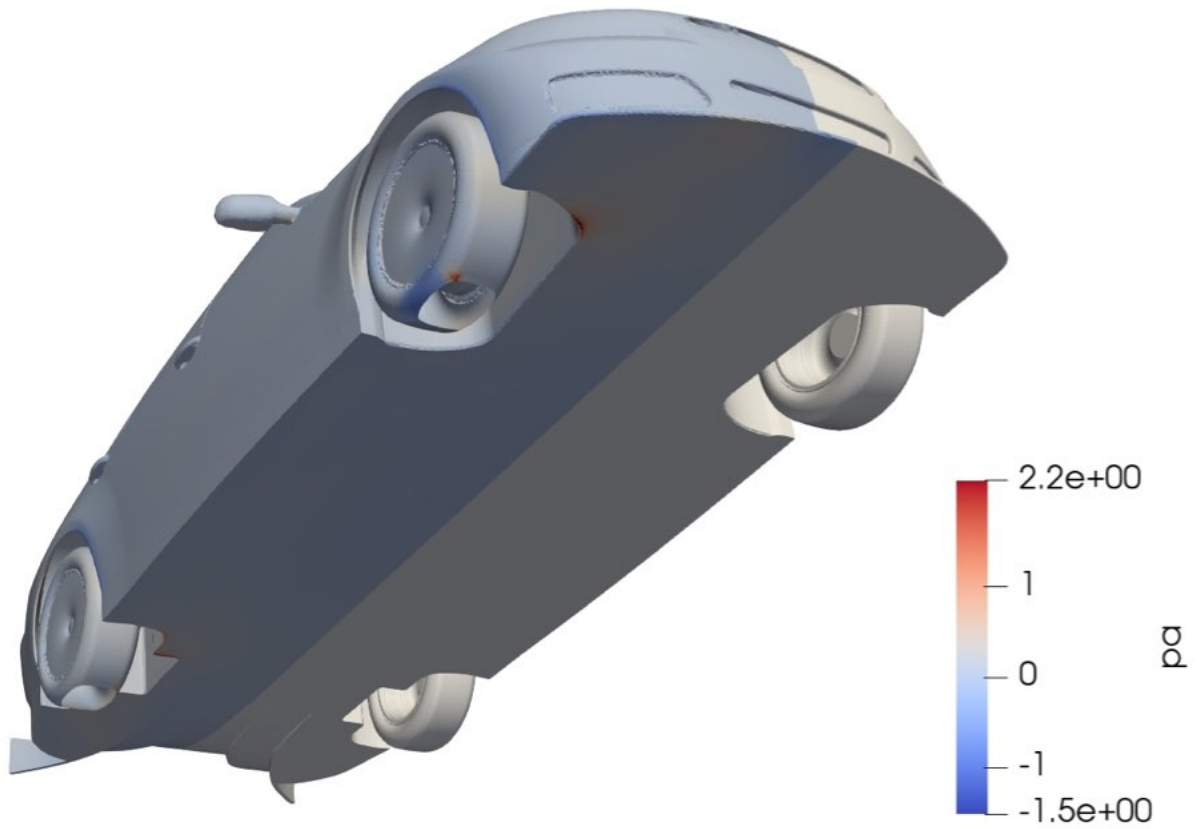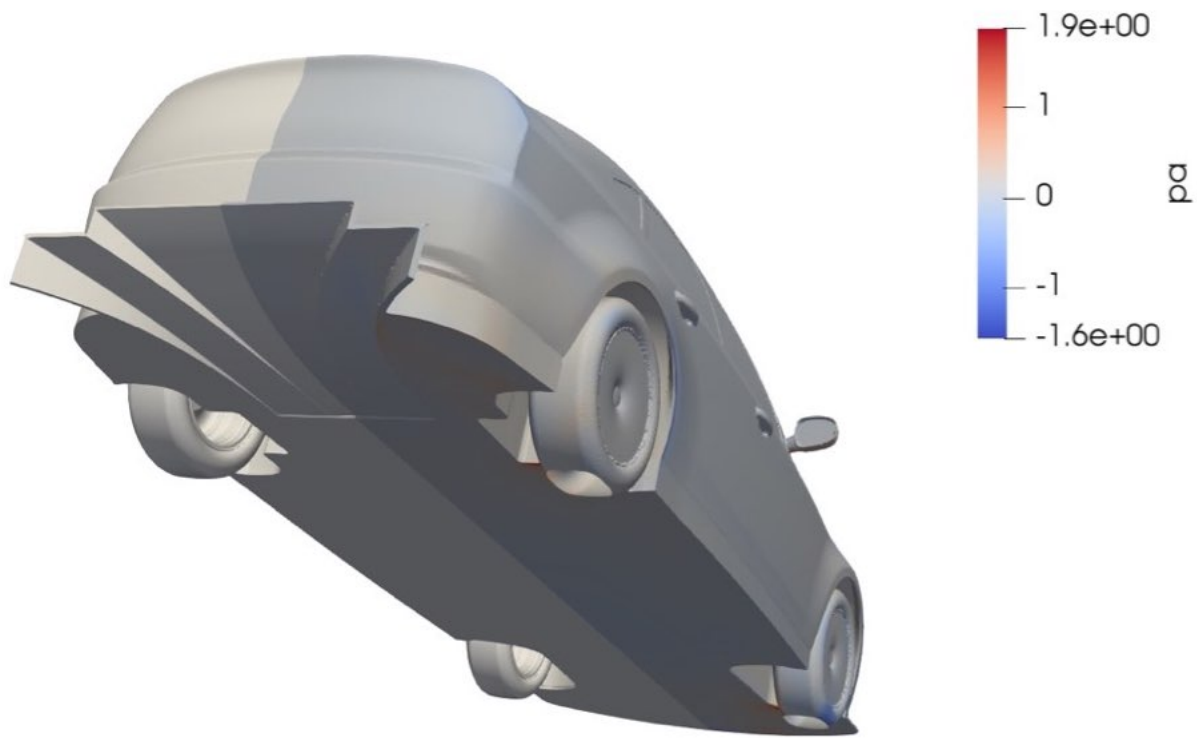
Figure 5.12: Adjoint pressure distribution on the modified car body, in rear 3/4 low elevation view. The results are presented on the right half of the car.

The adjoint pressure distribution on the vehicle body reveals further adjoint pressure peaks on the wheels and wheel arches. The rest of the distribution is again mostly uniform

5.3.2.C. Adjoint Variable $\tilde{v}$

In figure 5.13, the adjoint variable $\tilde{v}$ field at the car symmetry plane is shown.
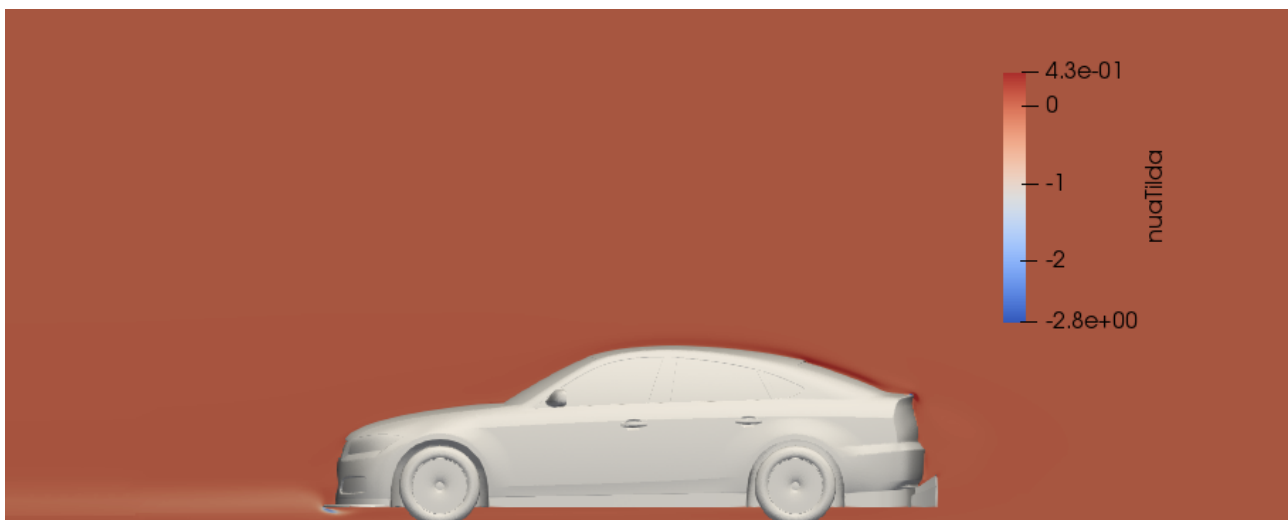

Figure 5.14: Adjoint variable $\tilde{v}$ field at the modified car symmetry plane.

The field of the adjoint variable $\tilde{v}$ is somewhat similar to this of the adjoint velocity z component, with a mostly uniform field with the exception of the rear of the vehicle and an area in front of the vehicle and close to the road.

5.3.3. Sensitivity Map

The sensitivity map is shown in figures 5.15 to 5.18. It is noted that the sensitivity derivatives are not computed on the wheels, since their geometry is fixed and a simplified smooth and closed wheel model was used.

Figure 5.15: The sensitivity map, as resulted from a single adjoint simulation, in front 3/4 high elevation view. Blue colour indicates inwards displacement and red colour indicates outwards displacement for improving the objective function. The results are presented on the right half of the car.
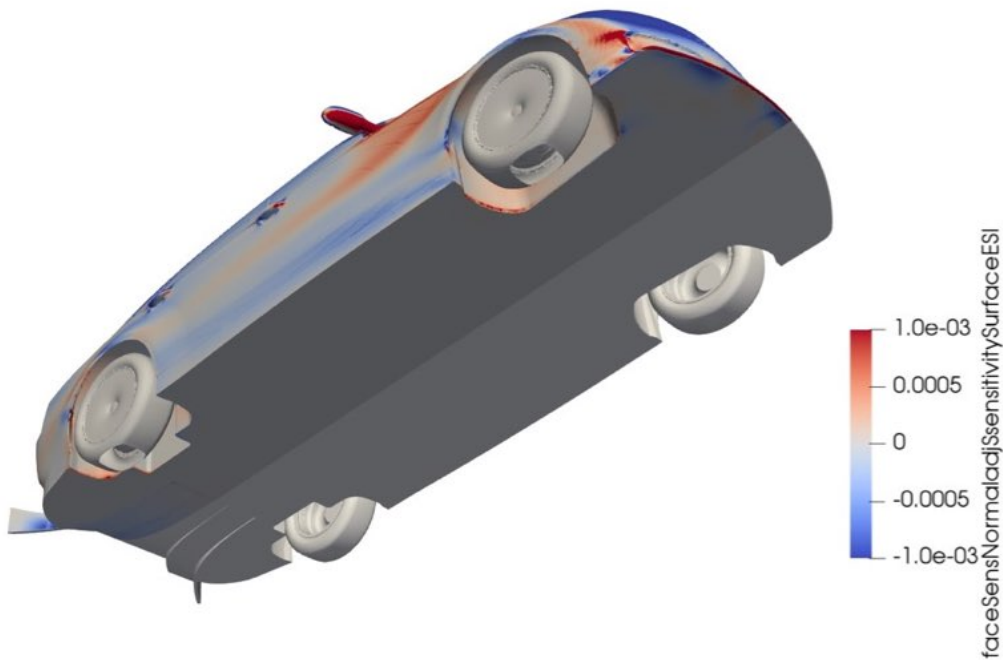
Figure 5.16: The sensitivity map, as resulted from a single adjoint simulation, in front 3/4 low elevation view. Blue colour indicates inwards displacement and red colour indicates outwards displacement for improving the objective function. The results are presented on the right half of the car.

Figure 5.17: The sensitivity map, as resulted from a single adjoint simulation, in rear 3/4 high elevation view. Blue colour indicates inwards displacement red colour indicates outwards displacement for improving the objective function. The results are presented on the right half of the car.
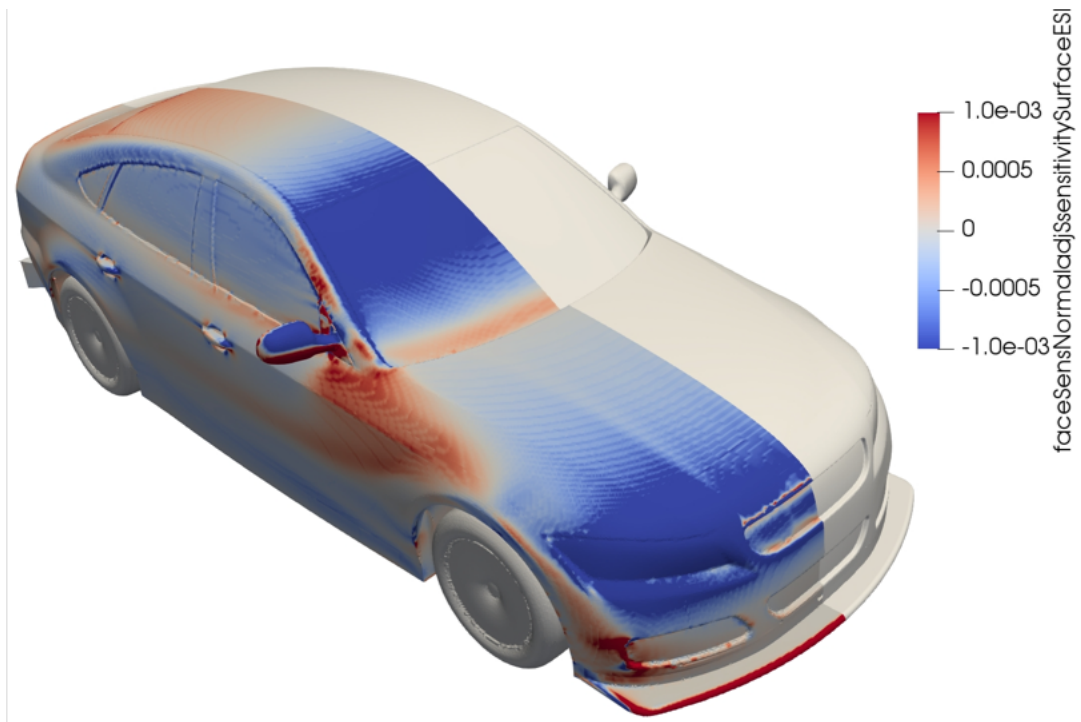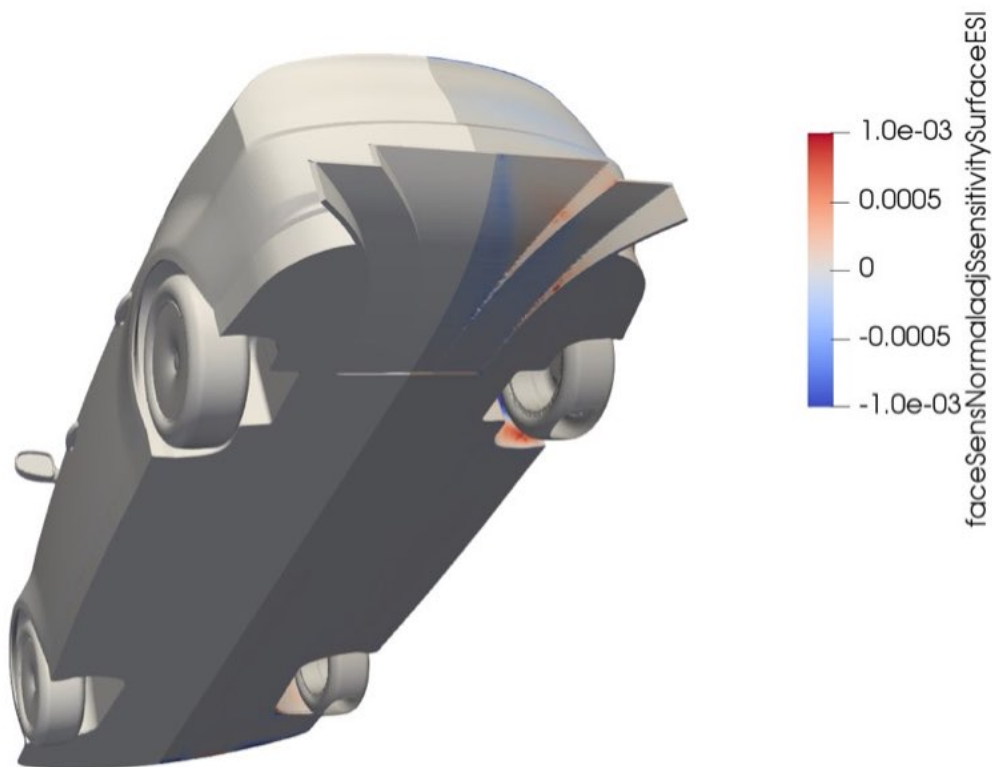

Figure 5.18: The sensitivity map, as resulted from a single adjoint simulation, in rear 3/4 low elevation view. Blue colour indicates inwards displacement and red colour indicates outwards displacement for improving the objective function. The results are presented on the right half of the car.
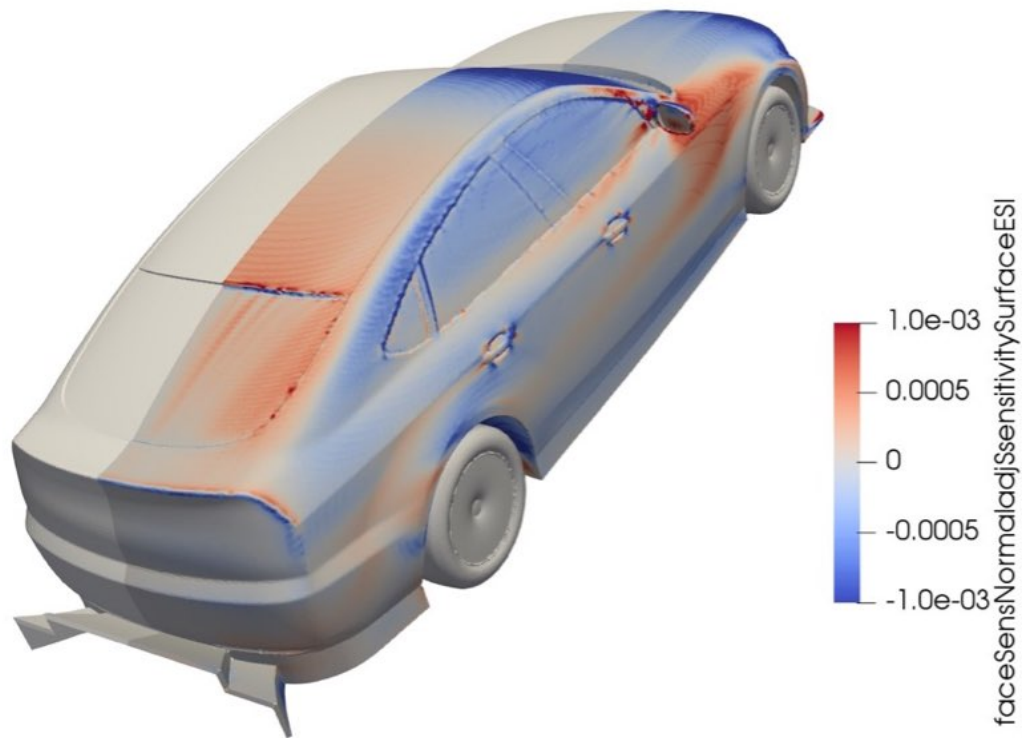
It is noted that, in order to increase the downforce, the sensitivity map suggests:

- The elongation of the front splitter,
- The elevation of the tip of the front splitter,
- Pushing the area of the headlights and the top of the front windscreen inwards, since this is an area where the velocity is accelerated, thus reducing the pressure and creating lift,
- Modifying the profile of the rear diffuser,
- The creation or larger spoilers at the rear of the car and on top of the rear windscreen,
- Morphing the side mirrors into a more wing-like shape,
- Pulling a large area of the front fenders and the front doors outwards,
- Pushing parts of the A-pillar inwards,
- Small alterations of the inside of the wheel arches.

6. Shape Optimization

6.1. Theoretical Background

6.1.1. Introduction - Free Form Deformation Method

The FFD Method uses a set of movable control points in the 3D computational domain, in the form of a structured grid, in order to displace CFD mesh points located inside the control grid.

The method has been developed and coupled with the adjoint solver by the PCOpt Unit of the NTUA.

In order for the method to function, the following two procedures must be successfully completed:

- The parameterization of a part of the surface, or the whole of the surface of an aerodynamic body by defining the control points in 3D space. The x, y and z components of the control points are used as the design variables, meaning that for N control points there will be $3N$ design variables.

- The displacement of the surface and volume nodes of the CFD mesh in each optimization iteration, according to the value of the sensitivity derivatives.

The method exhibits great potential since the cost of each mesh movement is extremely small, when compared to the solution of the mean flow equations, the minimum degree of surface continuity can be defined a-priori and the setup of each case is not cumbersome. The main advantages of the FFD software under consideration include:

- The relatively expensive part of the algorithm has to be done only once. Fine-grained parallelization can be used to reduce as much as possible the corresponding time. The computed parametric coordinates are then stored for use in the same (or any subsequent) optimization loop.

- Each mesh movement step can be computed very fast, through a closed-form expression, which can also be differentiated analytically.

- Local shape deformations can be applied by adding control points and lowering the basis functions degree.

- The minimum degree of surface continuity can be determined beforehand.

- Since the displaced meshes are not affected by the number of steps required to achieve the final geometries but only from the final coordinates of the control points, very big mesh deformations can be achieved even in a single step.

- Mesh elements are guaranteed not to overlap, as long as the control grid edges do not overlap either.

- The mesh quality is generally preserved to standards than allow the solution of the primal and, the numerically stiffer, adjoint equations.

6.1.2. B-Splines Curves

Let b_i, $i \in [0, n]$ be the control points of a parameterized curve $x(u)$. In the case of a B-splines curve, $x(u)$ is given by:

6.1.
$$x(u) = \sum_{i=0}^{n} U_{i,p}(u) b_i$$

where:

- $U_{i,p}(u)$ is the i-th basis function with a degree of p,

- $u \in [0, 1]$.

The Einstein's convention is also assumed hereafter.

By defining additional control points, equation *(6.1)* can be used to give the y and z coordinates of a 2D and 3D curve, respectively.

The resulting x curve is a piecewise polynomial function, with each polynomial being of a maximum degree of p. In order to define the basis function $U_{i,p}(u)$, a set of knots in ascending order, known as the knot vector, ξ_i, $i \in [0, m]$, $m = n + p + 1$, must first be defined. Knots may be present in the knot vector more than once. The following knot vector ξ is used:

6.2.
$$\vec{\xi} = \left[\underbrace{0 \quad \cdots \quad 0}_{p+1} \quad \frac{1}{N} \quad \cdots \quad \frac{N-1}{N} \quad \underbrace{1 \quad \cdots \quad 1}_{p+1} \right]$$

where N = n – p + 1.

This knot vector results to closed curves, i.e. curves that pass through the first and last control points. The number of control points has to exceed the curve degree by at least one.

The knot span is defined by two consecutive knots. The zero order basis function is given by:

6.3.
$$U_{i,0}(u) = \begin{cases} 1 & \text{if} \quad \xi_i \leq u < \xi_{i+1} \\ 0 & \text{elsewhere} \end{cases}$$

And the higher degree basis functions are given by:

6.4.
$$U_{i,p}(u) = \frac{u - \xi_i}{\xi_{i+p} - \xi_i} U_{i,p-1}(u) + \frac{\xi_{i+p+1} - u}{\xi_{i+p+1} - \xi_{i+p}} U_{i+1,p-1}(u)$$

If, during the computation of the basis function values, the term 0/0 appears, its value is set to 0.

Each basis function and, consequently, each control point, is affecting only the curve points with a parametric coordinate residing in the $p+1$ spans, as defined by [ξ_i, ξ_{i+p+1}). This enables the alteration of a certain part of the curve while keeping the rest of it intact. In other words, the B-splines have the property of local support. The range of the locality can be controlled by altering the curve degree p. Smaller values of the curve degree correspond to more localized support.

The continuity of the resultant curve can also be determined beforehand. The B-spline curves are continuously differentiable in the interior of the knot span, since they are piecewise polynomial functions. The curve continuity is finite only at the knots and is given by C^{p-k}, where k is the knot multiplicity.

6.1.3. Volumetric B-Splines

Let b_m^{ijk}, $m \in \{1, 2, 3\}$, $i \in [0, I]$, $j \in [0, J]$, $k \in [0, K]$ be the Cartesian coordinates of the *ijk*-th control points of the 3D structured control grid. I, J, K are the number of control points per control grid direction. In the case of volumetric B-splines, the Cartesian coordinates $\boldsymbol{x} = [x_1, x_2, x_3]^T = [x, y, z]^T$ of a CFD mesh point residing within the boundaries defined by the control grid are given by:

6.5.
$$x_m(u,v,w) = U_{i,pu}(u)V_{j,pv}(v)W_{k,pw}(w)b_m^{ijk}$$

where:

- *U*, *V*, *W*: The B-splines basis functions,

- *pu*, *pv*, *pw*: The B-splines basis functions' respective degrees, which may differ per control grid direction.

In this case, $\boldsymbol{u} = [u_1, u_2, u_3]^T = [u, v, w]^T$ are the mesh point parametric coordinates.

The computation of the Cartesian coordinates of any parameterized mesh point is straightforward, at a negligible computational cost, as long as its parametric coordinates u_m are known. Mesh parametric coordinatesare computed with accuracy, since a mapping from $\mathbb{R}^3(x, y, z) \rightarrow \mathbb{R}^3(u, v, w)$ is required. Consequently, B-splines can reproduce any input geometry with machine accuracy. Other surface fittings, Tsuch as NURBS, fail to achieve such accuracy, since an approximate mapping $\mathbb{R}^3(x, y, z) \rightarrow \mathbb{R}^3(u, v, w)$ is performed.

Given the control points position, the knot vectors and the basis functions degrees, the parametric coordinates (u, v, w) of a point with Cartesian coordinates $\boldsymbol{r} = [x_r, y_r, z_r]^T$ are computed by solving the following system of equations:

6.6.
$$\vec{R}(u,v,w) = \begin{bmatrix} x(u,v,w) - x_r = 0 \\ y(u,v,w) - y_r = 0 \\ z(u,v,w) - z_r = 0 \end{bmatrix}$$

where the x_m are computed with equation *(6.5)* given tlevalues of $\boldsymbol{b}$.

The 3×3 system of equation *(6.6)* is independently solved for each parameterized mesh point by computing and inverting the Jacobian $\partial x_m/\partial u_i$, $m, j \in \{1, 2, 3\}$, and using the Newton—Raphson method. The Jacobian matrix is computed analytically through a closed form expression resulting by differentiating equation *(6.V)* with respect to the components of $\boldsymbol{u}$. This phase may also run in parallel, since the evaluation of the parametric coordinates of each point is independent from the rest of the mesh points.

In addition, the aforementioned process has to be executed only once. Afterwards, after moving the control points $\boldsymbol{b}$, the Cartesian coordinates of each internal of boundary mesh point that is located within the control grid can be easily computed with *(6.5)* and with minimal computational costs.

Furthermore, since x_m depends only on (u, v, w) (which remain unchanged whatever the change in $\boldsymbol{b}$) and $\boldsymbol{b}$, the deformed meshes are step-independent. This means that, for a given final control points position, the same mesh quality will be obtained independent of the number of steps taken to reach that position. RBF-based or Laplacian-based mesh displacement algorithms, for instance, lack this ability.

6.2. Optimization Procedure

The aforementioned software has been coupled with the adjoint solver in the OpenFOAM environment. This results in a well-defined iterated optimization procedure that can be executed within the OpenFOAM environment.

In list form, the following steps are executed by the optimization loop:[47]

1. Define the control grid to enclose the part of the geometry to be optimized. Increasing the control points number and decreasing the basis functions degree lead to more localized (but less smooth) geometry changes. A basis function degree $p \geq 3$ should be used,

2. Find which CFD mesh points reside within the boundaries of the control grid. These are the points to be parameterized (i.e. parametric coordinates (u, v, w) should be computed for each one of them in step 3) and displaced, following the control points displacement,

3. Compute the parametric coordinates $\boldsymbol{u}$ of the points found in step 2 by solving the system of equation *(6.VI)* for each one of them. The computational cost of this step increases with the number of control points and the number of the mesh points to be parameterized. Since each system is independent from the rest, the process is amenable to parallelization,

4. Solve the flow equations,

5. Compute the objective function value and apply the termination criterion,

6. Solve the adjoint equations,

7. Compute the objective function gradient with respect to the boundary CFD mesh nodes to be displaced, i.e. $\delta F/\delta x_m$ (surface sensitivities),

8. Project the surface sensitivities to control points in order to compute the control points sensitivities, using the following equation:

6.7.
$$\frac{\delta F}{\delta b_i} = \sum_{j=1}^{N_b} \sum_{m=1}^{3} \frac{\delta F}{\delta x_m^j} \frac{\delta x_m^j}{\delta b_i}$$

where N_b is the number of boundary mesh points to be displaced. Since the degree of the surface continuity is determined by the properties of B-splines, no smoothing of the computed sensitivities is required. The quantity $\delta x_m^j/\delta b_i$ is computed analytically by differentiating the linear equation *(6.V)* with respect to b_i,

9. Update the control point positions. The boundary points of the control grid are kept fixed in order to prevent an overlapping between the parameterized and non-parameterized (if any) areas of the CFD mesh,

10. Compute the new surface and volume mesh points positions through equation *(6.5)*, using the already computed parametric coordinates $\boldsymbol{u}$ associated with each one of them,

11. Move to step 4.

6.3. Areas To Be Optimized

The areas for optimization were chosen to be the front splitters and a part of the rear diffuser. An array of control points for each of those areas was defined, enclosed by an orthogonal parallelepiped. For the front splitter, an array of 11 × 18 × 7 movable control points was created, whereas for the rear diffuser the array was 13 × 15 × 10.

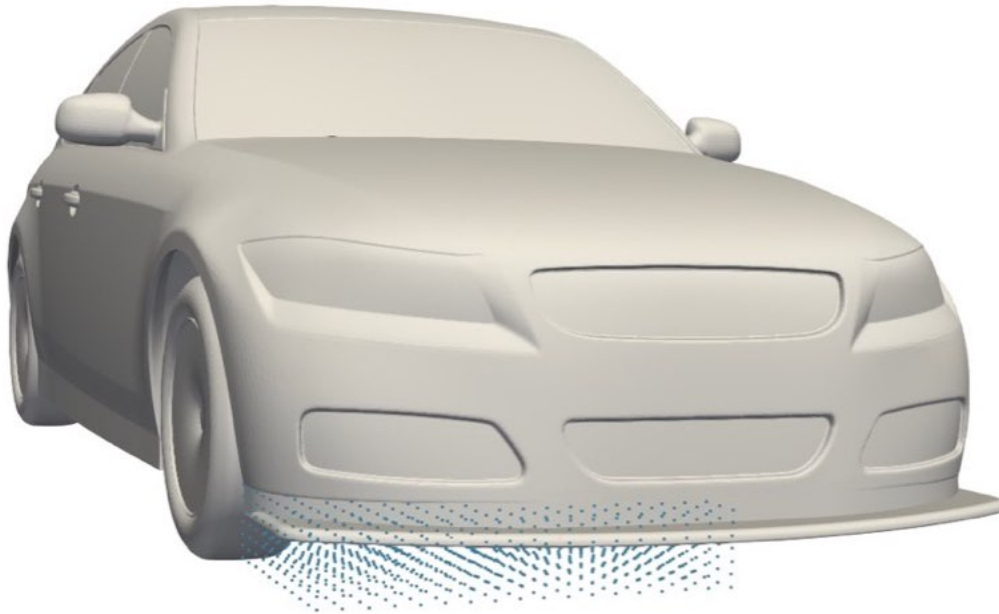In figure 6.1, the movable control points for the front splitter are shown.

Figure 6.1: The movable control points for the front splitter. Some control points are located inside the car geometry and they are not visible.

In figure 6.2, the movable control points for the rear diffuser are shown.

Figure 6.2: The movable control points for the rear diffuser. Some control points are located inside the car geometry and they are not visible.

The control points have been placed in such a way that the modified geometry will still comply to the regulations.

6.4. Results

6.4.1. Downforce

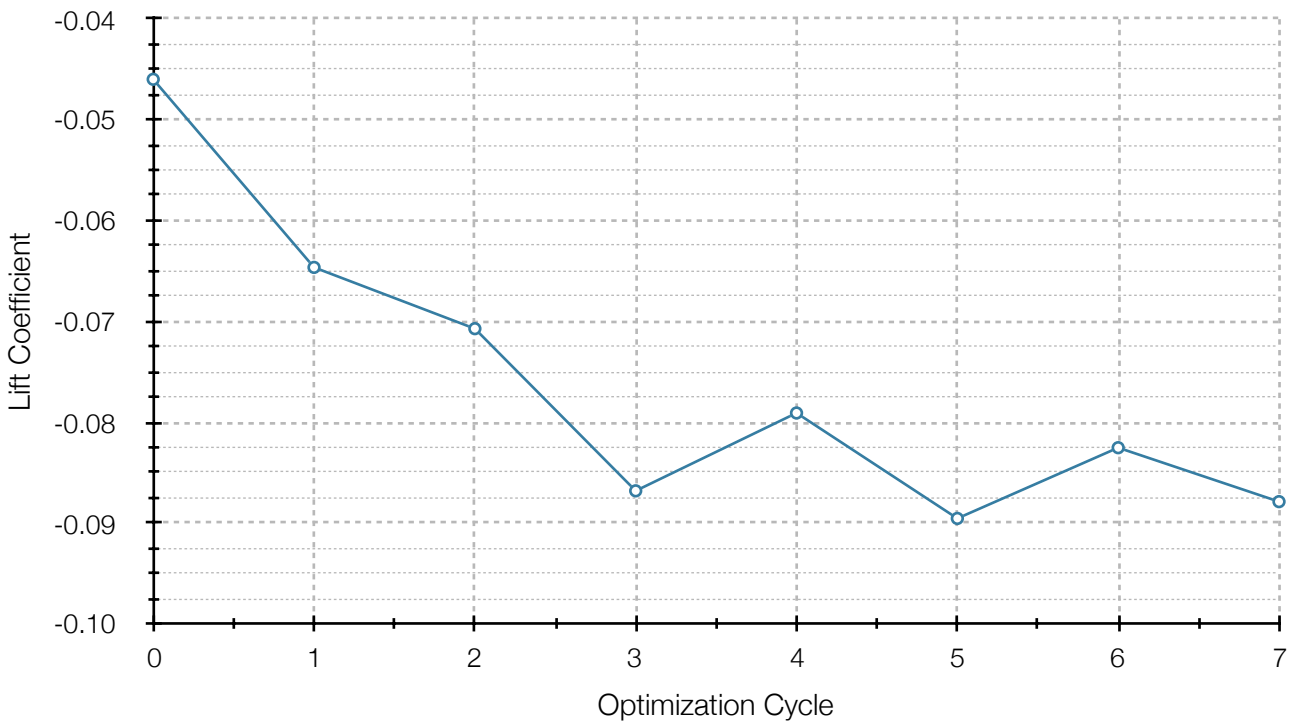The evolution of the downforce during the optimization cycle is presented in figure 6.3.

Figure 6.3: The objective of downforce at each optimization cycle.

The objective does not perfectly stabilize, due to the fact that the primal solution presents a slight oscillation in the value of the objective. After the third cycle, the results are oscillating lightly around a mean value, which is considered as the final solution. It is noted that this oscillation is due to the slightly unsteady nature of the flow.

In table 6.1, the results are shown in comparison to the original and initial geometries.

Table 6.1: Aerodynamic coefficients of the original models, the modified DrivAer and the optimized DrivAer.

Model	Coefficient	
	Drag	Lift
Original DrivAer	0.365	0.116
Modified DrivAer	0.326	-0.046
Optimized Geometry	0.327	-0.085
Difference To Original (%)	-10.41%	-173.43%
Difference To Initial (%)	0.31%	-85.16%

There is further significant downforce increase (-85%) with only marginal drag increase (0.31%).

6.4.2. Optimized Geometry

6.4.2.A. Front Splitter

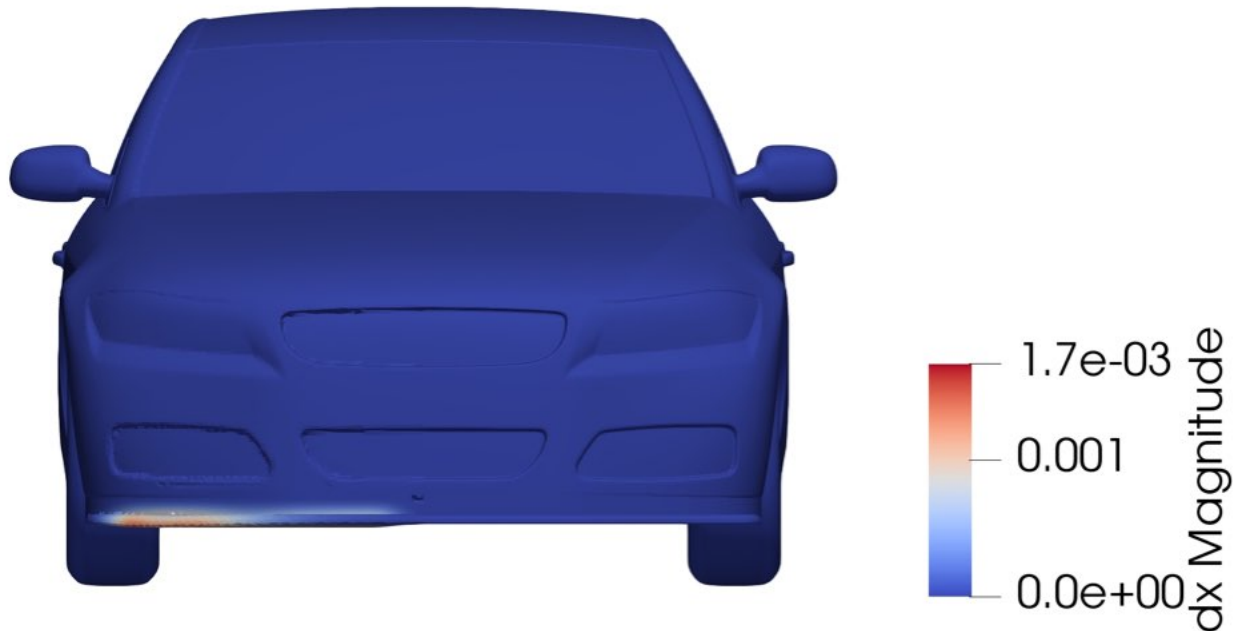In figures 6.4 to 6.7, the optimized splitter geometry in comparison to the initial geometry is presented.

Figure 6.4: The optimized splitter geometry (right side) and the initial geometry (left side) in front view. The colour map represents the magnitude of the displacement.

Figure 6.5: The optimized splitter geometry (right side) and the initial geometry (left side) in bottom view. The colour map represents the magnitude of the displacement.

Figure 6.6: The optimized splitter geometry (right side) and the initial geometry (left side) in top view. The colour map represents the magnitude of the displacement.

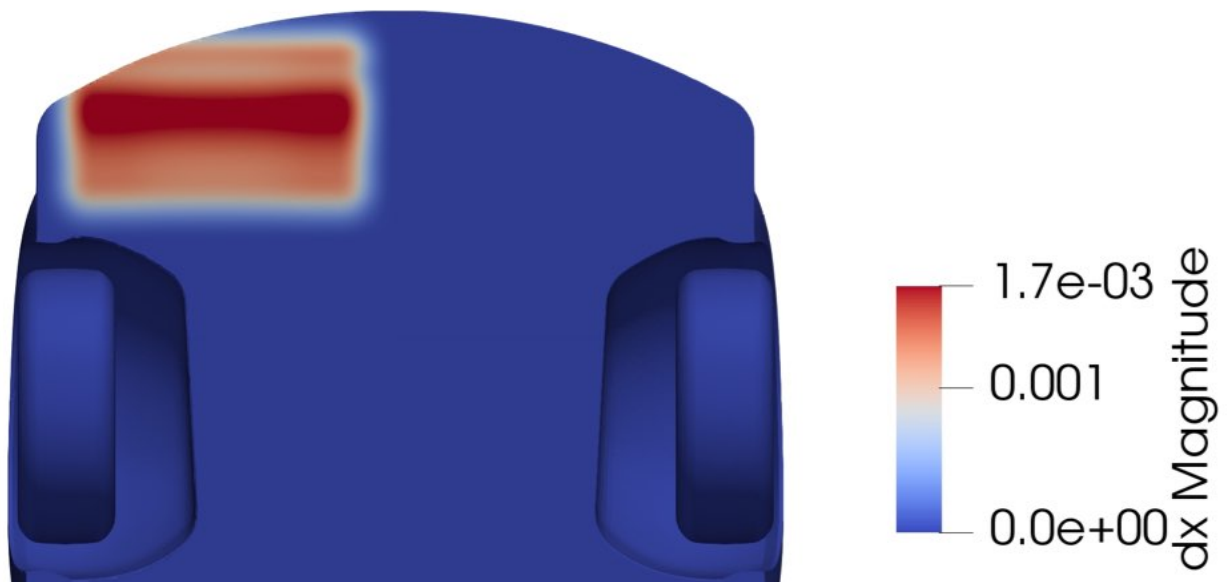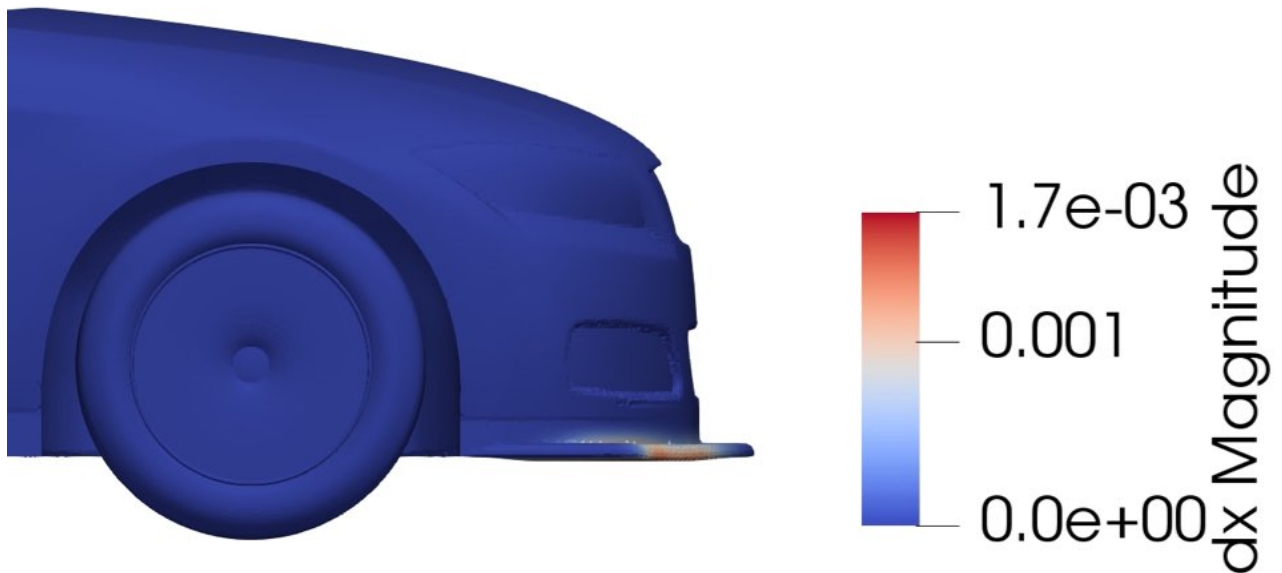

Figure 6.7: The optimized splitter geometry (right side) and the initial geometry (left side) in side view. The colour map represents the magnitude of the displacement.

The displacement is relatively small, only a few millimetres. The main modification is the thickening of the bottom side of the splitter.

6.4.2.B. Rear Diffuser

In figures 6.8 to 6.10, the optimized splitter geometry, in comparison to the initial geometry, is presented.

Figure 6.8: The optimized diffuser geometry (right side) and the initial geometry (left side) in rear view. The colour map represents the magnitude of the displacement.
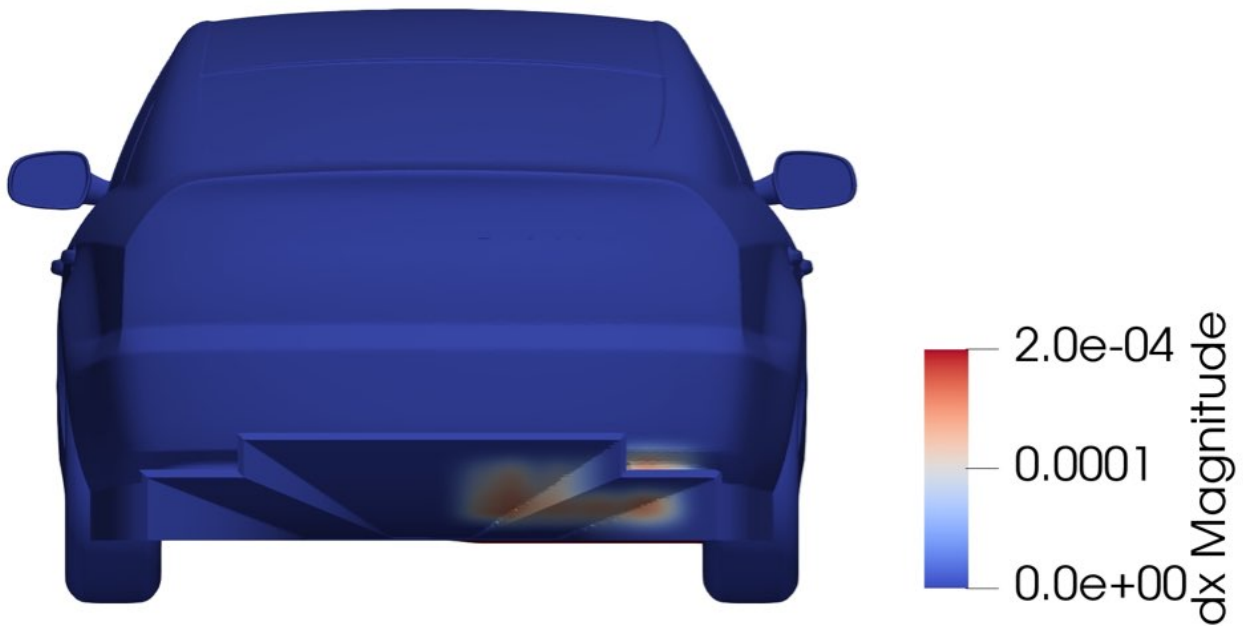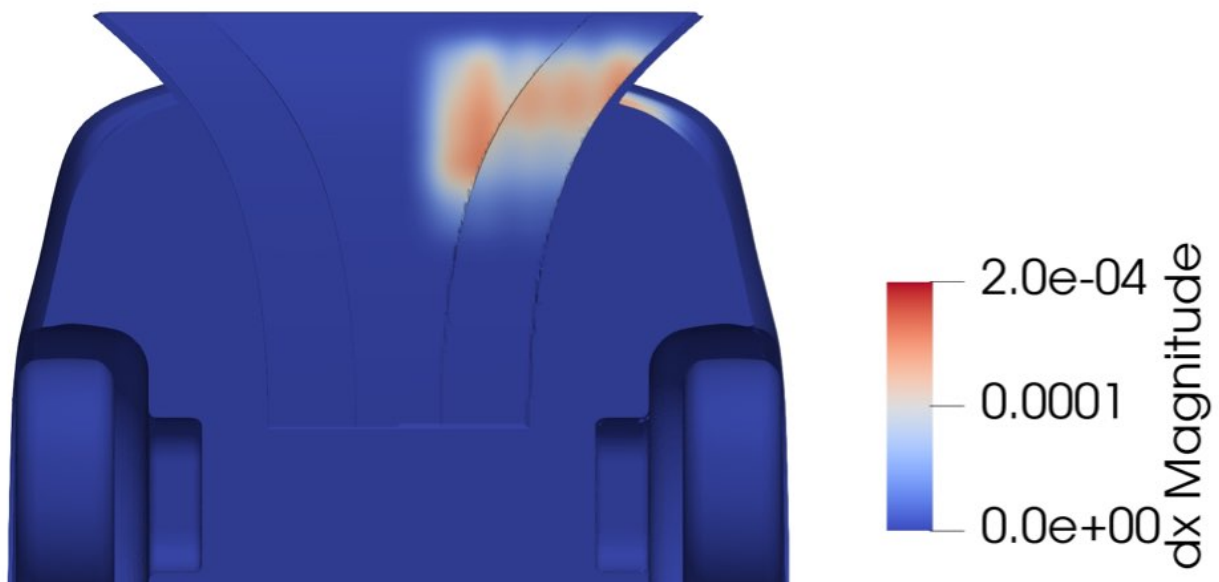

Figure 6.9: The optimized diffuser geometry (right side) and the initial geometry (left side) in bottom view. The colour map represents the magnitude of the displacement.

Again, the displacement is very small, only less that a millimetre. The main modification is a slight thickening of the diffuser walls at certain areas.

7. Concluding Remarks

7.1. Summary & Conclusion

In this Diploma Thesis, an optimization method was adapted in the DrivAer passenger car model, with the underfloor modified to the Le Mans Grand Tour Endurance racing specifications. The process is presented step by step, along with the results at every point. The main aim of the optimization is the increase of downforce, which is rarely a design specification in commercial passenger vehicles. The steps of this optimization procedure were the following:

- The creation of the modified underfloor. While this is a simple procedure, it set major setbacks in the process. The CAD software used failed to meet CFD geometry precision demands and special measures needed to be taken. The vehicle body geometry was not imported as a whole in the mesh generation software, as planned, but in separate parts, as distributed originally by its creators, along with an extra part which contained only the modifications. This procedure lasted significantly longer that planned.

- The generation of the computational mesh. After the final model was ready, the computational mesh was generated. In every mesh generation, there is a compromise between the quality of the results and the computational cost, since a much more detailed mesh yields more accurate results, but with higher computational costs, and vice versa. The final unstructured mesh was generated using primarily the *snappyHexMesh* tool in the OpenFOAM environment. During the simulations, the mesh quality was determined as acceptable and no re-meshing procedures were executed.

- The solution of the primal problem. This is the solution of the Navier—Stokes equations and the turbulence model, which was chosen to be the Spalart—Allmaras model. These equations are solved and they yield the flow field around the vehicle. Using the flow field, the aerodynamic forces acting upon the vehicle are computed. This step was completed both for the modified DrivAer model and for the original one. The results were promising, since the modifications had not only reversed the direction of the vehicle lift, producing downforce, but had also reduced the vehicle overall drag. This step was completed in the OpenFOAM environment using the SIMPLE algorithm.

- The solution of the adjoint problem. The adjoint equations are formulated using the primal equations and the objective function. The solution of the adjoint equations yield the adjoint flow field. Using the adjoint flow field, the sensitivity derivatives of the objective function with respect to the design variables are computed. The design variables in this step was the normal to the vehicle surface displacement of each surface point. The mapping of this on the car creates the sensitivity map, which indicates which areas have the greatest potential to improve the objective function. It has chosen to alter certain areas of the modified underfloor only, namely the front splitter and the rear diffuser. This step was also completed in the OpenFOAM environment using the software developed by the PCOpt Unit of the NTUA.

- The modification of the geometry using volumetric b-splines and optimization. In this step, the geometry and the computational mesh is parameterized using volumetric b-splines. The design variables now become Cartesian coordinates of the control points. As a result, in each optimization cycle, the geometry is altered by moving the control points, as indicated by the sensitivity derivatives computed by solving the adjoint field equations. The solution of the adjoint field equations require the solution of the primal equations first. This step was again completed in the OpenFOAM environment using software also developed by the PCOpt Unit of the NTUA.

A special note has to be made at this point, concerning computational costs. In CPU time, the following were generally observed:

About 6 hours of mesh generation,

About 360 hours for 20000 iterations of the primal problem,

About 150 hours for a solution to the adjoint problem,

About 1100 hours for the optimization.

It is noted that all the simulations were executed in parallel, in 36 cores of Intel Xeon E5-2630 v2 CPUs at 2.60GHz.

The adjoint problem reached far lower residuals quicker and smoother that the primal problem. Also, in the optimization cycles, the primal and adjoint fields are not reset, so the simulation initializes form already somewhat low residuals. The optimization also has the extra initial costs of computing the parameterized geometry upon initialization of solely the first cycle.

The results presented a slightly modified geometry but with significantly enhanced aerodynamic performance. The downforce was nearly doubled with negligible drag increases.

It is concluded that the optimization method with the b-splines based free form deformation can be applied at a passenger car model with motorsport specifications and can yield results of great interest. The aerodynamic performance if the vehicle is significantly improve, both in terms of downforce and in terms of drag. The modifications are considerable when compared to the original geometry and negligible to the naked eye when compared with the finial, not yet optimized geometry. However, it has to be noted that the resultant geometry may not be road legal or convenient for everyday use. The aerodynamic performance enhancement also comes with high computational costs, that should be taken into consideration for any future work.

As a result, the LMGTE modifications offer significant downforce increase along with slight drag decrease. The optimization with the FFD method using the volumetric b-splines offered further relatively small downforce increase at a small cost of drag increase. These improvements are presented in table 7.1.

Table 7.1: Aerodynamic coefficients of the original models, the modified DrivAer and the optimized DrivAer.

Model	Coefficient	
	Drag	Lift
Original DrivAer	0.365	0.116
Modified DrivAer	0.326	-0.046
Difference To Original	-0.039	-0.162
Optimized Geometry	0.327	-0.085
Difference To Modified	0.001	-0.039

7.2. Future Work

It is anticipated that future students may wish to enrich the research on the "LMGTE DrivAer". Some possible topics for consideration are listed below:

- The creation of a curved splitter,

- The creation of differently shaped rear diffuser, such as a purely rectangular or a curved one,

- The creation of openings at the sidewall of the diffuser,

- The insertion of fins in the diffuser and analyses concerning their number, size and shape,

- The analysis of the diffuser while taking into consideration the effect created by the exhaust pipes, at a single or at different exhaust positioning,

- The introduction of a rear wing,

- The simulation at a lower ride heigh, which is closer to the ride height of the LMGTE cars,

- The optimization of different areas of the vehicle, such as the spoilers and the fenders,

- The comparison of the results in this Diploma Thesis with a similar analysis, only with modifications subject to later or earlier technical regulations,

- Further modifications of the underfloor, so that it is fully road legal and more discreet, while maintaining the aerodynamic performance as high as possible,

- The optimization of the underfloor with packaging constrains of the regulations and the underbody components, like driveshafts and exhaust pipes.

References

[1] http://www.formula1-dictionary.net/splitter.html

[2] http://www.vx220.org.uk/forums/topic/71504-which-splitter/

[3] https://nasaspeed.news/tech/aero/air-dams-splitters-spoilers-and-wings-downforce-increases-grip-grip-decreases-lap-times-and-isnt-that-the-whole-point/

[4] https://www.racetechmag.com/2017/08/willem-toet-explains-motorsport-diffusers/

[5] https://www.racecar-engineering.com/tech-explained/diffusers-engineering-basics-aerodynamics/

[6] http://www.formula1-dictionary.net/diffuser.html

[7] Lions, JL.: Optimal control of systems governed by partial differential equations. Springer-Verlag, New York, 1971

[8] https://openfoam.org

[9] https://www.openfoam.com

[10] https://www.cfdsupport.com/why-openfoam.html

[11] Heft, A., Indinger T., Adams N.: "Introduction of a New Realistic Generic Car Model for Aerodynamic Investigations", SAE 2012 World Congress, April 23-26, 2012, Detroit, Michigan, USA, Paper 2012-01-0168

[12] Frank T.,Gerlicher B.,Abanto J.: "DrivAer-Aerodynamic Investigations for a New Realistic Generic Car Model using ANSYS CFD", ASWC 2013 - Automotive Simulation World Congress, Frankfurt am Main, Germany

[13] https://www.fiawec.com/en/classes/32

[14] https://www.autosport.com/wec/news/141428/first-wave-of-2019-le-mans-entries-revealed

[15] https://www.autosport.com/wec/news/141843/top-us-gte-teams-among-final-le-mans-entrants

[16] https://www.lemans.org/en/news/24-hours-of-le-mans-af-corse-lmgte-pro/52033

[17] https://www.fiawec.com/en/race/result/4604

[18] https://media.chevrolet.com/media/us/en/chevrolet/photos.detail.html/content/Pages/galleries/us/en/racing/Chevrolet/2018-chevy-racing/18-chevyracing.html#

[19] https://races.ferrari.com/en/competizioni-gt/multimedia/

[20] FIA WEC, 2019 Technical Regulations For Grand Touring Cars "LMGTE" Homologated From 2016, https://www.fia.com/fia-wec-2019-technical-regulations-grand-touring-cars-lmgte-homologated-2016

[21] http://cdntbs.astonmartin.com/sitefinity/racing/racing-gte1-2018.jpg?sfvrsn=0

[22] https://www.porsche.com/international/motorsportandevents/motorsport/racingcars/991-911-rsr/

[23] https://www.ford.com/content/dam/brand_ford/en_us/brand/performance/gt/gallery/3_2/RP---Ford-GT-Le-Mans-36_PK.jpg/jcr:content/renditions/cq5dam.web.1440.1440.jpeg

[24] *https://www.carbodydesign.com/gallery/2018/06/interview-with-bmw-motorsport-designer-michael-scully-on-the-new-m8-gte/20/*

[25] *https://www.openfoam.com/documentation/guides/latest/doc/guide-meshing-snappyhexmesh-layers.html*

[26] *https://cfd.direct/openfoam/user-guide/v6-snappyhexmesh/*

[27] *Landau, L., Lifshitz, E.: "Fluid Mechanics, Volume 6 of Course of Theoretical Physics", Pergamon Press, 1987*

[28] *Davidson, P: "Turbulence: An Introduction for Scientists and Engineers", Oxford University Press, Oxford, 2015*

[29] *Schmitt, F.G: "About Boussinesq's turbulent viscosity hypothesis: historical remarks and a direct evaluation of its validity", Comptes Rendus Mecanique, (335):617–627, 2007*

[30] *Spalart, Ph., Allmaras, S.: "A one-equation turbulence model for air flows", AIAA Paper 1992-439, 30th Aerospace Sciences Meeting and Exhibit, Reno, Nevada, USA, January 6–9 1992*

[31] *https://turbmodels.larc.nasa.gov/spalart.html*

[32] *https://pdfs.semanticscholar.org/32c3/71dc61d8bc060835f4e3a306fd43e5df9b37.pdf*

[33] *Fangqing Liu.: "A Thorough Description Of How Wall Functions Are Implemented In OpenFOAM", In Proceedings of CFD with OpenSource Software, 2016, Edited by Nilsson. H., http://www.tfd.chalmers.se/~hani/kurser/OS_CFD_2016*

[34] *Anderson, J., "Fundamentals Of Aerodynamics", Third Edition, McGraw-Hill Series in Aeronautical and Aerospace Engineering, McGraw-Hill, New York, 2001*

[35] *Giannakoglou, K., Papoutsis Kiachagias, E., Kavvadias, I., Gkaragkounis, K., "adjointOptimization, an OpenFOAM-based optimization tool", User Manual, Prepared by the Parallel CFD & Optimization Unit, School of Mechanical Engineering, NTUA, Athens, 2018*

[36] *https://www.grc.nasa.gov/www/k-12/airplane/dragco.html*

[37] *https://www.openfoam.com/documentation/guides/latest/doc/guide-applications-solvers-simple.html*

[38] *https://www.openfoam.com/documentation/user-guide/fvSchemes.php*

[39] *Giannakoglou, K.C. "Μέθοδοι Βελτιστοποίησης Στην Αεροδυναμική" (Optimization Methods In Aerodynamics) 4th Edition, National University Of Athens Press, Athens, 2006*

[40] *Karpouzas, G.K., Papoutsis-Kiachagias, E.M., Schumacher, T., de Villiers, E., Giannakoglou, K.C.: Othmer, C.: "Adjoint Optimization for Vehicle External Aerodynamics", 2015*

[41] *Grinfield, P: "Hadamart's Formula Inside And Out", Journal of optimization theory and applications, 2010*

[42] *Zymaris, A.S, Papadimitriou, D.I., Giannakoglou, K.C., Othmer, C.: "Continuous adjoint approach to the Spalart-Allmaras turbulence model for incompressible flows", Computers & Fluids, 38(8)*

[43] *Giannakoglou, K.C., Papoutsis-Kiachagias, E.M., Kavvadias I.S., Gkaragkounis, K.T.: "Continuous Adjoint in Shape & Topology Optimization — Recent Developments & Applications"*

[44] *Papoutsis-Kiachagias, E.M., Giannakoglou, K.C.: "Continuous adjoint methods for turbulent flows, applied to shape and topology optimization: Industrial applications", Archives of Computational Methods in Engineering*

[45] *Papoutsis-Kiachagias, E, "Adjoint Methods for Turbulent Flows, Applied to Shape or Topology Optimization and Robust Design", PhD Thesis at Laboratory Of Thermal Turbomachines, National Technical University Of Athens, Athens, 2013*

[46] *I.S. Kavvadias, E.M. Papoutsis-Kiachagias, K.C. Giannakoglou, "On the proper treatment of grid sensitivities in continuous adjoint methods for shape optimization", J. Comput. Phys. (2015), http://dx.doi.org/10.1016/j.jcp.2015.08.012*

[47] Papoutsis-Kiachagias, E., Giannakoglou, K., "A parameterization and mesh movement strategy based on volumetric B-splines. Applications to shape optimization", Parallel CFD & Optimization Unit, School of Mechanical Engineering, NTUA, Athens, January 2015

Εθνικό Μετσόβιο Πολυτεχνείο
Σχολή Μηχανολόγων Μηχανικών
Τομέας Ρευστών
Μονάδα Παράλληλης ΥΡΔ & Βελτιστοποίησης

Αεροδυναμικός Σχεδιασμός Ανάλυση & Βελτιστοποίηση Μορφής Με Τη Συζυγή Μέθοδο Αγωνιστικού Πατώματος Αυτοκινήτου Σε Περιβάλλον OpenFOAM

Διπλωματική Εργασία

Νικολακόπουλος Αναστάσιος

Επιβλέπων: Καθηγητής Κυριάκος Χ. Γιαννάκογλου

Εκτενής Περίληψη Στα Ελληνικά

1. Εισαγωγή

Στον μηχανοκίνητο αθλητισμό, είναι επιθυμητή η αύξηση της πρόσφυσης των ελαστικών με το οδόστρωμα. Μία μέθοδος αύξησης είναι η αύξηση της κάθετης αεροδυναμικής δύναμης (στο εξής εννοείται με φορά προς το οδόστρωμα). Οι μηχανικοί σχεδιάζουν το αμάξωμα του οχήματος έτσι ώστε να επιτυγχάνεται μεγάλη κάθετη αεροδυναμική δύναμη και κατά τον δυνατόν μικρή αεροδυναμική αντίσταση. Δύο εξαρτήματα που χρησιμοποιούνται συχνά είναι ο εμπρός splitter και ο πίσω διαχύτης.

Σκοπός της εργασίας είναι η μετατροπή του πατώματος του μοντέλου οχήματος DrivAer με προσθήκη εμπρός splitter και πίσω διαχύτη, και η βελτιστοποίησή τους με χρήση της συνεχούς συζυγούς μεθόδου και ογκομετρικών b-splines. Η μετατροπές έγιναν σύμφωνα με τους κανονισμούς Le Mans Grand Touring Endurance. Η γένεση του πλέγματος, η επίλυση του πρωτεύοντος και συζυγούς προβλήματος και η βελτιστοποίηση έγιναν όλα σε περιβάλλον OpenFOAM. Το μοντέλο προς βελτιστοποίηση απεικονίζεται στο σχήμα 1.1.
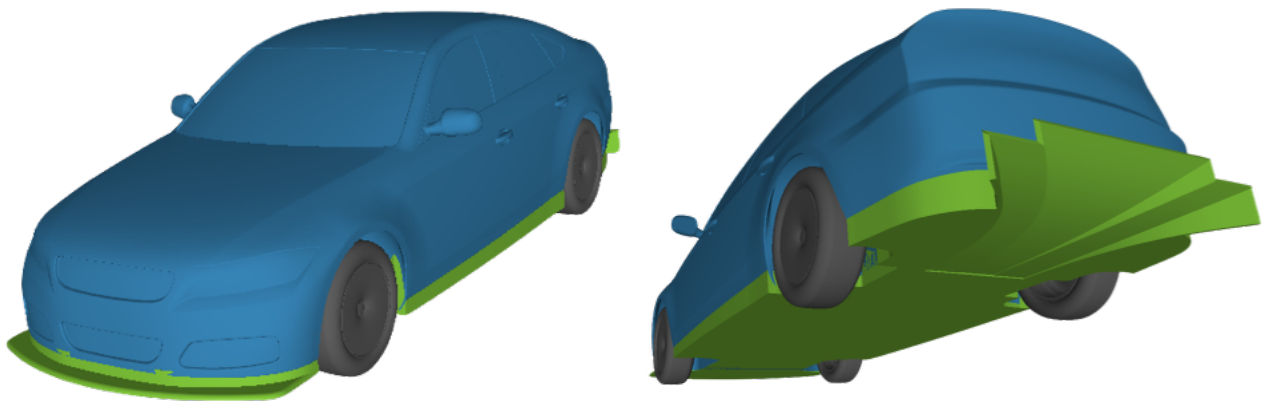
Σχήμα 1.1: Το μοντέλο προς βελτιστοποίηση σε εμπρός 3/4 όψη (αριστερά) και σε πίσω 3/4 όψη (δεξιά).

2.   Γένεση Πλέγματος

Η γένεση πλέγματος έγινε με χρήση των εργαλείων *blockMesh*, για την δημιουργία του υπολογιστικού χωρίου με δομημένο πλέγμα, του εργαλείου *surfaceFeatureExtract*, για την αναγνώριση χαρακτηριστικών καμπυλών στην γεωμετρία και του εργαλείου *snappyHexMesh*, για την δημιουργία του τελικού υβριδικού πλέγματος και λεπτομερειών. Το πλέγμα δημιουργήθηκε γύρω από το δεξί ήμισυ του οχήματος, λόγω συμμετρίας της γεωμετρίας. Επίσης, δημιουργήθηκαν δύο περιοχές αυξημένης ανάλυσης πλέγματος, μία μόνο για τη γεωμετρία του οχήματος και μία για τη γεωμετρία του οχήματος μαζί με τον ομόρρου και περιοχή αυξημένης ανάλυσης πλησίον του δρόμου. Το τελικό πλέγμα έχει διαστάσεις 11 × 18 × 7 m και αποτελείται από 4.846.058 κελιά. Στο σχήμα 2.1 φαίνονται περιοχές του πλέγματος.
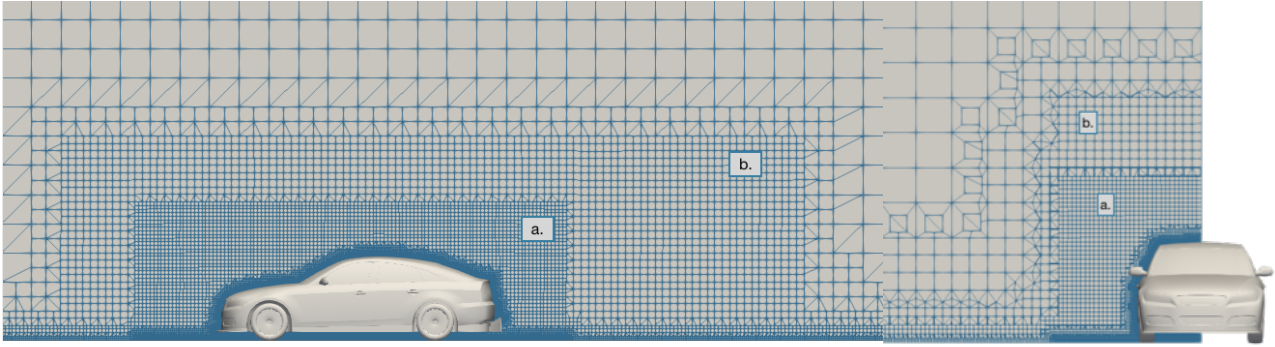
Σχήμα 2.1: Τμήμα του υπολογιστικού πλέγματος. Διακρίνονται οι περιοχές αυξημένης ανάλυσης για το όχημα (a) και για τον ομόρρου (b) σε πλάγια όψη (αριστερά) και σε εμπρός τομή (δεξιά).

3.   Το Πρωτεύον Πρόβλημα

Το πρωτεύον πρόβλημα περιγράφεται από τις Raynold Averaged εξισώσεις Navier—Stokes και το μοντέλο τύρβης, που έχει επιλεχθεί το Spalart—Allmaras. Οι εξισώσεις που περιγράφουν την ασυμπίεστη και χρονικά σταθερή ροή είναι οι εξής:

1.
$$R^p = -\frac{\partial u_j}{\partial x_j} = 0$$

2.
$$R^u_{\ j} = \frac{\partial u_i}{\partial t} + u_j \frac{\partial u_i}{\partial x_j} + \frac{\partial p}{\partial x_i} - \frac{\partial}{\partial x_j}\left[(\nu + \nu_t)\left(\frac{\partial u_i}{\partial x_j} + \frac{\partial u_j}{\partial x_i}\right)\right] = 0$$

Ενώ η βασική εξίσωση του μοντέλου τύρβης είναι η:

3.
$$R^{\tilde{\nu}} = \frac{\partial \tilde{\nu}}{\partial t} + u_j \frac{\partial \tilde{\nu}}{\partial x_j} - C_{b_1}\left(1 - f_{t_2}\right)\tilde{S}\tilde{\nu} + \left(C_{w_1}f_w - \frac{C_{b_1}}{\kappa^2}f_{t_2}\right)\left(\frac{\tilde{\nu}}{d}\right)^2 - \frac{1}{\sigma}\left[\frac{\partial}{\partial x_j}\left[(\nu + \tilde{\nu})\frac{\partial \tilde{\nu}}{\partial x_j}\right] - C_{b_2}\frac{\partial \tilde{\nu}}{\partial x_i}\frac{\partial \tilde{\nu}}{\partial x_i}\right] = 0$$

Στις οριακές συνθήκες, ορίστηκε, μεταξύ άλλων η ταχύτητα εισόδου. Επομένως, θεωρώντας ως μήκος αναφοράς το μεταξόνιο του οχήματος, το οποίο είναι 2,786 m, προκύπτει ο αριθμός Reynolds της ροής ίσος με $6{,}7{\times}10^6$.

Το πρωτεύον πρόβλημα επιλύθηκε και για το πρωτότυπο όχημα, αλλά και για το όχημα με τις αεροδυναμικές μετατροπές. Ο αλγόριθμος επίλυσης ήταν ο SIMPLE Τα αποτελέσματα των αεροδυναμικών δυνάμεων καταγράφονται στον πίνακα 3.1.

Μοντέλο	Συντελεστής	
	Αντίστασης	Άνωσης
Πρωτότυπο DrivAer	0.365	0.116
LM GTE Μετατροπές	0.326	-0.046
Διαφορά (%)	-10.68%	-139.66%

Γίνεται φανερό πως οι μετατροπές βελτιώνουν σημαντικά την πρόσφυση, καθώς το όχημα παράγει πλέον αρνητική άνωση. Επίσης, μειώνεται κατά 10% η οπισθέλκουσα.
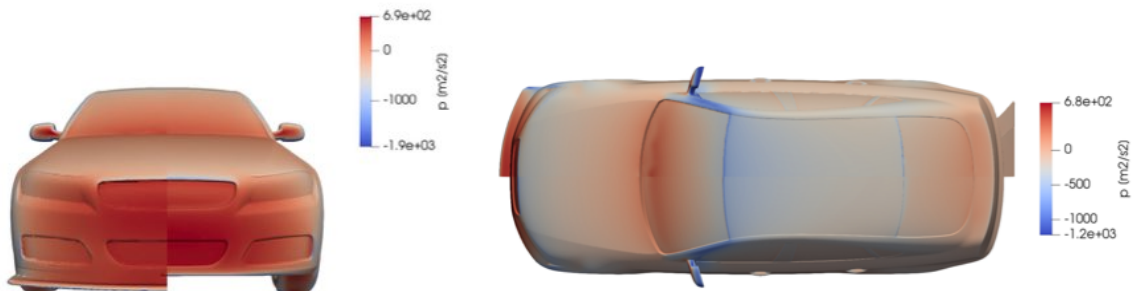
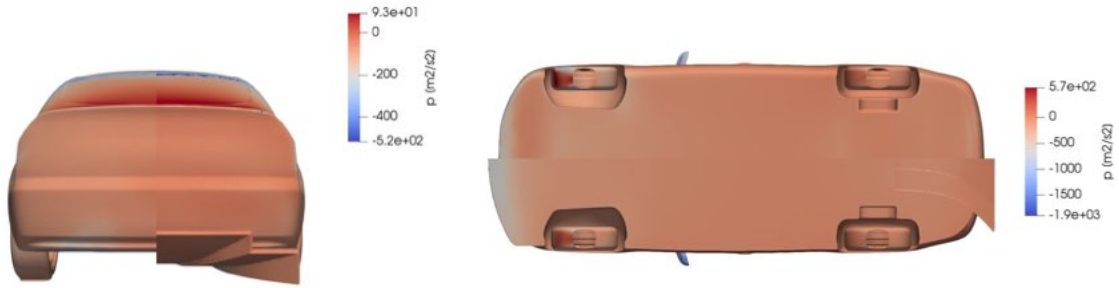Ορισμένες εικόνες από τα πεδία ροής φαίνονται στα σχήματα 3.1 έως 3.4.

Σχήμα 3.1: Το πεδίο του μέτρου της ταχύτητας στο επίπεδο συμμετρίας για το πρωτότυπο όχημα (αριστερά) και για το όχημα με τις μετατροπές (δεξιά).
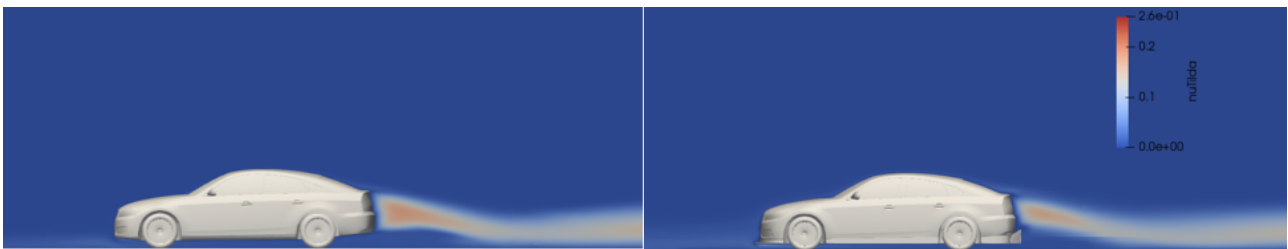

Σχήμα 3.2: Το πεδίο της πίεσης στο επίπεδο συμμετρίας για το πρωτότυπο όχημα (αριστερά) και για το όχημα με τις μετατροπές (δεξιά).

Σχήμα 3.3: Το πεδίο της πίεσης επάνω στο όχημα, σε εμπρός όψη (επάνω αριστερά), πίσω όψη (κάτω αριστερά), άνω όψη (επάνω δεξιά) κάτοψη (κάτω δεξιά). Το πρωτότυπο όχημα βρίσκεται στα δεξιά του οχήματος.

Σχήμα 3.4: Τα πεδία της μεταβλητής ṽ στο επίπεδο συμμετρίας για το πρωτότυπο όχημα (αριστερά) και για το όχημα με τις μετατροπές (δεξιά).

Παρατηρείται πως ο εμπρός splitter εγκλωβίζει την σχεδόν ακίνητη ροή στο άνω του μέρος ενώ επιτρέπει την κίνηση της ταχέως κινούμενης ροής στο κάτω του μέρος. Η διαφορά πίεσης που προκύπτει καταλήγει στην δημιουργία κάθετης δύναμης στο εμπρός μέρος. Επίσης, η κατανομή της πίεσης στο πάτωμα είναι περισσότερο ομοιόμορφη στο όχημα με τις μετατροπές. Υπάρχουν ακόμη μικρές διαφορές στον ομόρρου των δύο οχημάτων.

4. Το Συζυγές Πρόβλημα

Το συζυγές πρόβλημα περιγράφεται από τις συζυγείς εξισώσεις ροής, τις συζυγείς εξισώσεις του μοντέλου τύρβης, και την συζυγή εξίσωση για τις μετατοπίσεις του πλέγματος:

4.
$$R^q = -\frac{\partial v_j}{\partial x_j} = 0$$

5.
$$R^v_i = v_j \frac{\partial u_j}{\partial x_i} - \frac{\partial (u_j v_i)}{\partial x_j} + \frac{\partial q}{\partial x_i} - \frac{\partial}{\partial x_j}\left((\nu + \nu_t)\left(\frac{\partial v_i}{\partial x_j} + \frac{\partial v_j}{\partial x_i} \right) \right) = 0$$

6. $R^{\tilde{v}_a} = -\frac{\partial (u_j \tilde{v}_a)}{\partial x_j} - \frac{\partial}{\partial x_j}\left[\left(\nu + \frac{\tilde{\nu}}{\sigma} \right) \frac{\partial \tilde{v}_a}{\partial x_j} \right] + \frac{1}{\sigma} \frac{\partial \tilde{v}_a}{\partial x_j} \frac{\partial \tilde{v}}{\partial x_j} + \frac{2C_{b_2}}{\sigma} \frac{\partial}{\partial x_j}\left(\tilde{v}_a \frac{\partial \tilde{v}}{\partial x_j} \right) + \tilde{v}_a \tilde{v} C_{\tilde{v}} + \frac{\partial \nu_t}{\partial \tilde{\nu}} \frac{\partial v_i}{\partial x_j}\left(\frac{\partial u_i}{\partial x_j} + \frac{\partial u_j}{\partial x_i} \right) + (-P + D)\tilde{v}_a = 0$

7.
$$R^m_i = \frac{\partial^2 m_i}{\partial x_j^2} = 0$$

Οι παράγωγοι ευαισθησίας υπολογίζονται με την μέθοδο E-SI ως εξής:

8.
$$\frac{\delta F_{aug}}{\delta b_n} = \oiint_{S_{M_b}} \left[(\nu + \nu_t)\left(\frac{\partial v_i}{\partial x_j} + \frac{\partial v_j}{\partial x_i}\right) n_j - q n_i + \frac{\partial F_{S_{M_{b,l}}}}{\partial u_i} n_l \right] \frac{\partial u_i}{\partial b_n} \frac{\delta x_m}{\delta b_n} dS$$

$$+ \oiint_{S_{M_b}} \frac{\partial F_{S_{M_{b,i}}}}{\partial x_m} \frac{\partial u_i}{\partial b_n} n_i \frac{\delta x_k}{\delta b_n} dS + \oiint_{S_{M_b}} F_{S_{M_{b,i}}} n_i \frac{\delta(dS)}{\delta b_n}$$

$$+ \oiint_{S_{M_b}} \frac{\partial m_i^a}{\partial x_j} n_i \frac{\delta x_i}{\delta b_n} dS$$

$$- \oiint_{S_{M_b}} \left[\left(-v_k n_k + \frac{\partial F_{S_{M_{b,k}}}}{\partial \tau_{lz}} n_k n_l n_z \right) \left(\tau_{ij} \frac{\delta(n_i n_j)}{\delta b_n} + \frac{\partial \tau_{ij}}{\partial x_m} \frac{\delta x_k}{\delta b_n} n_i n_j \right) \right] dS$$

$$- \oiint_{S_{M_b}} \left[\frac{\partial F_{S_{M_{b,k}}}}{\partial \tau_{lz}} n_k t_l^I t_z^I \left(\tau_{ij} \frac{\delta(t_i^I t_j^I)}{\delta b_n} + \frac{\partial \tau_{ij}}{\partial x_k} n_k \frac{\delta x_k}{\delta b_n} t_i^I t_j^I \right) \right] dS$$

$$- \oiint_{S_{M_b}} \left[\left(\frac{\partial F_{S_{M_{b,k}}}}{\partial \tau_{lz}} n_k \left(t_l^{II} t_z^I + t_l^I t_z^{II} \right) \right) \left(\tau_{ij} \frac{\delta(t_i^{II} t_j^I)}{\delta b_n} + \frac{\partial \tau_{ij}}{\partial x_k} n_k \frac{\delta x_k}{\delta b_n} t_i^{II} t_j^I \right) \right] dS$$

$$- \oiint_{S_{M_b}} \left[\left(\frac{\partial F_{S_{M_{b,k}}}}{\partial \tau_{lz}} n_k t_l^{II} t_z^{II} \right) \left(\tau_{ij} \frac{\delta(t_i^{II} t_j^{II})}{\delta b_n} + \frac{\partial \tau_{ij}}{\partial x_k} n_k \frac{\delta x_k}{\delta b_n} t_i^{II} t_j^{II} \right) \right] dS$$

Το συζυγές πρόβλημα επιλύθηκε με λογισμικό που έχει αναπτυχθεί στην ΜΠΥΡ&Β του ΕΜΠ στο λογισμικό OpenFOAM. Προκύπτουν τα συζυγή πεδία ροής για το όχημα με τις μετατροπές, τα οποία φαίνονται στα σχήματα 4.1 έως 4.5.
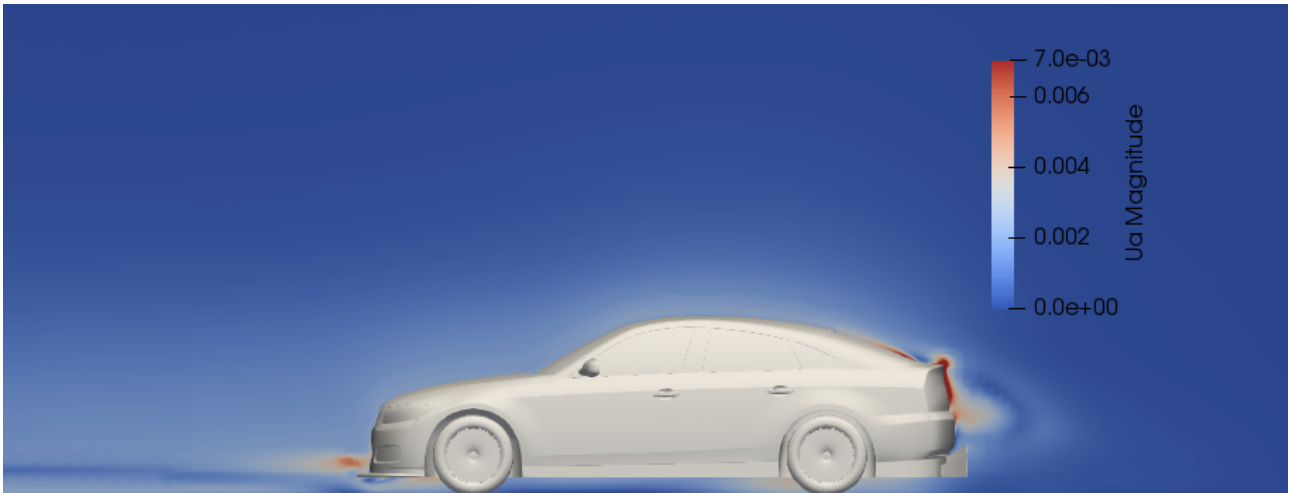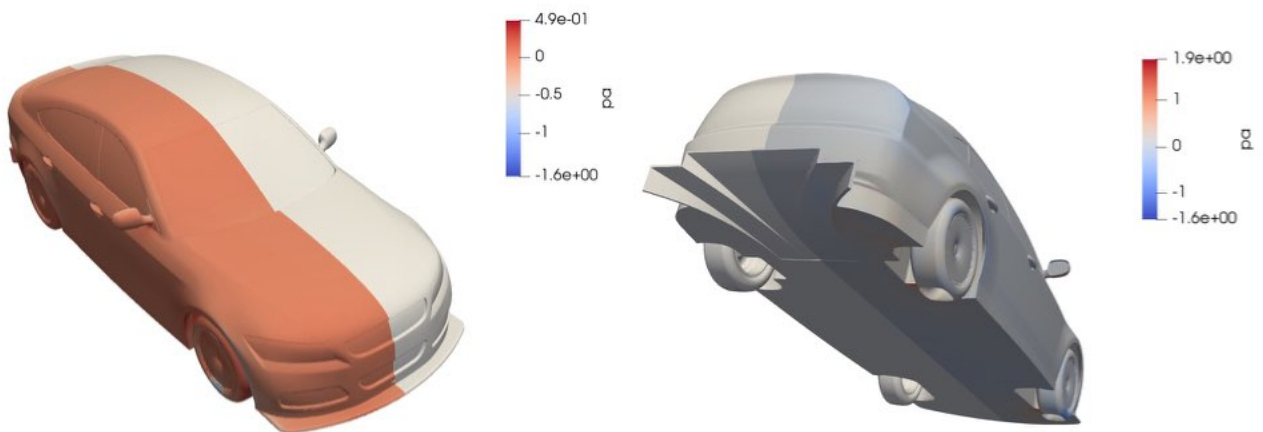

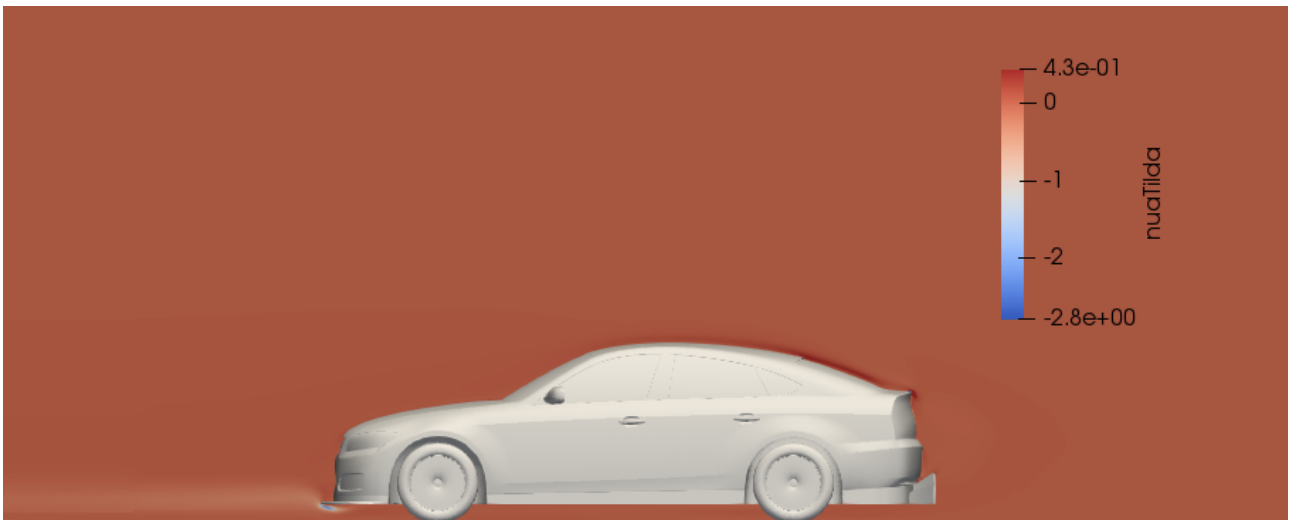*Σχήμα 4.1: Το μέτρο της συζυγούς ταχύτητας στο επίπεδο συμμετρίας.*
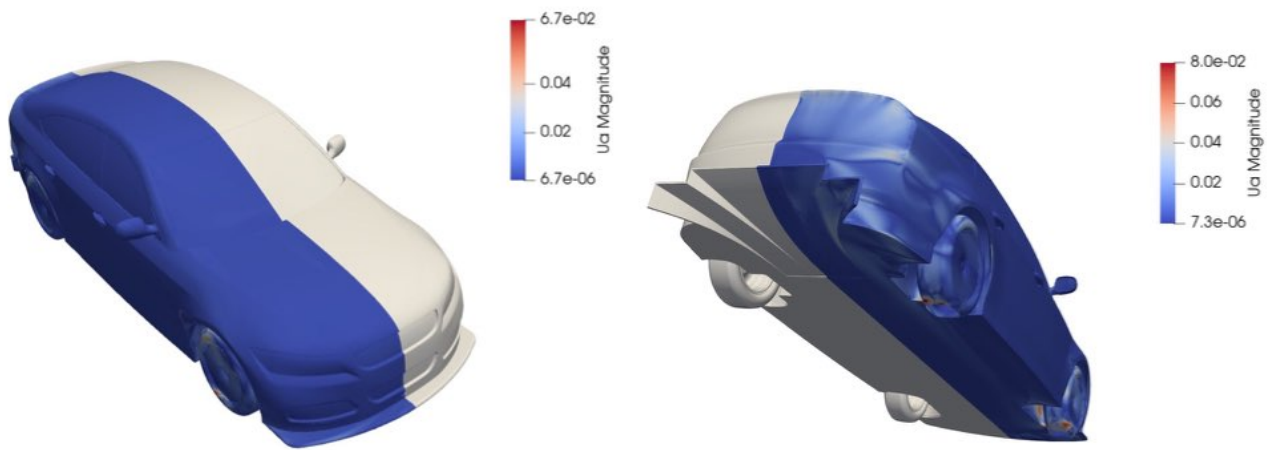
Σχήμα 4.2: Το μέτρο της συζυγούς ταχύτητας επάνω στο όχημα, σε εμπρός 3/4 όψη (αριστερά) και πίσω 3.4 όψη (δεξιά).
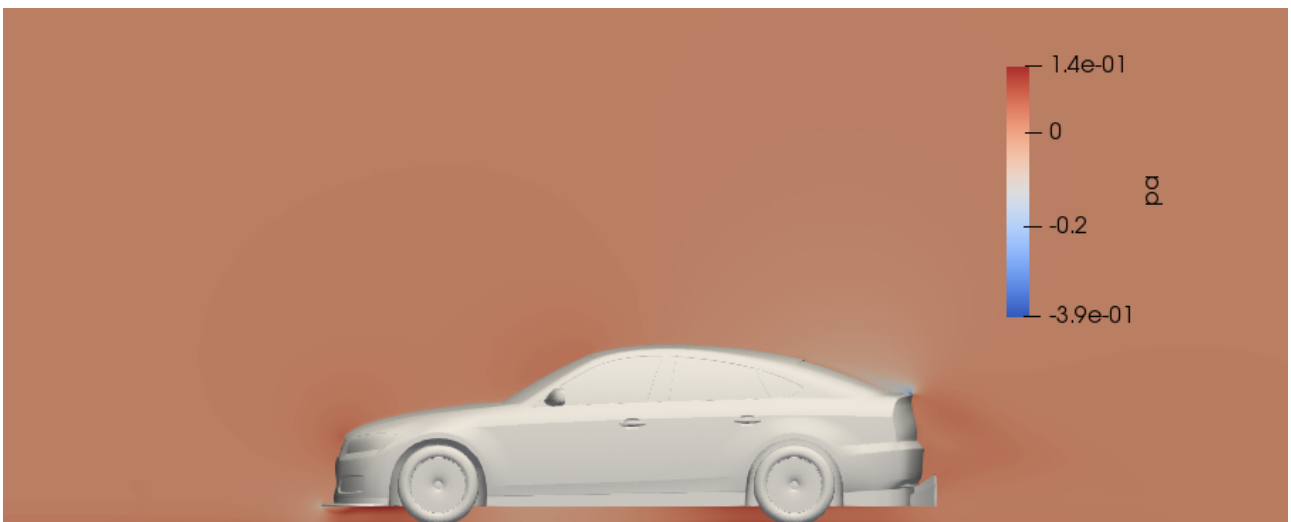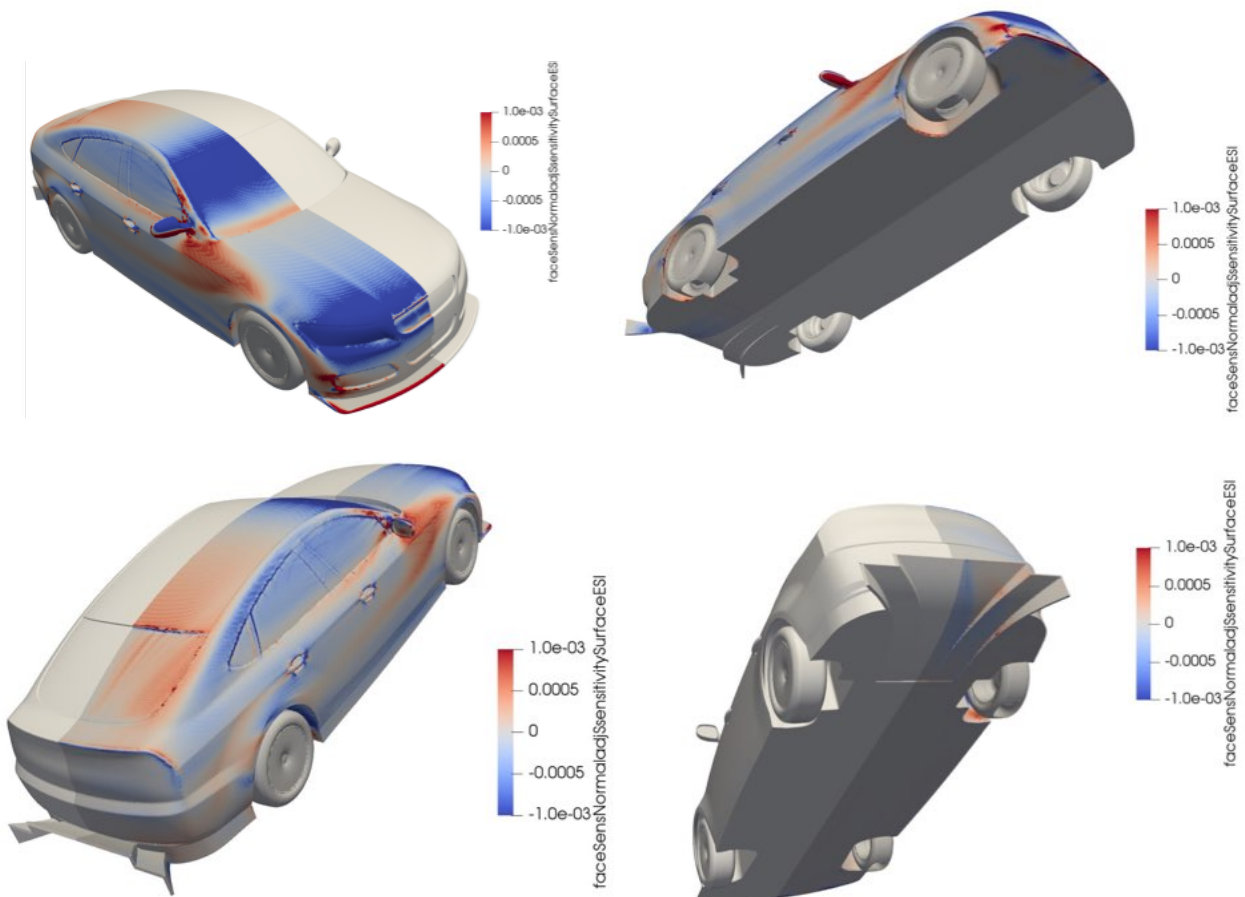

Σχήμα 4.3: Το πεδίο της συζυγούς πίεσης στο επίπεδο συμμετρίας.

Σχήμα 4.4: Το μέτρο της συζυγούς ταχύτητας επάνω στο όχημα, σε εμπρός 3/4 όψη (αριστερά) και πίσω 3.4 όψη (δεξιά).

Σχήμα 4.5: Το πεδίο της συζυγούς μεταβλητής ṽ στο επίπεδο συμμετρίας.

Ο χάρτη ευαισθησίας φαίνεται στο σχήμα 4.6.

Σχήμα 4.6: Ο χάρτης ευαισθησίας, σε εμπρός 3/4 άνω όψη (επάνω αριστερά) και κάτω όψη (επάνω δεξιά) και πίσω 3/4 άνω όψη (κάτω αριστερά) και κάτω όψη (κάτω δεξιά). Το μπλε χρώμα σημαίνει αύξηση του στόχου με μετατόπιση προς τα μέσα, ενώ το κόκκινο με μετατόπιση προς τα έξω.

Από τον χάρτη ευαισθησίας, προκύπτει το συμπέρασμα πως η περαιτέρω αύξηση της κάθετης μείωσης θα επιτευχθεί μέσω:

- Της επιμήκυνσης του εμπρός splitter,

- Την ανύψωσης του χείλους προσβολής του εμπρός splitter,

- Την μετατόπιση προς τα μέσα της περιοχής στο ύψος των εμπρός φωτιστικών και της κορυφής του παρμπρίζ προς τα μέσα, καθώς αυτές είναι περιοχές που επιταχύνεται ο αέρας και μειώνεται η στατική πίεση, με αποτέλεσμα να δημιουργείται άνωση,

- Της μετατροπής του πίσω διαχύτη,

- Την αύξηση του μεγέθους των spoilers στο επάνω μέρος του επάνω παραθύρου και της κορυφής της θύρας των αποσκευών,

- Την τροποποίηση των πλάγιων καθρεπτών, έτσι ώστε να έχουν σχήμα πτέρυγας,

- Την μετατόπισης μέρους των εμπρός φτερών και θυρών προς τα έξω,

- Την μετατόπιση της κολόνας Α προς τα μέσα,

- Των μικρών αλλαγών εντός των θόλων των τροχών.

## 5. Βελτιστοποίηση Μορφής Με b-Splines

Για την βελτιστοποίηση μορφής με b-splines, επιλέχθηκε να βελτιστοποιηθεί το σχήμα του εμπρός splitter και του πίσω διαχύτη. Κατά συνέπεια, ορίστηκαν τα σημεία ελέγχου στις περιοχές αυτές, όπως φαίνεται στο σχήμα 5.1.


Σχήμα 5.1: Τα σημεία ελέγχου στον εμπρός splitter (αριστερά) και στον πίσω διαχύτη (δεξιά).

Τα σημεία ελέγχου ορίσθηκαν με τρόπου τέτοιο, ώστε και η βελτιστοποιημένη γεωμετρία να υπακούει στους κανονισμούς.

Εν συνεχεία, εκτελέσθηκε ο αλγόριθμος βελτιστοποίησης, με λογισμικό που έχει επίσης αναπτυχθεί στην ΜΠΥΡ&Β του ΕΜΠ στο λογισμικό OpenFOAM. Τα αποτελέσματα της βελτιστοποίησης φαίνονται στα σχήματα 5.2 και 5.3.
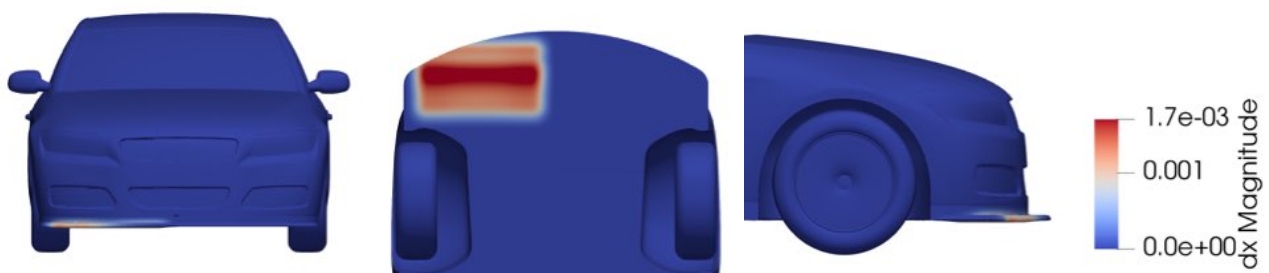
Σχήμα 5.2: Η βελτιστοποιημένη μορφή του εμπρός splitter σε εμπρός όψη (αριστερά), κάτοψη (μέση) και πλάγια όψη (δεξιά).
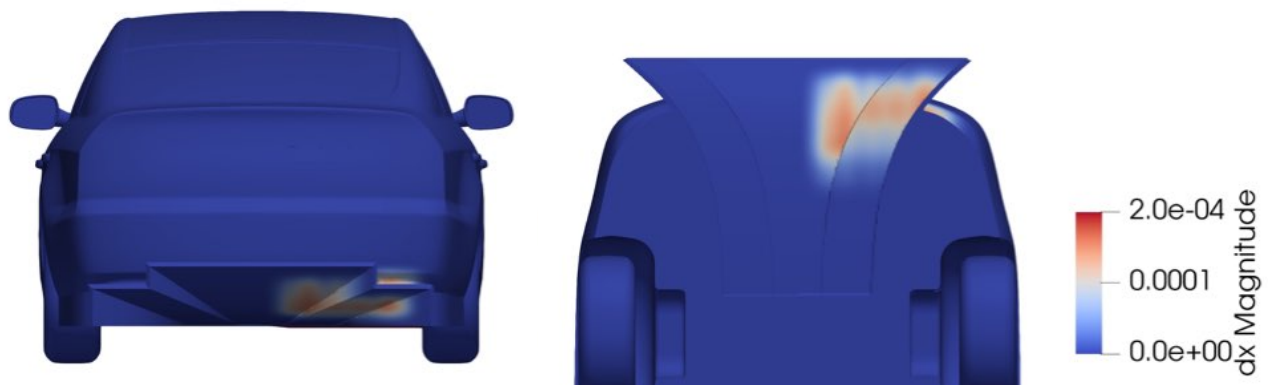
Σχήμα 5.3: Η βελτιστοποιημένη μορφή του πίσω διαχύτη σε πίσω όψη (αριστερά) και κάτοψη (δεξιά).

Στον πίνακα 5.1 καταγράφονται οι αεροδυναμικές δυνάμεις, όπως προέκυψαν από την βελτιστοποίηση.

Πίνακας 5.1: Οι αεροδυναμικοί συντελεστές του πρωτότυπου μοντέλου, του μοντέλου με τις μετατροπές και του βελτιστοποιημένου μοντέλου.

Μοντέλο	Συντελεστής	
	Αντίστασης	Άνωσης
Πρωτότυπο DrivAer	0.365	0.116
Μετατροπές LM GTE	0.326	-0.046
Βελτιστοποιημένο	0.327	-0.085
Διαφορά Από Το Πρωτότυπο (%)	-10.41%	-173.43%
Διαφορά Από Το Αρχικό (%)	0.31%	-85.16%

6. Συμπεράσματα

Οι προσθήκες βελτιώνουν πολύ την αεροδυναμική απόδοση. Επιτυγχάνεται μείωση 140% στην άνωση, δηλαδή το όχημα παράγει αρνητική άνωση. Παράλληλα, μειώνεται ο συντελεστής αντίστασης κατά 10%. Με την βελτιστοποίηση, αυξάνεται περαιτέρω η κάθετη δύναμη κατά 85%, ενώ υπάρχει μικρή αύξηση της αντίστασης κατά 0.3%.

7. Προτεινόμενη Βιβλιογραφία

1. *https://www.fiawec.com/en/classes/32*

2. *FIA WEC, 2019 Technical Regulations For Grand Touring Cars "LMGTE" Homologated From 2016, https://www.fia.com/fia-wec-2019-technical-regulations-grand-touring-cars-lmgte-homologated-2016*

3. *Spalart, Ph., Allmaras, S.: "A one-equation turbulence model for air flows", AIAA Paper 1992-439, 30th Aerospace Sciences Meeting and Exhibit, Reno, Nevada, USA, January 6–9 1992*

4. *Giannakoglou, K., Papoutsis Kichagias, E., Kavvadias, I., Gkaragkounis, K., "adjointOptimization, an OpenFOAM-based optimization tool", User Manual, Prepared by the Parallel CFD & Optimization Unit, School of Mechanical Engineering, NTUA, Athens, 2018*

5. *https://www.openfoam.com/documentation/guides/latest/doc/guide-applications-solvers-simple.html*

6. *Giannakoglou, K.C. "Μέθοδοι Βελτιστοποίησης Στην Αεροδυναμική" (Optimization Methods In Aerodynamics) 4th Edition, National University Of Athens Press, Athens, 2006*

7. *Papoutsis-Kichagias, E, "Adjoint Methods for Turbulent Flows, Applied to Shape or Topology Optimization and Robust Design", PhD Thesis at Laboratory Of Thermal Turbomachines, National Technical University Of Athens, Athens, 2013*

8. *I.S. Kavvadias, E.M. Papoutsis-Kiachagias, K.C. Giannakoglou, "On the proper treatment of grid sensitivities in continuous adjoint methods for shape optimization", J. Comput. Phys. (2015), http://dx.doi.org/10.1016/j.jcp.2015.08.012*

9. *Papoutsis-Kichagias, E., Giannakoglou, K., "A parameterization and mesh movement strategy based on volumetric B-splines. Applications to shape optimization", Parallel CFD & Optimization Unit, School of Mechanical Engineering, NTUA, Athens, January 2015*